Summer 6-18-2013

A Structural and Mechanistic Study of Two Members of Cupin Family Protein

Fange Liu
Georgia State university

A STRUCTURAL AND MECHANISTIC STUDY OF TWO MEMBERS OF CUPIN FAMILY PROTEIN

by

FANGE (KATHERINE) LIU

Under the Direction of Dr. Aimin Liu

ABSTRACT

Cupin superfamily is a functionally diverse large group of proteins sharing a jelly roll β-barrel fold. An enzymatic member 3-hydroxyanthranilate-3,4-dioxygenase (HAO) and a non-enzymatic member pirin, which is a human nuclear metalloprotein of unknown function present in all human tissues, were selected for structural and functional studies in this dissertation work. HAO is an important enzyme for tryptophan catabolism and for 2-nitrobenzoic acid biodegradation. In this work, seven catalytic intermediate were captured in HAO single crystals, enabling for the first time a nearly complete structural snapshot viewing of the entire molecular oxygen activation and insertion mechanism in an iron- and O_2-depedent enzyme. The rapid catalytic turnover rate was found achieved in large part by protein dynamics that facilitates O_2 binding to the catalytic iron, which is bound to the enzyme by a facile 2-His-1-carboxylate ligand motif. An iron storage and chaperon mechanism was also discovered in the bacterial source of this enzyme, which led to a proposed novel biological function of a mononuclear

iron-sulfur center. Although human pirin protein shares the same structural fold with HAO, its iron ion is coordinated by a 3-His-1-carboxylate ligand motif. Pirin belongs to a subset of proteins whose members are playing regulatory functions in the superfamily. In this work, pirin is shown to act as a redox sensor for the NF-κB transcription factor, a critical mediator of intracellular signaling that has been linked to cellular responses to pro-inflammatory signals which controls the expression of a vast array of genes involved in immune and stress responses.

INDEX WORDS: Metalloprotein, Oxygen activation, Catalytic mechanism, Protein-protein and Protein-DNA interactions, Signaling transduction activation, Regulation of gene transcription

A STRUCTURAL AND MECHANISTIC STUDY OF TWO MEMBERS OF CUPIN FAMILY PROTEIN

by

FANGE (KATHERINE) LIU

A Dissertation Submitted in Partial Fulfillment of the Requirements for the Degree of

Doctor of Philosophy

in the College of Arts and Sciences

Georgia State University

2013

A STRUCTURAL AND MECHANISTIC STUDY OF TWO MEMBERS OF CUPIN FAMILY PROTEIN

by

FANGE (KATHERINE) LIU

Committee Chair: Dr. Aimin Liu

Committee: Dr. David Wilson

Dr. Donald Hamelberg

Electronic Version Approved:

Office of Graduate Studies

College of Arts and Sciences

Georgia State University

August 2013

DEDICATION

I would like to thank my wonderful family!

ACKNOWLEDGEMENTS

It is very lucky of me to have Dr. Aimin Liu as my Ph.D. advisor. He is a great scientist with infinity of sparkling research ideas. He is also a fantastic teacher and speaker; he can always explain the complicated scientific meaning in an easy way to be understood. Dr. Liu is very supportive to his students and I benefit a lot from it. I wish that I could be as lively, enthusiastic and energetic as Dr. Liu and to someday be able to command an audiences as well as he can.

I would like to thank my committee members, Dr. David Wilson and Dr. Donald Hamberlg. Dr. Wilson taught me how to use surface Plasmon resonance and analyze the data. He is my primary source for getting my SPR questions answered. Dr. Hamberlg provides very insightful suggestions in my defense about protein dynamics, which make up my knowledge hole and helping me understand biochemistry more comprehensively.

I would like to sincerely thank the people, especially Dr. Judith Klinman and Dr. Amy Rosenzweig who has encouraged and told me that I could be a great scientist in the future. Their encouragement is always hovering on my mind, reminding me to be passionate on my dreams.

A good support system is indispensable for graduate students. I was lucky to have several excellent friends. My special “thank you” goes to Jingchun Li, Nangting Ni, Kednerlin Dornevil and Imran Rehmani

TABLE OF CONTENTS

ACKNOWLEDGEMENTS v

1. CUPIN SUPERFAMILY.....1

2. UNDERSTANDING EXTRADIOL DIOXYGENASE MECHANISM in NAD^+ BIOSYNTHESIS by VIEWING CATALYTIC INTERMEDIATES.....3

2.1. Abstract 3

2.2 Introduction 4

2.3 Results and Discussion 7

2.3.1 How does the organic substrate 3-HAA bind to HAO? 7

2.3.2 Single crystals of HAO are catalytic active 11

2.3.3 Catalytically active ternary complex from O_2 binding.....12

2.3.4 The oxygenated intermediates 14

2.3.5 The intermediate product bound HAO complexes 18

2.5 Further experimental details.....24

3. SUBSTRATE-INDUCED LOOP MOVEMENT IS ESSENCIAL FOR RAPID OXYGEN INCORPORATION IN 3-HYDROXYGANTHRANILIAT 3,4-DIOXYGENASE 29

3.1 Abstract.....29

3.2 Introduction 29

3.3 Result and Discussion.....31

3.3.1 Induced open-to-close scenario is observed in HAO upon substrate-binding 31

3.3.2 The chemical nature of the Fe center in the closed state 35

3.3.3 Structural requirement to induce loop movement.....35

3.3.4 Single mutation at Ile142 breaks down the loop movement phenomenon.....36

3.3.5 Structure of the I142A-3-HAA complex 38

3.4 Concluding Remarks 40

4. THE RUBREDOXIN FE IS A SPARE TIRE TO THE CATALYTIC NON-HEME FE IN BACTERIAL 3-HYDROXYANTHRANILATE-3,4-DIXOYGENASE 41

4.1 Abstract 41

4.2 Introduction 41

4.3 Materials and Methods 44

4.3.1 Chemicals 44

4.3.2 Protein preparation for the HAO catalytic activity assays 44

4.3.3 Catalytic activity measurement of adding apo-HAO to holo-HAO 44

4.3.4 Reconstitution of apo-HAO for Mössbauer measurements 44

4.3.5 Mössbauer spectroscopy 45

4.3.6 Electronic paramagnetic resonance (EPR) spectroscopy 45

4.3.7 X-ray data collection and crystallographic refinement 45

4.3.8 Fluorescence spectroscopy 46

4.4 Result 46

4.4.1 Metal-ion reconstitution of HAO and activity assay 46

4.4.2 Spectroscopic characterization of the reconstituted HAO 47

4.4.3 Mössbauer spectroscopy 48

Mössbauer spectroscopy ***48***

4.4.4 Metal binding affinity measured by tryptophan intrinsic fluorescence study 50

4.4.5 Crystal structures of Cu/Fe-HAO and Fe/Cu-HAO 50

4.4.6 The $Fe(Cys)_4$ is capable of delivering its Fe ion to apo-HAO 53

4.4 Discussion 55

5. PIRIN IS An IRON-DEPENDENT REDOX REGULATOR OF NF-κB 57

5.1 Abstract.....57

5.2 Introduction 57

5.3 Materials and Methods.....59

5.3.1 Protein materials.....59

5.3.2 Metal analysis.....60

5.3.3 Nuclear extract containing native NF-κB proteins 60

5.3.4 DNA 60

5.3.5 Spectroscopy.....61

5.3.6 Crystallizations and X-ray structure determinations.....62

5.3.7 In silico docking of the supercomplex 63

5.3.8 Experimental validation of the docking study.....63

5.3.9 Accession codes.....64

5.4 Results 64

5.4.1 Human pirin facilitates the DNA binding of p65 to the κB gene in a redox-state dependent manner 64

5.4.2 The protein-DNA supercomplex in the presence of pirin is compact and rigid.....68

5.4.3 Pirin-NF-κB-DNA supercomplex dissociates by added reducing agent.....68

5.4.4 The redox state of the Fe in pirin affects the conformation of a specific R-shaped surface area as revealed by X-ray protein crystallography 70

5.4.5 The crystal structures of the intermediate states of Fe-Pirin show the reversibility of the R-shaped loop conformation changes dependent on the oxidation state of the metal 73

5.4.6 The metal identity affects the conformation of the R-shaped surface area 76

5.4.7 The R-shaped region on pirin interacts with the C-terminal domain of NF-κB proteins.....*78*

5.5 Discussion.....**82**

5.6 Further Experimental Details.....**84**

5.6.1 Material preparations.....*84*

5.6.2 Method description.....*87*

REFERENCES.....**99**

LIST OF TABLES

Table 1. Catalytic activity of metal-reconstituted HAO……47

Table 2. X-ray crystallography data collection and refinement statistics of ligand-free, ligand bound- and Fe-bound intermediates of HAO……..93

Table 3. X-ray crystallography data collection and refinement statistics of HAO……94

Table 4. X-ray crystallographic data collection and refinement statistics of human pirin at the active ferric oxidation state……95

Table 5. X-ray crystallographic data collection and refinement statistics of metal-substituted pirin variants……96

Table 6. X-ray crystallographic data collection and refinement statistics of ferric E32V pirin variant… 97

LIST OF FIGURES

Figure 1.1. Four representative cupin proteins……1

Figure 1.2 Conserved consensus in cupin superfamily proteins…….. 2

Figure 2.1 HAO occupies a central position in two biological catabolic pathways……..3

Figure 2.2 Crystal structure of HAO and the proposed catalytic cycle (A to J) based on the X-ray time-resolved crystallographic study……6

Figure 2.3 A side-by-side comparison of the HAO active site and the 2,3-HPCD catalytic center……6

Figure 2.4. Active site structures of substrate-free (A, PDB entry: 4L2N) and substrate-bound HAO in monodentate coordination (B, PDB entry: 4L2P) and in bidentate coordination (C, PDB entry: 4L2V)……8

Figure 2.5. Structures of dioxygen-incorporated intermediates after *in crystallo* reaction with 3-HAA and O_2……10

Figure 2.6 Single-crystal UV-Vis spectroscopy……11

Figure 2.7 Omit maps for 3-HAA bidentate-bound species molded using (A) superoxo species instead of 3-HAA alone and (B) 3-HAA and water-ligated Fe center instead of 3-HAA alone……12

Figure 2.8 Omit maps for dioxygen-incorporated Fe-bound superoxo-specie……13

Figure 2.9 Omit maps for dioxygen-incorporated Fe-bound alkylperoxo-species……..15

Figure 2.10. Omit maps for Fe-bound epoxide-species……16

Figure 2.11 Additional views for the structures of the epoxide intermediate showing the boat conformation……18

Figure 2.12 Omit maps for Fe-bound ACMS at early stage with all-*trans* conformation……..19

Figure 2.13 Omit maps for Fe-bound ACMS at late stage with 2,3-*cis*-4,5-*trans* conformation……20

Figure 2.14 Proposed NAD^+ biosynthesis mechanism from 3-HAA (3-hydroxyanthranilic acid)……22

Figure 2.15. Omit maps for all six of the intermediates with assignment of each claimed intermediate structure ……23

Figure 3.1 A substrate-induced loop movement around the catalytic Fe center is observed in three loop regions in HAO upon 3-HAA binding……31

Figure 3.2 Multiple HAO sequence alignment against the protein sequence of HAO from *Cupriavidus metallidurans* ……..33

Figure 3.3 Monodentately bound 3-HAA in HAO is not able to induce the loop movement……34

Figure 3.4 The relative positions of Asn27 and Ile142 and their interactions in the (A) substrate-free HAO, (B) 3-HAA monodentate bound HAO, and (C) 3-HAA bidentate bound HAO……..36

Figure 3.5 4-Cl-3-HAA bound HAO structures also turn on the closed conformation……37

Figure 3.6 Structure details on I142A HAO……..38

Figure 3.7 Single mutation of I142A disables the loop movement in HAO……..39

Figure 4.1 Crystal structure of HAO from *C. metallidurans* (from 1YFU.PDB)……43

Figure 4.2 X-band EPR spectrum of Cu-reconstituted HAO measured at 20 K with 0.02 mW microwave power……48

Figure 4.3 Mössbauer spectra of HAO reconstituted with (A) 2Fe (B) 1Cu + 1Fe (C) 1Fe + 1Cu (data: black; simulation of doublet 1: red; simulation of doublet 2: green……49

Figure 4.4 Intrinsic fluorescence spectrum of apo-HAO (black trace) quenched by titration of Fe^{2+} ion at 0.25 molar equivalent of increments…… 50

Figure 4.5 The metal sites in HAO reconstituted with different metals……..51

Figure 4.6 Stability of FeCu- and CuFe-HAO……52

Figure 4.7 Comparison of structures of Kti11p (left) and holo-HAD (right). The spheres represent the metal ions……53

Figure 4.8 Addition of apo-HAO to holo-HAO can increase the catalytic activity. The inset shows representative kinetic traces……54

Figure 5.1 The ferric, not ferrous, form of pirin substantially facilities binding of p65 to IgκB gene in SPR spectroscopy……..65

Figure 5.2. Fluorescence spectroscopic study of pirin's effect on p65's binding to the IgκB gene…….67

Figure 5.3 The function of pirin on p65 is reversible depending on the redox state of the iron center.69

Figure 5.4 Structural comparison of ferric and ferrous pirin……71

Figure 5.5 Key residues at the "active site" of pirin in the *R*-shaped surface loop including—the relative orientation and the electron densities of Arg14, Arg23, Glu32, and Lys34 in the structural data ……72

Figure 5.6 The electron density comparison of fully oxidized and reduced pirin iron centers……73

Figure 5.7 The Fe center is connected to the pirin "active site" residues (including Arg14, Arg23, Glu32, and Lys34) through a H-bond network……..74

Figure 5.8 Structural alignments of (a) Fe(III)-pirin before and after L-ascorbate soaking, and (b) comparison of the *in crystallo* reduced structure with the fully Fe(II)-pirin structure……75

Figure. 5.9 An Fe(II)-bound peroxo intermediate state of human Pirin, which is structurally similar to Fe(III)-Pirin but distinct from the Fe(II) state of pirin……..76

Figure 5.10 Structural alignments of Co(II)- (magenta, 4ERO), Mn(II)- (red, 4EWE), and Mn(III)- (purple, 4EWD) against Fe(III)-pirin (yellow, 4EWA)……77

Figure 5.11 Structural differences shown in the alignment of ferric pirin……..78

Figure 5.12 A docking model of pirin (green/yellow)-p65 (blue)-IgκB (golden/blue) supercomplex built from the corresponding crystal structures……..80

Figure 5.13 The zoomed-in view of the pirin (top, green)-p65 (bottom, cyan) interface region shows multiple complementary ion-pair interactions including K34-E234, E32-R273, R14-E279, and R23-E282 (pirin-p65)…….. 81

Figure 5.14 Mutation at the *R*-shaped surface impairs the ability of pirin to enhance the DNA binding ability of p65 to the IgκB site……..82

Figure 5.15 The proposed function of human pirin ……83

1. CUPIN SUPERFAMILY

Cupin superfamily is a structure-based classification of a protein family. All the protein members in this superfamily, although do not carry apparent sequence similarity, present an overall "jelly roll β-barrel" structural fold shown in Figure 1.1 by a few examples of the X-ray crystallographic data of the cupin proteins. The β-barrel scaffold of cupins is constituted of four pairs of antiparallel β-barrel. This superfamily was initially described by Jim M. Dunwell during studies of germins and plant storage proteins (*1*). Later, it became clear that this superfamily was built on the same structural platform (*2-4*).

According to Pfam (http://pfam.sanger.ac.uk), cupin superfamily is the functionally most diverse protein superfamily which contains more than 53 subfamilies with hundreds of thousands members across all kingdoms of life. About one third of the total population of cupins is present with only one cupin domain while the majority of the proteins contain two cupin domains.

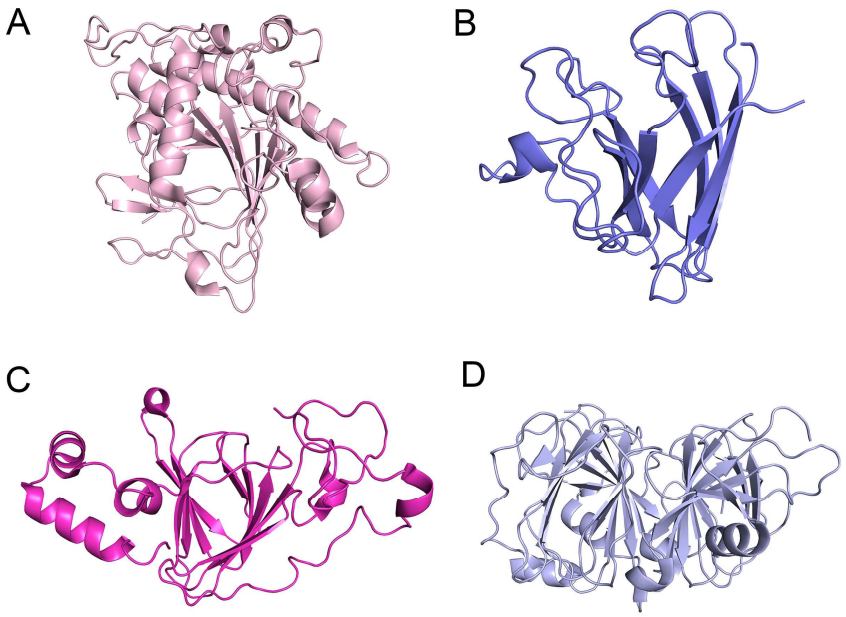

Figure 1.1. Four representative cupin proteins: (A) Isopenicillin *N* synthase (PDB: 1QJE), (B) superoxide dismutase (PDB, 2SOD), (C) oxalate oxidase (PDB: 1FI2) and (D) quercetin 2,3-dioxygenase (1JUH). Pictures were drawn by using Pymol.

Isopenicillin *N* synthase is the first structurally characterized protein in cupin superfamily (*5*). Other well-characterized protein members include, but not limit to, Mn-containing oxalate oxidase (germin) (*6*), Cu- or Fe-containing quercetin 2,3-dioxygenases (*7-9*), Fe- and Mn-superoxide dismutases (SOD) (*10*). A subgroup of metabolic modulator proteins and gene transcription regulators also belong to the cupin superfamily. However, these proteins are so far relatively poorly characterized.

Most, although not all, of the cupin proteins are metal-binding proteins. Cupins possess characteristic of two short but highly conserved amino acid sequence motifs for binding a mononuclear metal (Figure 1.2). In the absence of the structural information, the metal binding motifs shown in Figure 1.2 are often used as cupin signatures. These two motifs collectively provide up to 3 histidine and one glutamate residues for binding of a mononuclear metal ion, typically an Fe or a Cu, Mn etc.

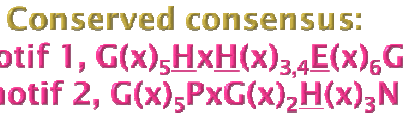

Figure 1.2 Conserved consensus in cupin superfamily proteins

Although the overall protein fold is relatively unchanged from one member to another, the metal center architecture varies and is only conserved for certain biological function. In this dissertation, the research focus has been placed on the study of two of the cupin proteins. The first of which is 3-hydroxyanthranilate-3,4-dioxygenase (HAO, also known as HAD), which is an important enzyme playing roles in amino acid catabolism, NAD^+ *de novo* biosynthesis, and toxic aromatic compound degradations. The second cupin protein selected to study is a human nuclear metalloprotein, pirin, which is a non-enzymatic member of unknown biological function. These target cupins are Fe-containing proteins. The initial protein structural information is available for both proteins (*11, 12*). The catalytic Fe in HAO is coordinated with a facile 2-His-1-carboxylate ligand motif (*13*), whereas the Fe ion in pirin is bound more

tightly to the protein with a 3-His-1-carboxylate motif. There are also apparent differences in the second ligand sphere between the two cupin Fe centers.

2. UNDERSTANDING EXTRADIOL DIOXYGENASE MECHANISM in NAD^+ BIOSYNTHESIS by VIEWING CATALYTIC INTERMEDIATES

2.1. Abstract

The synthesis of quinolinic acid from 3-hydroxyanthranilic acid is a critical step in the *de novo* biosynthesis of NAD^+ from tryptophan in mammals. By performing time-resolved *in crystallo* reactions, we observed a series of catalytic intermediates in a non-heme iron-based dioxygenase responsible for quinolinic acid production. The catalytic mechanism is visualized by structural snapshots of seven intermediates: mono- and then bidentate binding of the organic substrate, iron-bound superoxo, alkylperoxo, epoxide, and two distinct conformations of the quinolinic acid precursors. A unique metal-assisted *cis/trans* isomerization takes place in the oxygenated product to prevent it from forming quinolinic acid prior to its release from the dioxygenase. These results, especially the epoxide

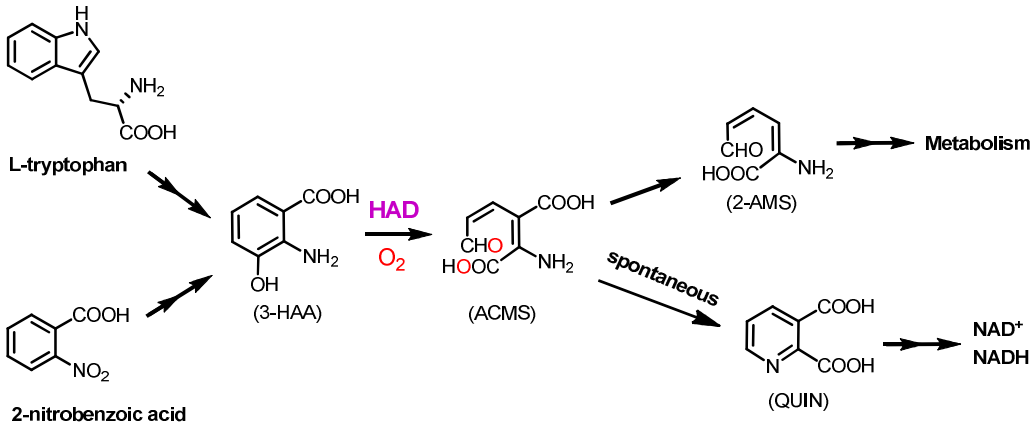

Figure 2.1 HAO occupies a central position in two biological catabolic

intermediate, define a stepwise oxygen insertion for the dioxygenation important for NAD^+ biosynthesis.

2.2 Introduction

Quinolinic acid **(**QUIN) is the universal precursor for *de novo* NAD^+ synthesis across kingdoms of life (*14*). In mammals QUIN is synthesized from the tryptophan metabolite 3-hydroxyanthranilic acid (3-HAA) via an intermediary product α-amino-β-carboxymuconate-ε-semialdehyde (ACMS) in an enzymatic step mediated by 3-hydroxyanthranilate 3,4-dioxygenase (HAO, also known as HAD or HAAO) (Figure 2.1). ACMS nonenzymatically cyclizes to yield QUIN (*15*). The dioxygenation reaction of 3-HAA for ACMS production requires O_2 and a non-heme Fe(II) ion bound in the center of a cupin structural fold in HAO (*11, 16-18*). HAO functionally belongs to the extradiol dioxygenase superfamily, which cleaves an adjacent non-hydroxylated carbon (*meta*-cleavage) rather than the carbon-carbon bond in between the substitution groups. This is the most popular ring-cleavage reaction in nature. To date, extradiol dioxygenase has more than 30,000 entries in the National Center for Biotechnology Information (NCBI) protein database and three subtypes of the enzymes are known based on the evolutionarily distinct structural folds (*19*).

A proposed oxygen activation and insertion mechanism is shown in Figure 2.2, which is based on the model established for a remotely related extradiol dioxygenase superfamily member, homoprotocatechuate 2,3-dioxygenase (2,3-HPCD) (*20*), theoretical studies (*21-24*), and the time-resolved X-ray protein crystallographic study presented below. Extradiol dioxygenases are highly efficient biocatalysts. The reaction cycles typically complete within a millisecond. Thus, it has been challenging to study the oxygen activation mechanism in this enzyme superfamily by the routine spectroscopic methodology. Two key catalytic intermediate structures, superoxo and alkylperoxo with its native substrate bound at the Fe center as well, have been characterized in 2,3-HPCD initially through the *in crystallo* reactions (*20*), an extradiol dioxygenase superfamily member structurally and evolutionally distinct from HAO. The superoxo intermediate is later to be confirmed by subsequent

spectroscopic study (*25*). Similar intermediates are needed in an enzyme such as HAO to establish the common oxygen activation feature in this superfamily. A noteworthy feature is that an active site acid catalyst, typically a conserved histidine residue, is present in those well-characterized extradiol dioxygenases to facilitate the O-O bond cleavage of the alkylperoxo intermediate to yield a gem diol species (*26*). However, such an active site amino acid catalyst is missing in HAO, although the active site structure does share most of the other common characteristics with other types of the extradiol enzymes (see Figure 2.3).

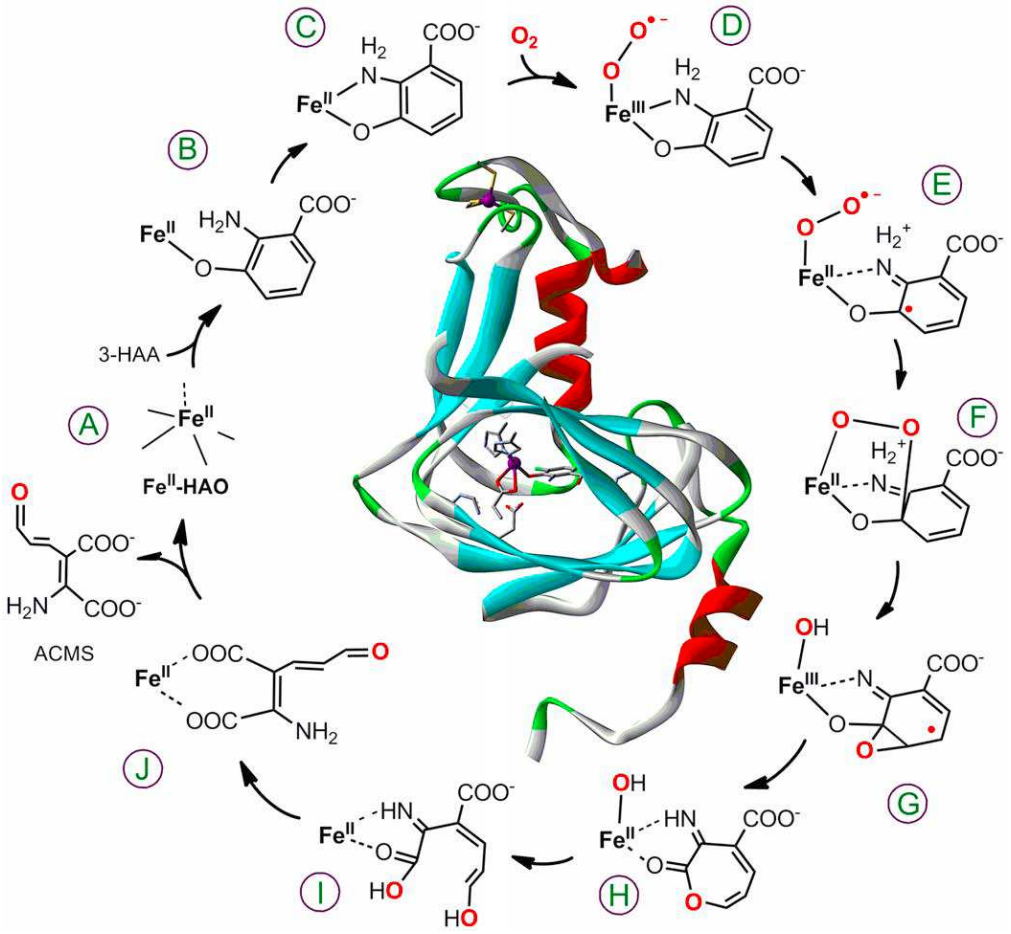

Figure 2.2 Crystal structure of HAO and the proposed catalytic cycle (A to J) based on the X-ray time-resolved crystallographic study. (A) HAO, (B) 3-HAA-bound enzyme (monodentate), (C) 3-HAA-bound enzyme (bidentate), (D) Fe^{3+}-bound superoxo, (E) Fe^{2+}-bound diradical (a resonance structure of the superoxo), (F) Fe^{2+}-bound alkyoperoxo, (G) Fe^{2+}-bound epoxide or the resonance structure Fe^{3+}-bound epoxide radical, (H) Fe^{2+}-bound ε-lactone intermediate, (I) Fe^{2+}-bound ACMS at the all-*trans* conformation, and (J) Fe^{2+}-bound ACMS at the 2,3-*cis*-4,5-*trans* conformation.

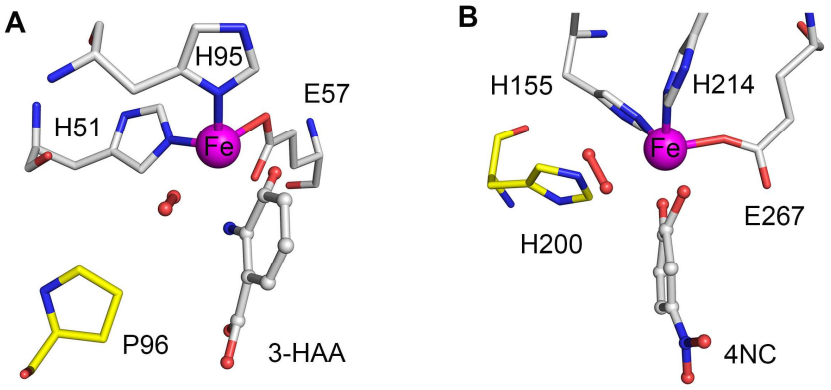

Figure 2.3 A side-by-side comparison of the HAO active site and the 2,3-HPCD catalytic center (2IGA).

2.3 Results and Discussion

In this work, important mechanistic questions such as (1) how is the organic substrate is binding to the active site, (2) what is the relative orientation between the organic substrate and O_2 in the catalytic Fe center, (3) how do the two substrates interact with each other at the first contact, (4) will the O-O bond be cleaved or the Fe-O_2 bond, (5) what are the intermediary oxygenated intermediates, and (6) what is the chemical conformation of the QUIN precursor, were asked and addressed experimentally.

2.3.1 How does the organic substrate 3-HAA bind to HAO?

The general mechanism catalyzed by non-heme Fe-dependent enzymes typically starts with chelation of the iron by the organic substrate, often a catechol compound. Substrate binding displaces one or more solvent-derived metal ligands and causes reorganization of the iron coordination sphere to open up a vacant site for the subsequent binding of O_2. The ligand-free crystal structure of HAO from *Cupriavidus metallidurans* was previously determined at 1.90 Å resolution, and the structure of the enzyme in complex with 3-HAA was solved at 3.20 Å resolution (*11*). We obtained high quality single crystals of Fe^{2+}-HAO in an anaerobic chamber. The ligand-free crystal structure was determined in $P6_522$ space group and refined to 1.74 Å resolution (Figure 2.2 inset, RCSB PDB deposition code: 4L2N). One protomer was observed per asymmetric unit, and each interacts with another protomer in a neighboring asymmetric unit giving rise to a homo-dimeric state (*11*). The catalytic iron is bound to the enzyme by a 2-His-1-Glu facial triad motif (Figure 2.4A). A second Cys_4 iron-binding site at the surface of the enzyme is also present for a non-catalytic protective role (*27*), which will be further studied in a separate effort (Chapter 4).

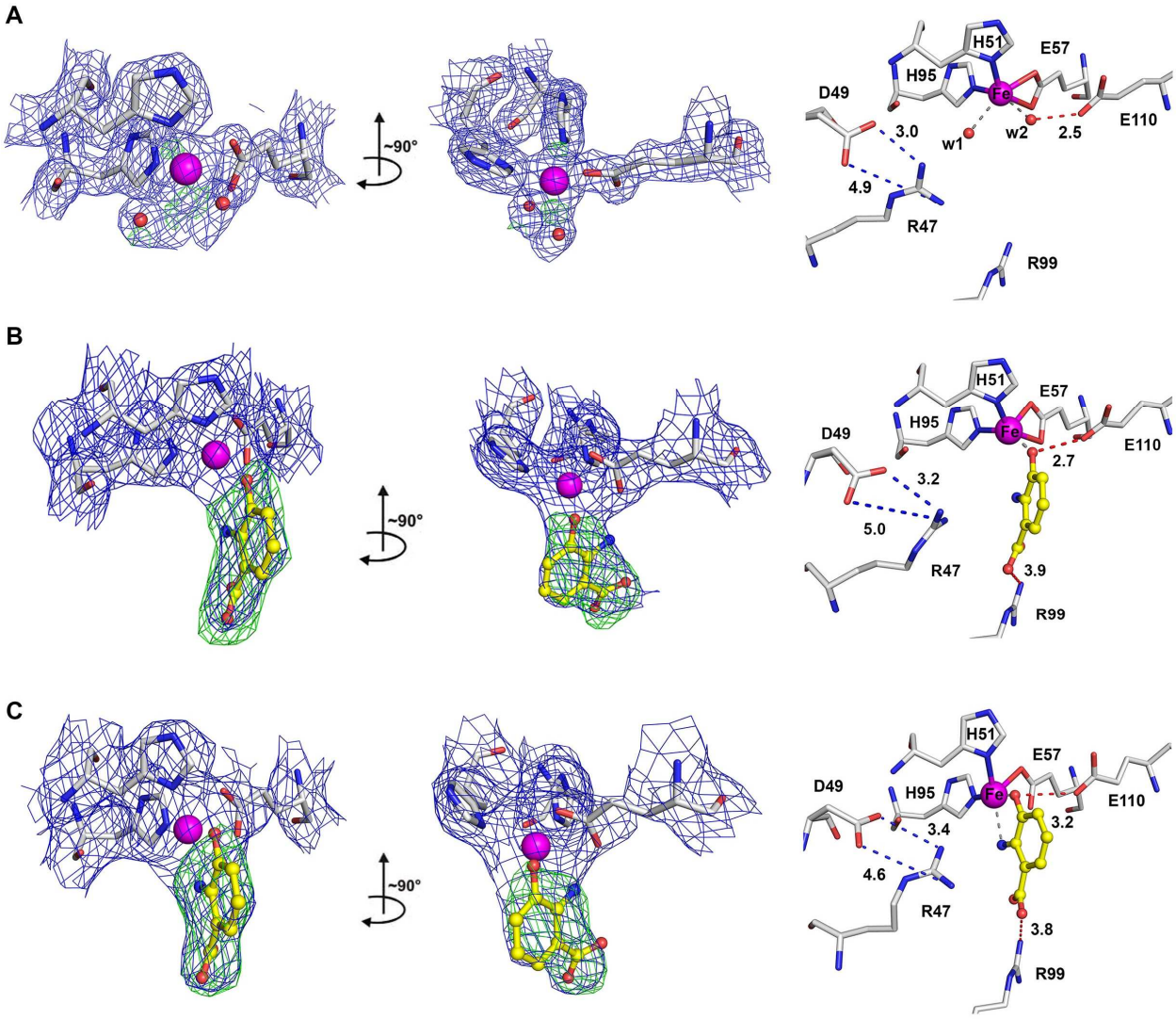

Figure 2.4. Active site structures of substrate-free (A, PDB entry: 4L2N) and substrate-bound HAO in monodentate coordination (B, PDB entry: 4L2P) and in bidentate coordination (C, PDB entry: 4L2V). The monodentate intermediate was trapped after < 30 s soaking of 3-HAA under O_2-free conditions. The $2F_o$-F_c maps are contoured at 1.0 σ. Atom color code: gray, carbon (protein residues); yellow, carbon (ligand); blue, nitrogen; red, oxygen; magenta, iron.

To study the reaction cycle by X-ray crystallography, we performed time-resolved *in crystallo* reactions in the absence (Figure 2.4) and presence (Figure 2.5) of O_2. Thousands of crystals were screened and about two hundred individual crystal diffraction data sets were collected and analyzed structurally in distinct reaction time domains, about twenty at each time point. Representative structures of seven distinct catalytic intermediates with full, or nearly full (≥ 95%), occupancy are

presented below. These intermediates are generated in a relatively high reproducible manner at specific incubation time intervals and pH, although they slightly vary due to the size differences of the crystals.

Under strict anaerobic conditions, two distinct binary complex structures were observed. An unexpected structure of monodentate-ligated enzyme-substrate complex was observed by exposing HAO crystals to the cryoprotectant containing 3-HAA for within 20 seconds. This structure was refined to 2.40 Å resolution (see Appendix Table A1) and deposited to the RCSB PDB with an entry code 4L2P. The hydroxyl group of 3-HAA coordinates the catalytic ferrous ion with a bond distance of 1.7 Å, while the amino group is 3.6 Å away from the Fe ion (Figure 2.4B). The 3-HAA is also in close contact with two active site residues. Glu110 is H-bonded to the substrate hydroxyl group (2.7 Å) and Arg99 forms a salt bridge with the carboxylate end of the substrate (3.9 Å). The carboxyl moiety of 3-HAA rotates out of the phenyl ring plane due to its interaction with Arg99. This is the first structure of a monodentally ligated enzyme-substrate complex of an extardiol dioxygease. In contrast, 30 seconds or longer 3-HAA incubation resulted in a distinct yet anticipated ligand-bound structure (Figure 2.4C). The electron density of the enzyme active site shows that the substrate binds to the iron with both the hydroxyl and amino groups. The bidentately ligated complex was refined to 2.71 Å resolution (PDB entry 4L2V). Its structure exhibits large resemblance to the previously published 3.20 Å resolution structure (1YFY.pdb) with r.m.s.d value of 0.54 over 1254 Cα atoms included in the alignment. There is no additional electron density observed for either O_2 or water at the Fe ion in these two substrate-bound structures; forcing to model O_2 molecule resulted in negative density (Figure 2.6). Given the reproducibility, it is likely that the monodentate ligation of the substrate is an intermediary state before final bidentate binding.

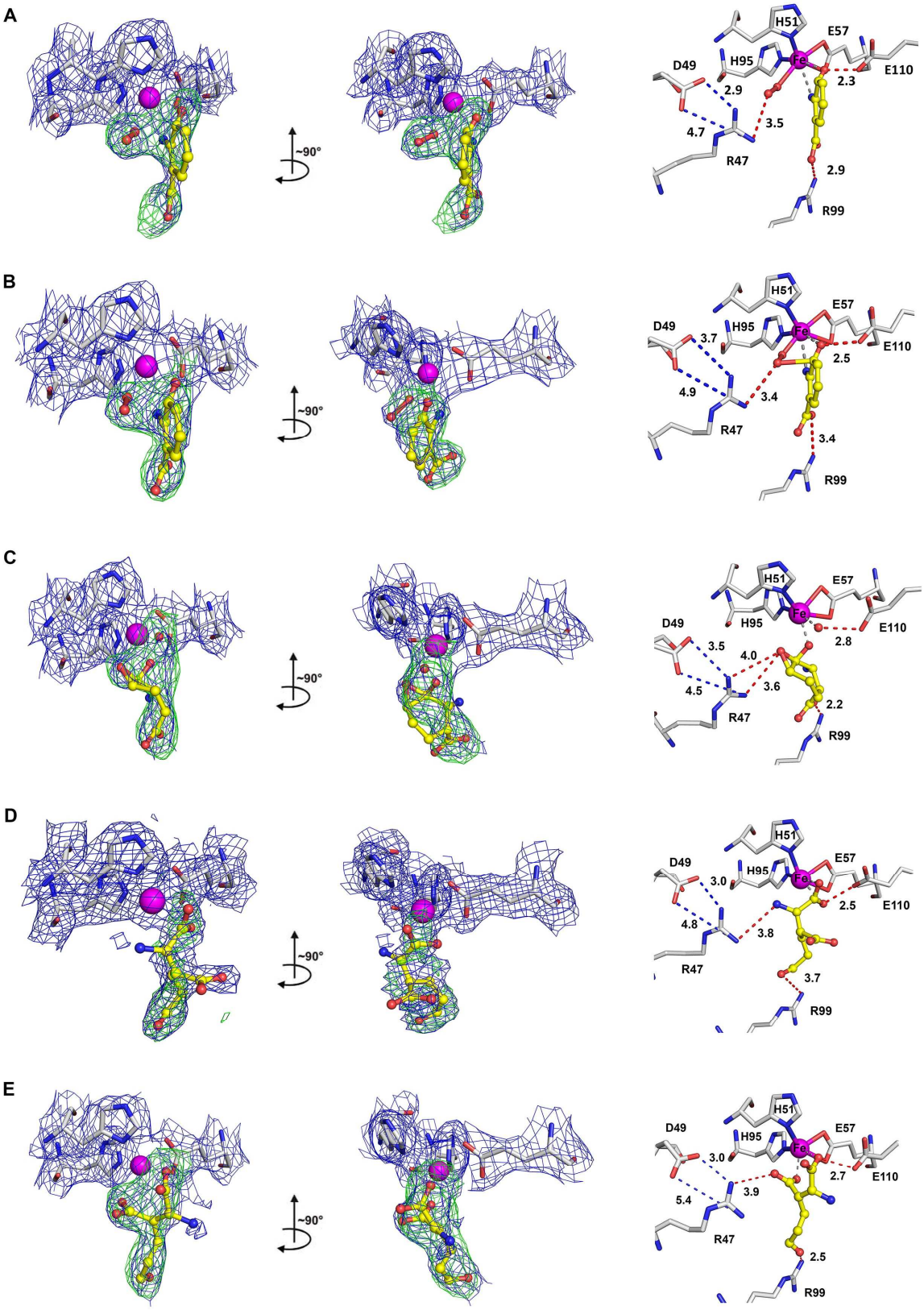

Figure 2.5. Structures of dioxygen-incorporated intermediates after *in crystallo* reaction with 3-HAA and O_2. (A) superoxo (~50 s, PDB entry: 4L2Q), (B) alkyoperoxo (~60 s, PDB entry: 4L2R), (C) epoxide (3 - 5 min, PDB entry: 4L2S), (D) all-*trans* ACMS (~ 7 - 9 min, PDB entry: 4L2T), and (E) 2,3-*cis*-4,5-*trans* ACMS (> 9 min, PDB entry: 4L2U). Atom color code: gray, carbon (HAD protein residues); yellow, carbon (ligands); blue, nitrogen; red, oxygen; magenta, iron. Red dashed lines represent hydrogen-bonding interactions (Å) while the gray dashed lines show

2.3.2 Single crystals of HAO are catalytic active

In the presence of O_2, the HAO-mediated ring-cleaving reaction which converts 3-HAA to ACMS is a rapid process. The catalytic turnover rate is 25 s^{-1} *(11)*, rendering trapping and characterization of catalytic intermediates in solution after O_2 binding infeasible. Additionally, the optical spectra of the substrate, proposed intermediates and the reaction product are very similar to each other, which make it challenging to follow by using electronic absorption spectroscopy and transient kinetics. In the current study, we noticed that the single crystals of HAO were catalytically active with its native substrates, albeit crystallized at pH 8.5 rather than the enzyme's optimal pH, 7.0. In a quartz UV-Vis cuvette containing single crystals of HAO with cryoprotectant, addition of 3-HAA under aerobic conditions resulted in the conversion of 3-HAA to QUIN via ACMS (Figure 2.6). After the reaction, the single crystals were still intact. Thus, this single crystal spectroscopic study shows that the single crystals are catalytic

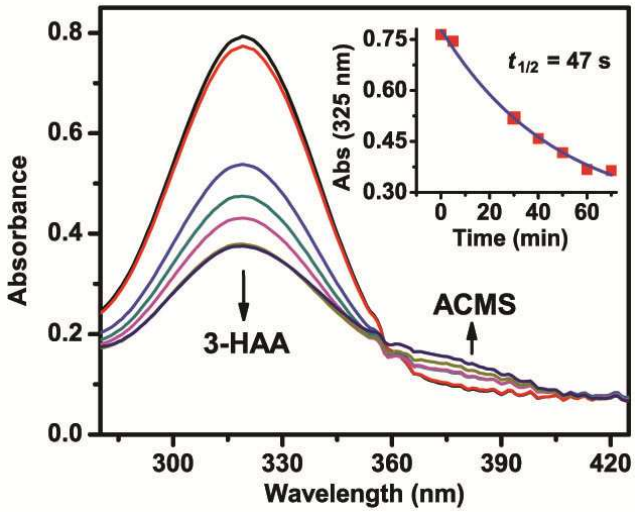

Figure 2.6 Single-crystal UV-Vis spectroscopy. The catalytic reaction was performed with seven single crystals of HAO in 450 µl cryoprotectant with seven single crystals of HAO. 3-HAA (2 µM) was added into the cuvette aerobically and its enzyme-mediated decay to QUIN was followed for 70 min. ACMS was observed as transient intermediate product. Crystals survived after completion of the catalytic reaction. The maxima of UV absorption of the substrate 3-HAA exhibits at 320 nm while the product ACMS shows absorbance at 373 nm at pH 8.5. The absorption of 3-HAA decreased at 320 nm concurrently with the increase of the ACMS formation at 373 nm. ACMS is unstable and it non-enzymatically cyclizes to QUIN, a transparent product, at a decay rate of 0.015 min^{-1} at neutral pH in solution. When the pH level increases ACMS is prone to be more unstable, and the rapid

competent.

2.3.3 Catalytically active ternary complex from O_2 binding

To capture the catalytic intermediate *in crystallo* after O_2 binding, we started to incubate the crystalline enzyme with O_2-saturated cryoprotectent containing 3-HAA. The first oxygenated intermediate structure captured between 20 – 30 seconds is shown in Figure 2.5A. At this time interval, we obtained multiple similar structures; the best X-ray diffraction dataset was used to refine an atomic model against to 2.01 Å resolution (PDB entry: 4L2Q). 3-HAA alone cannot satisfy extra electron density observed at the active site. Additional positive electron density was found in the anticipated O_2 binding site adjacent to the metal center and the bound 3-HAA (Figure 2.8A). This is the same site for O_2, or nitric oxide (NO), binding previously seen in the ternary complex structure of HAO, inhibitor 4-Cl-3-HAA and O_2 and the structure of HAO, 3-HAA and NO *(11).* Attempts to model only one oxygen or solvent molecules resulted in extra electron density (Figure 2.8B).

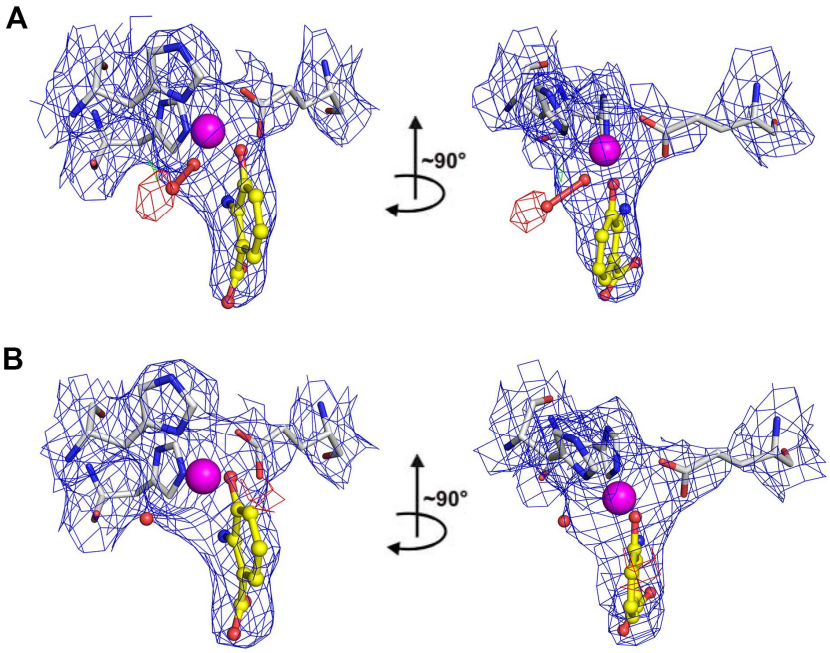

Figure 2.7 Omit maps for 3-HAA bidentate-bound species molded using (A) superoxo species instead of 3-HAA alone and (B) 3-HAA and water-ligated Fe center instead of 3-HAA alone. The blue $2F_{obs} - F_{calc}$ omit maps are contoured at 1.0 σ. The $F_{obs} - F_{calc}$ electron density maps are contoured at 3.0 σ and -3.0 σ in green and red, respectively.

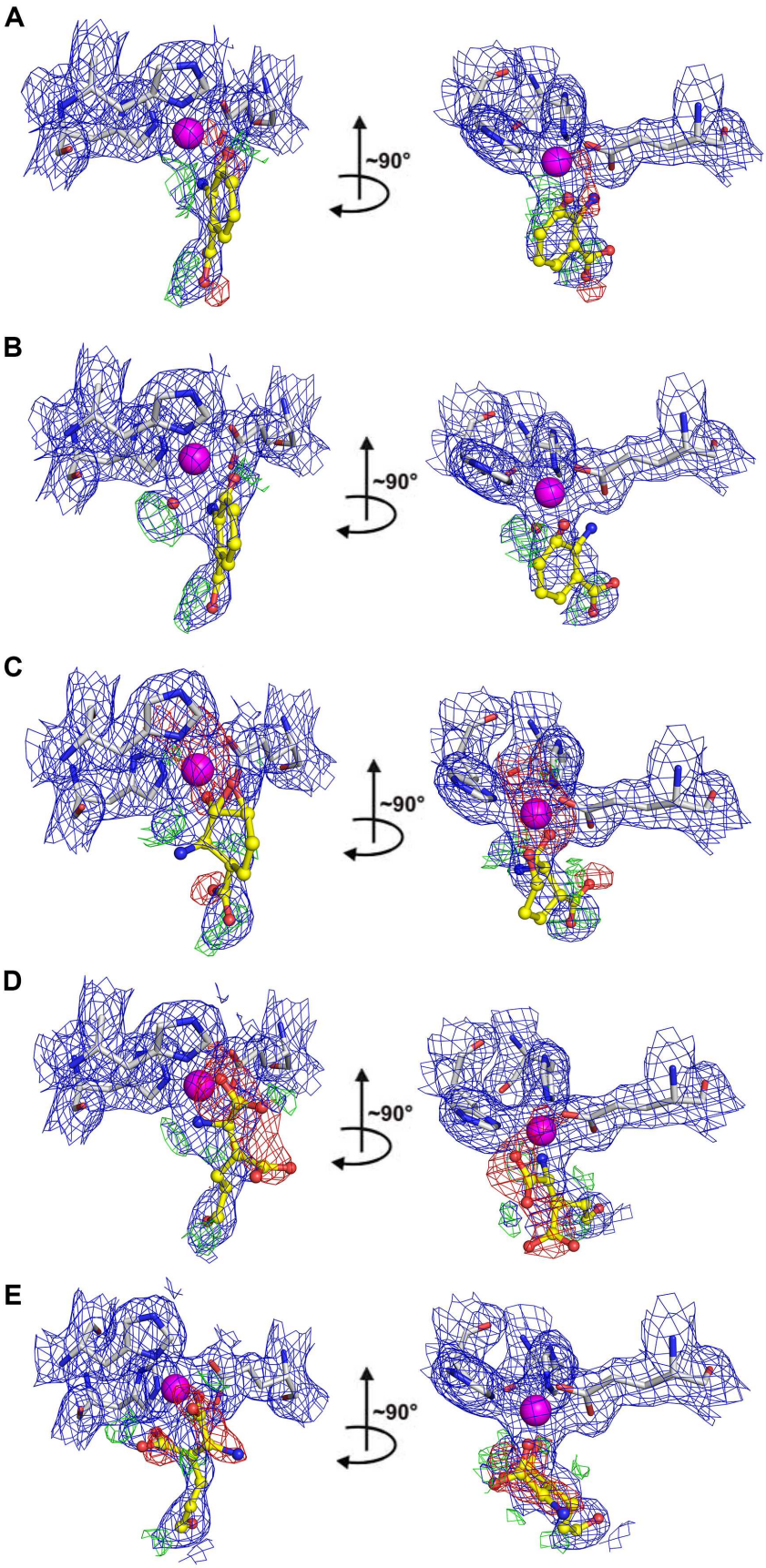

Figure 2.8 Omit maps for dioxygen-incorporated Fe-bound superoxo-species molded using (A) 3-HAA instead of the superoxo intermediate, (B) 3-HAA and one oxygen atom modeled at the adjacent side instead of the superoxo, (C) epoxide instead of the superoxo, (D) ACMS at the early stage with all-*trans* conformation instead of the superoxo, and (E) ACMS at late stage with 2,3-*cis*-4,5-*trans* conformation instead of the superoxo, respectively. The blue $2F_{obs} - F_{calc}$ omit maps are contoured at 1.0 σ. The $F_{obs} - F_{calc}$ electron density maps are contoured at 3.0 σ and -3.0 σ in green and red, respectively.

The ligand density around the Fe center cannot be modeled by later reactive intermediates other than 3-HAA and an O_2 ligand (Figure 2.8 C-E). In this intermediate, the organic substrate 3-HAA is a bidentate ligand bound to the Fe in the opposite site of the protein ligands His51, Glu57 and His95, and the O_2 is bound to the iron in a typical end-on manner. Compared to the binary complex structures obtained before O_2 incorporation, an additional noteworthy feature for the bound substrate 3-HAA is that its hydroxyl group rotates out of the ring plane, moving further close to the Glu110 residue. The dioxygen is bound to the Fe in an end-on mode. The O-O bond, refined with no bond distance pre-defined, is 1.3(4) Å, and this is consistent with a superoxo species (*20*). Depending on the oxidation state of the iron, this species can be one of the two resonance structures depicted in Figure 2.2 D and E, as previously proposed in the 2,3-HPCD study (*20*). The out-plane rotation of the hydroxyl group in the 3-HAA suggests that the organic substrate is already partially activated in this intermediate; as a result, it facilitates the radical delocalization more prone to the $C3^{3\text{-HAA}}$ – the carbon that the hydroxyl group is attached to. This altered radical delocalization is a necessary step for forming next intermediate.

2.3.4 The oxygenated intermediates

The next oxygenated intermediate was trapped in flash-cooled crystals at 50 seconds after mixing with O_2-saturated cryoprotectant and 3-HAA, which was refined to 2.50 Å (PDB entry 4L2R). Using the same refinement strategy applied to the prior intermediate, an intermediate similar to superoxo was obtained (Figure 2.5B). A notable difference, however, between this later intermediate and the prior superoxo is that this structure shows a much shorter distance between $O2^{O2}$ to $C4_{3\text{-HAA}}$ (2.3 compared to 3.5 Å), suggesting that an incipient bond is forming from the prior intermediate. This species is consistent with an Fe(II)-alkylperoxo intermediate, and the distal oxygen atom of O_2 has begun to form a covalent bond with the organic substrate. The 1.76 Å length O-O distance is particularly noteworthy as it is much longer than what it is normally observed 1.21 Å for O_2 and 1.33 Å for superoxo (*28*). Attempts to model this intermediate by the superoxo or other intermediates of the catalytic cycle

resulted in obvious negative and/or positive densities around the iron center (Figure 2.8). In this alkylperoxo intermediate, the substrate amino group is in an ideal position to function as an acid catalyst to facilitate O-O bond cleavage. With metal chelation and increased hydrophobicity in the enzyme, the pK_a of the 3-HAA amino group would be significantly shifted. This observation provides a plausible explanation for a missing active site acid catalyst.

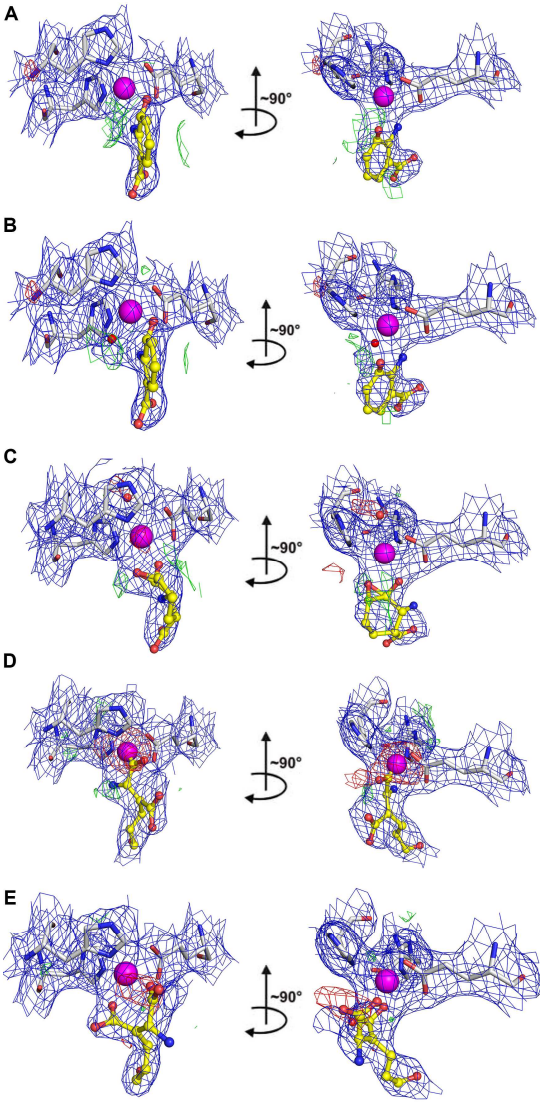

Figure 2.9 Omit maps for dioxygen-incorporated Fe-bound alkylperoxo-species molded using (A) 3-HAA instead of the alkylperoxo intermediate, (B) 3-HAA and one oxygen atom modeled at the adjacent side instead of the alkylperoxo species, (C) epoxide intermediate instead of the alkylperoxo, (D) all-*trans* ACMS instead of the alkylperoxo, and (E) 2,3-*cis*-4,5-*trans* ACMS instead of the alkyloxo species. The blue $2F_{obs} - F_{calc}$ omit maps are contoured at 1.0 σ. The $F_{obs} - F_{calc}$ electron density maps are contoured at 3.0 σ and -3.0 σ in green and red, respectively.

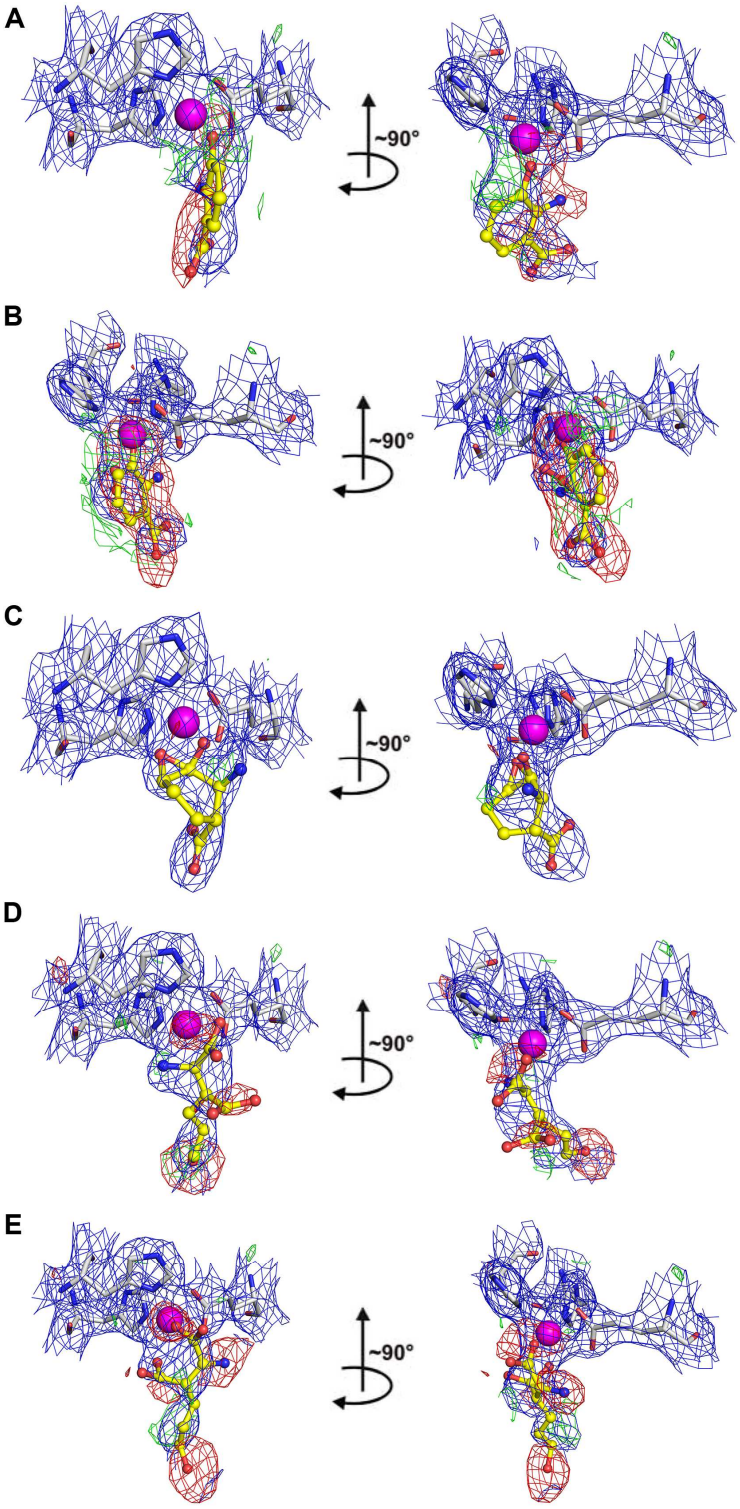

Figure 2.10. Omit maps for Fe-bound epoxide-species molded using (A) 3-HAA instead of epoxide, (B) superoxo-species, (C) epoxide-species in short of the proximal oxygen, (D) all-*trans* ACMS, (E) 2,3-*cis*-4,5-*trans* ACMS. The blue $2F_{obs} - F_{calc}$ omit maps are contoured at 1.0 σ. The $F_{obs} - F_{calc}$ electron density maps in A, B, D, and E are contoured at 3.0 σ and -3.0 σ in green and red, respectively; The maps in C are contoured at 3.3 σ and -3.3 σ in green and red, respectively.

At 5 minutes, a new species with external ligand at the iron center exhibits a highly constrained conformation (Figure 2.5C). The distal oxygen of the dioxygen is incorporated to the 3-HAA between the C3 and C4 carbon, forming a three-member ring epoxide while the proximal oxygen remains bound to the Fe ion and is stabilized by Glu110 through H-bound interactions. The best dataset of this intermediate was refined an atomic model against 2.40 Å resolution (PDB entry: 4L2S). Likewise, attempts to model this dataset with other catalytic intermediate were unsuccessful (Figure 2.10). The oxygen insertion to the organic substrate caused a substantial distortion of its phenyl ring; as a result, the epoxide intermediate is far from planer but instead in a slightly distorted boat conformation. The zoom-in view of epoxide of multiple viewing angles is shown in Figure 2.11. The epoxide oxygen is stabilized by Arg47; a residue appears to be the companion of the distal oxygen atom till this step. We attempted to analyze this species by other models. However, the F_o-F_c maps suggest that none of them can fit the electron density (Figure 2.11). Among these improper models, epoxide without the proximal oxygen bound to iron fits the electron density better than the others, except an extra electron density demanding the presence of the proximal oxygen (Figure 2.8). The structural characterization of Fe-bound epoxide intermediate makes it clear that the oxygen insertion is conducted in a stepwise manner, rather than concerted, in this dioxygenase reaction. Though it has been predicted by theoretical studies (*21-24*), this epoxide intermediate had not been observed or structurally characterized from any dioxygenases.

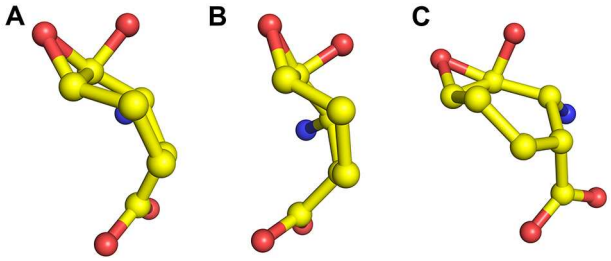

Figure 2.11 Additional views for the structures of the epoxide intermediate showing the boat conformation.

2.3.5 The intermediate product bound HAO complexes

Seven minutes and longer reaction granted two intermediary product species (Figure 2.5 D and E). In both structures, the aromaticity of the substrate 3-HAA is broken. The Fe center is bound with an exogenous organic ligand in linear structural form in both intermediates and they are not identical to each other (Figure 2.5 D and E). Modeling ACMS fitted well into the electron densities. In the intermediate trapped after 7 - 9 min of the *in crystallo* reaction (refined to 2.06 Å resolution, PDB entry 4L2T), the well-defined electron density map shows that the ligand is an ACMS in its all-*trans* conformation, with a newly formed carboxylate group bidentately coordinated to the iron and the original amino group close to, but not coordinating the iron. In the second ACMS-bound structure, which was obtained from longer reaction time (> 11 min), the product is in the 2,3-*cis*-4,5-*trans* conformation (refined to 2.30 Å resolution, PDB entry 4L2U). Interestingly, the model was built by using the all-*trans* ACMS as the starting ligand, but it ended up with a distinct conformation after fitting with the electron density. The 2,3-*cis*-4,5-*trans* ACMS coordinates to the Fe in a bidentate manner by its oxygen atoms from each carboxylate group, at the distance of 2.7 and 2.3 Å, respectively. Neither swapping the two ACMS-bound models nor any other intermediates of Figure 2.2 fits the corresponding electron densities (Figures 2.12 and 2.13). There is no final product QUIN-bound structure obtained in any of the hundred structures solved from *in crystallo* reactions with a time frame up to two days. The 2,3-*cis*-4,5-*trans*

ACMS and ligand-free HAO structures were observed in the crystals of those from prolonged reaction times. Apparently, ACMS releasing appears to be the rate-limiting step in the *in crystallo* reaction.

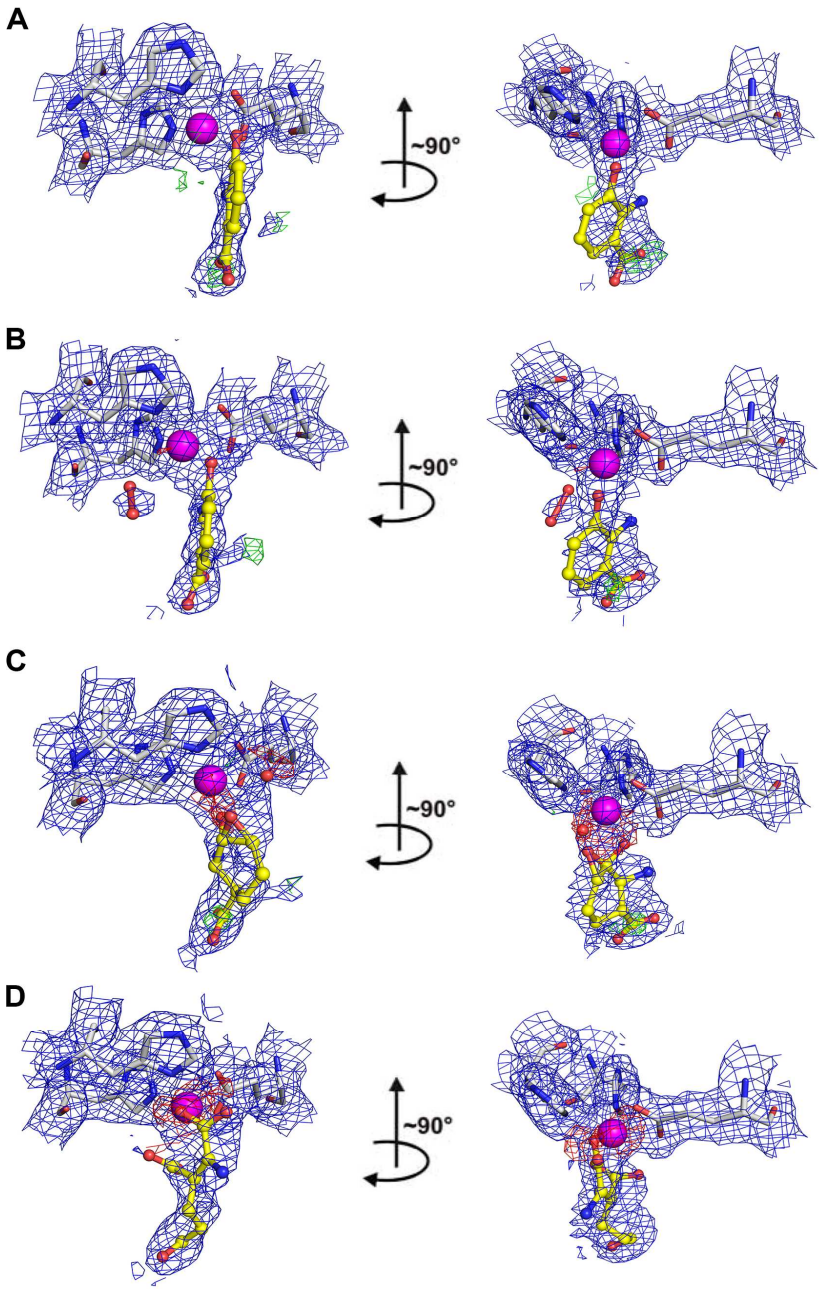

Figure 2.12 Omit maps for Fe-bound ACMS at early stage with all-*trans* conformation molded using (A) 3-HAA instead of ACMS, (B) superoxo-species, (C) epoxide-species in short of the proximal oxygen, and (D) ACMS at the late stage with 2,3-*cis*-4,5-*trans* conformation, respectively. The blue $2F_{obs} - F_{calc}$ omit maps are contoured at 1.0 σ. The $F_{obs} - F_{calc}$ electron density maps are contoured at 3.0 σ and -3.0 σ in green and red, respectively.

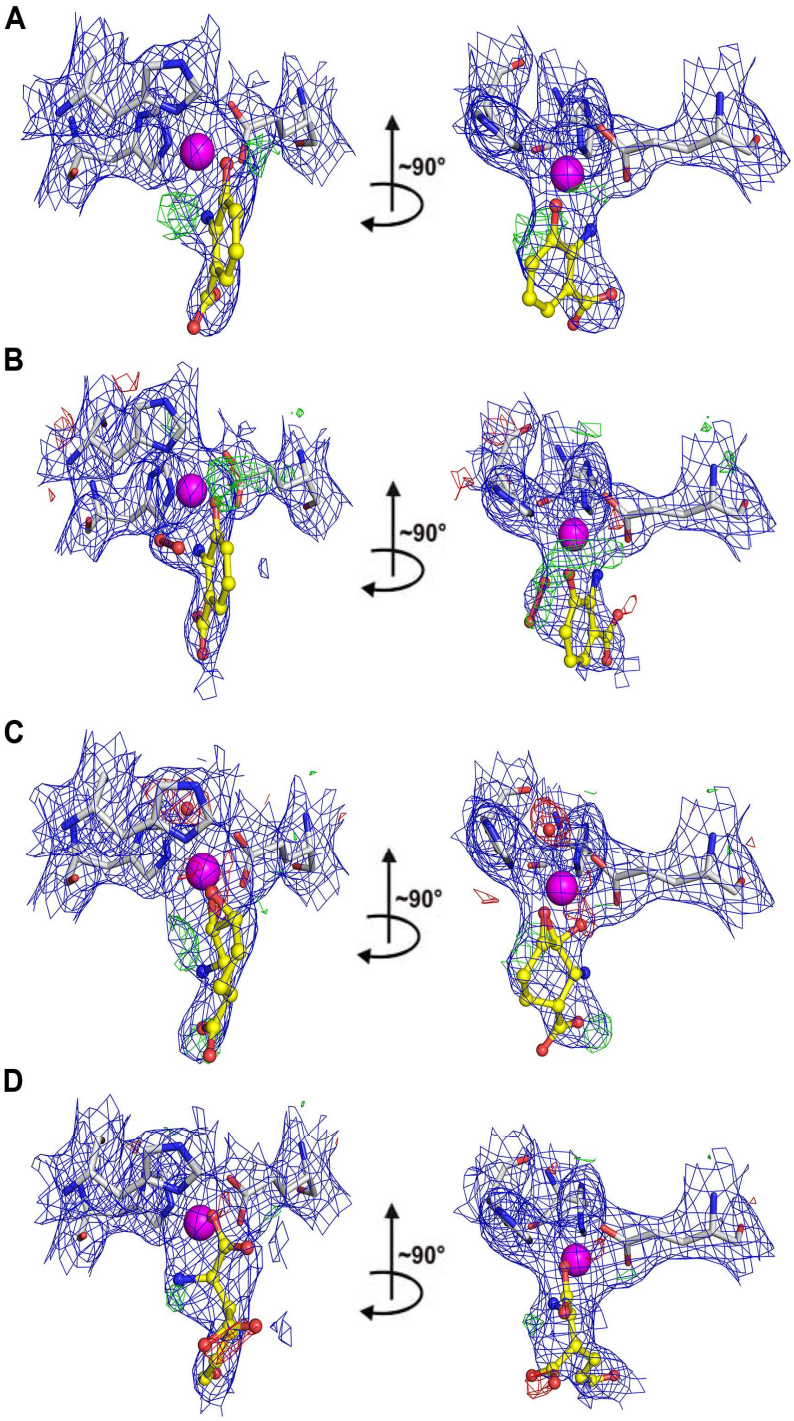

Figure 2.13 Omit maps for Fe-bound ACMS at late stage with 2,3-*cis*-4,5-*trans* conformation molded using (A) 3-HAA instead of ACMS, (B) superoxo species instead of ACMS, (C) epoxide species instead of ACMS, and (D) all-*trans* instead 2,3-*cis*-4,5-*trans* ACMS, respectively. The blue $2F_{obs} - F_{calc}$ omit maps are contoured at 1.0 σ. The $F_{obs} - F_{calc}$ electron density maps are contoured at 3.0 σ and -3.0 σ in green and red, respectively.

The ACMS-bound structures represent the first attempt to determine the crystal structure of an unstable intermediary product in QUIN synthesis. Chemically, ACMS has many different conformations as shown in the NMR study of an analogue compound (*15*). It was known that the all-*trans* form is the most stable conformation of ACMS while the all-*cis* counterpart is the most likely form to autocyclize via an electrocylic reaction (*15*), and also that the 2,3-*trans*-4,5-*cis* form is proposed to be the last isomer prior to the all-*cis*. Interestingly, the ACMS made by HAO is in neither 2,3-*trans*-4,5-*cis* nor all-*cis* conformation. Our results show that a metal-assisted *cis/trans* isomerization converts the all-*trans* to the 2,3-*cis*-4,5-*trans* form for final release. This intermediary product is in a structurally remote configuration from the anticipated 2,3-*trans*-4,5-*cis* form (Figure 2.2). Thus, the dioxygenase is preventing ACMS from autocyclization so that it will not generate QUIN inside the enzyme and that a portion may be safely taken or delivered to the active site of the downstream enzyme of the kynurenine pathway, to avoid overproduction of QUIN, a compound which is excitotoxic causes excessive stimulation of nerve cells at overwhelmed concentrations (*29, 30*). The kynurenine pathway partitions for the fate of ACMS. A decarboxylase competes with the non-enzymatic reaction to direct the metabolic flux to either acetyl-CoA (*31, 32*) or glutaryl-CoA (*33*). At pH 7.0 and room temperature, the half-life time of ACMS is 43 min in our determination and this will be significantly shorter at higher pH and temepratures. The HAO-assisted *cis/trans* isomerization is important for keeping enough non-cyclized ACMS and this is likely part of a natural strategy to control the branched pathways while one pathway reaction is enzymatic and the other is spontaneous and nonenzymatic .

An intriguing observation is that the ACMS automatically adjusts the orientation prior to its departure from the catalytic iron. The metal-assisted *trans*-to-*cis* transition would not be able to take place with a double bound presenting between the C2 and C3 of ACMS. In the newly formed ACMS, the 2,3-bond is not a double bond due to the bidentate ligation of the carboxyl and amino groups to the iron. Thus, the enzyme completes such a transition and naturally, the amino group switches off from the

metal and the carboxylate group becomes a metal ligand once the metal-assisted *cis/trans* isomerization is complete. Although the all-*trans* conformation is the most stable form of ACMS, the constrain forces resulted from the epoxide intermediate would make this metal-bound ACMS a transient species. Like the monodentate ligated 3-HAA shown in Figure 2.4B, the all-*trans* ACMS is probably trappable only

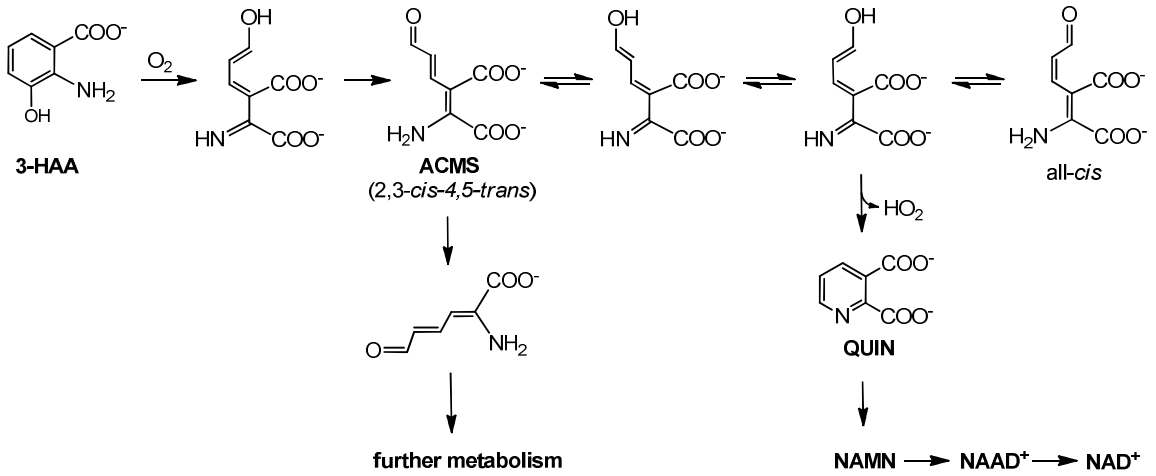

Figure 2.14 Proposed NAD^+ biosynthesis mechanism from 3-HAA (3-hydroxyanthranilic acid). NaMN (nicotinic acid mononucleotide) and NaAD (nicotinic acid adenine dinucleotide) are the intermediates from QUIN (quinolinic acid) to NAD^+ (nicotinamide adenine dinucleotide).

because the reaction is in inside the crystal.

With a total of seven intermediate crystal structures and an improved enzyme-alone structure, the current study provides support for the general oxygen activation characters of the Fe dioxygenase and leads to comprehension for the first time the mechanism of QUIN production for NAD^+ biosynthesis (Figure 2.14). The model shown in Figure 2.2 is also the first mechanistic cycle for an extradiol dioxygenase lacking the active site histidine for promoting O-O bond cleavage. The epoxide structure has been proposed in both heme and non-heme dioxgenases as a key intermediate, such as heme-dependent tryptophan dioxygenase (*34-36*), but has not been structurally characterized until this work. The characterization of this intermediate provides the most solid evidence that a large fraction of the dioxygenases performs oxygen atom transfer to the organic substrate in a stepwise fashion.

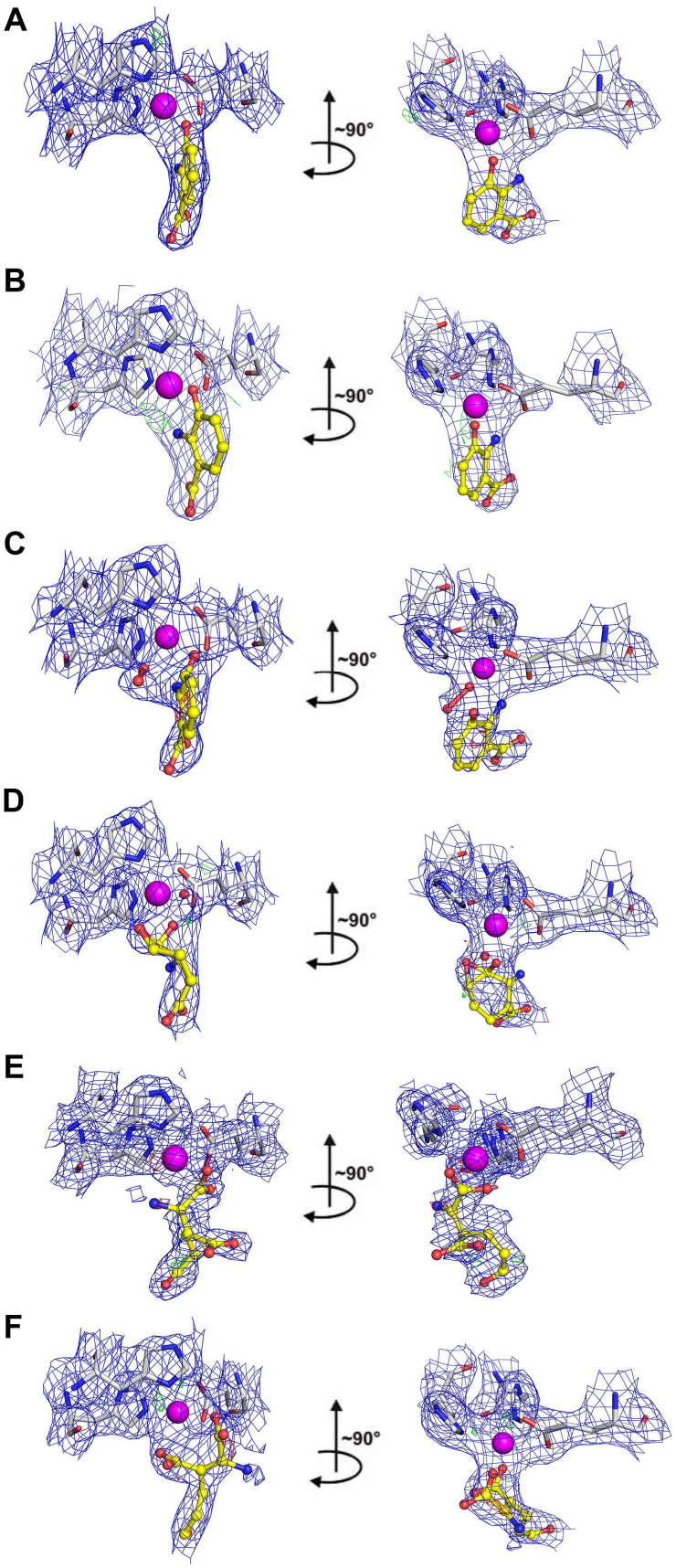

Figure 2.15. Omit maps for all six of the intermediates with assignment of each claimed intermediate structure (A) 3-HAA monodentately bound to the Fe ion, (B) bidentate ligand, (C) alkylperoxo, (D) epoxide, (E) all-*trans* ACMS, (F) 2,3-*cis*-4,5-*trans* ACMS. The blue $2F_{obs} - F_{calc}$ omit maps are contoured at 1.0 σ. The $F_{obs} - F_{calc}$ electron density maps in A, B, D, and E are contoured at 3.0 σ and -3.0 σ in green and red, respectively; The maps in C are contoured at 3.3 σ and -3.3 σ in green and red, respectively.

2.5 Further experimental details

Materials—3-hydroxyanthranilic acid, ammonium iron(II) sulfate (99.997%), ascorbate, and glycerol were the highest grades purchased from Sigma-Aldrich and used without further purification.

Expression and purification—The HAO gene from *Cupriavidus metallidurans* was overexpressed in *Escherichia coli* (DE3) cells (Novagen) and purified by nickel affinity chromatography as previously described (7, 19). Purified protein was reconstituted with five equivalents of $NH_4Fe(SO_4)_2$ anaerobically. The resultant protein then underwent size exclusion column Superdex 200 which is equilibrated with Tris-HCl buffer (10 mM, pH 7.6) containing 2 mM DTT and 5% glycerol.

HAO in crystallo reaction—Full length (1 – 174 amino acid) HAO proteins were crystallized by optimization of conditions previously established using hanging drop vapor diffusion in VDX plates (Hampton Research). Single crystals suitable for X-ray data collection were obtained from drops assembled with 1 µL protein solution layered with 1 µL reservoir solution containing 0.1 M Tris pH 8.5, 0.2 M $MgCl_2$, 1 mM DTT, 18% PEG 8000. Crystal growth took place in a vibration-free crystal growth refrigerator from Molecular Dimensions at 16 °C. In order to trap the binary complex of enzyme and substrate, the *in crystallo* reaction was firstly performed by exposing single HAO crystals in the solution (0.1 M Tris-HCl pH 8.5, 0.2 M $MgCl_2$, 20% PEG 8000) supplemented with 1mM 3-HAA in anaerobic chamber. The 3-HAA monodentate-bound HAO was trapped by exposing single crystals with 3-HAA in cryoprotectant within 20 seconds while the 3-HAA-chelated HAO was captured in exposing time of 30 seconds. The *in crystallo* reaction was then carried out with the cryoprotectant containing 3-HAA and also being purged with O_2 for 30 min prior to mixing with crystalline enzymes. The crystals were exposed to the aforementioned reaction solution for different periods of time of 50 seconds, 1, 3, 5, 7 and 13 minutes. For each of the time scale, single crystals were mounted in small loops of fine rayon fiber and flash-cooled directly in liquid nitrogen after being dipped into the cryoprotectant solution that

contained 0.1 M Tris-HCl (pH 8.5), 0.2 M $MgCl_2$, 20% PEG 8000 30% glycerol for individual structural determination.

X-ray Data Collection and refinement—X-ray diffraction data were collected at the SER-CAT beamline 22-ID or beamline 22-BM at the Advanced Photon Source (APS), Argonne National Laboratory, Argonne, IL. All data collection was performed at 100 K. The diffraction data was indexed, integrated and scaled with HKL2000 (*37*). The structures were solved by molecular replacement using MOLREP (*38*) program of the CCP4 suite (*39*) with holo-HAO (PDB accession number 1YFU) as search model. Link restraints to Fe were removed from the refinement to avoid bias in the refined Fe-ligand distance. Electron density was fitted and refined using Coot (*40*), Phaser (*41*) and REFMAC (*42*).

Ligand Refinement and molecular modeling—In order to avoid bias in model building, ligand refinement was initiated at the final stage of the structure refinement by examining ligand-omit difference maps. 3-HAA was employed as the initial ligand model for all intermediate structures and the proper ligands were modeled into the density by checking on the $F_{obs} - F_{cal}$ maps. The dictionaries for the 3-HAA derived Fe(II)-superoxo, alkylperoxo, epoxide, and ACMS intermediates were generated with Phaser (*41*). Among the structures determined, some of which exhibit overlapping intermediate states and the density cannot be fitted by one single intermediate structure. These overlapping structures were excluded for further analysis because of heterogeneous nature. Only the intermediates with ligands occupancy between 90 - 100%, including all the carbon, oxygen and nitrogen atoms, were analyzed further. The structures with the best resolution in each intermediate are shown in the results. The blue $2F_o$-F_c maps resultant from the metal-ligands His51, Glu57 and His95 as well as active-site ligand are contoured at 1.0 σ. Finally, the active site ligands were removed and the resultant ligand-free structures were refined with five cycles of restrained refinement for preparation of the difference maps. The resultant positive density (green) contoured at 3.0 σ is in agreement with the corresponding active site ligand in all models (Figure 2.15). In the ligand-free enzyme (Figure 2.4A), we observed extra

election density at the catalytic iron center which can be accommodated by two water molecules. Strong spherical density is observed in the pocket created by residues Val41, Arg47, Pro97 and Arg99 at the bottom of the substrate–binding cleft, and it is assigned to an Cl^- anion. The presence of the Cl^- is the structural signature of the resting state of HAO enzyme in ligand-free form (*11*). Checking for the presence of this Cl^- anion and the occupancy of the candidate ligand were the two beginning steps in the intermediate ligand refinement. Two distinct substrate-bound HAO structures (Figure 2.4B and Figure 2.4C) were obtained under anaerobic conditions by soaking argon-saturated O_2-free 3-HAA in the cryoprotectant. We initiated our ligand fitting with 3-HAA. After 3-HAA was modeled into the structure, it became clear that no extra electron density for O_2 around the catalytic iron center. To ensure that no oxygen species present in these two structures, we also attempted to model dioxygen into these structures. The fitting and refinement were performed exactly the same manner as what was carried out on the oxygen-free ligand structure. The result revealed negative density at the site of the modeled dioxygen, while the electron density on 3-HAA was undisturbed (for one of these, see Figure 2.6).

For the five dioxygen-incorporated structures presented in this study, ligand modeling was initiated with 3-HAA as well, however, none of the active site in those intermediates contained 3-HAA in an unaltered form. Sequentially fitting the density features with the candidate ligands proposed from the mechanistic cycle was applied instead of using the non-crystallographic symmetry (NCS) restraints refinement in the PHENIX suite (*43*). The candidate ligands include 3-HAA, 3-HAA-Fe-superoxo, 3HAA-Fe-alkylperoxo, Fe-epoxide intermediate and the ring-opening product, ACMS, in two distinct conformations. Each of the candidate ligands was fitted into the data sets individually. These ligands satisfied the respective extra electron density at the active site distinctly.

As discussed earlier, one dioxygen-incorporated species was assigned as Fe-bound superoxo species of HAO. We refined this species with sole 3-HAA and it resulted in both positive and negative electron densities around 3-HAA. In addition, the superimposition of the superoxo structure with either

the determined monodentate-bound 3-HAA or bidentate-bound 3-HAA shows large differences at the orientations of the metal-ligands and 3-HAA. Nevertheless, if only one oxygen atom is positioned adjacent to 3-HAA, positive density is clearly revealed suggesting a missing oxygen atom. We further fitted and refined with epoxide, ACMS at the early and late stage. However, none of them is able to satisfy the extra electron density at the active site (Figure 2.8).

The fourth structure shown in the result section was assigned as an alkylperoxo intermediate. Likewise, we attempted to fit and refine it with different ligands by using the same strategy as described above. As shown in Figure 2.9, the green positive electron density adjacent to 3-HAA suggests a missing oxygen atom or atoms in the structures of Figure 2.9 (A and B). When this species was assigned to an epoxide intermediate, there was no density to cover the proximal oxygen (Figure 2.9C). The assignment of this species to an ACMS also results in unsatisfied electron density (Figure 2.9 D and E).

The fifth structure shown in the main text was assigned as an epoxide intermediate. Figure 2.10 shows that none of the other catalytic cycle intermediates would satisfy the extra electron density at the active site with the exception of the epoxide species. Moreover, if we fit the epoxide ligand without the proximal oxygen, the positive density (green) appears (Figure 2.10C) and this unassigned density can be satisfied by simply fitting the proximal oxygen back to the corresponding position. As we observed in fitting to the 2,3-*cis*-4,5-*trans* conformation with Fe-bound all-trans ACMS, negative electron density around the newly degenerated carboxyl group suggests mis-assignment.

The sixth structure shown in the main text was assigned as an iron-bound all-*trans* ACMS. As shown in Figure 2.12, the extra electron density at the active site cannot be covered either by 3-HAA, superoxo, epoxide and the 2,3-*cis*-4,5-*trans* ACMS which was trapped at a later stage.

The seventh structure shown in the main text was assigned as an iron-bound 2,3-*cis*-4,5-*trans* ACMS. Fitting of different ligands was similarly performed as described above. Figure 2.13D shows the fitting results of refining ACMS to the all-*trans* conformation to the structure. Positive electron density is

observed at the amino moiety while the negative electron density at the newly generated carboxyl group, suggesting such an assignment of the ACMS conformation is inconsistent to the experimental data. The major difference in the electron densities between ACMS at the early and late stages (Figure 2.13) is the shift of the electron density of the original carboxyl group of the 3-HAA. This electron density includes one carbon and two oxygen atoms. In contrast, the amino group has only electron density for the nitrogen atom. The relative orientation of the carboxyl group and amino group is distinct in the assigned confirmations. The bulky density belonging to the carboxyl group is away from the catalytic iron in the all-*trans* ACMS structure whereas it is close to the iron in the 2,3-*cis*-4,5-*trans* ACMS structure.

Reproducibility—We performed time-resolved *in crystallo* reactions with the native substrate of HAO and O_2. At each of the incubation time-scale, 20+ crystals were frozen down and structurally determined through X-ray diffraction data collections and subsequent data analyses. Each of the catalytic intermediates presented in the main text was also observed in additional structural data sets of various resolutions. Among those, the binary enzyme-substrate complex and the product-bound enzyme were easier to obtain because they are relatively stable with respect of other catalytic intermediates. The product ACMS is unstable and thus it is not possible to perform soaking experiment to the crystalline enzyme to compare with the *in crystallo* reaction results. Among the crystal structures determined at the same time scale, the best-fit structures were chosen to represent the corresponding intermediates based on the following criteria: 1) occupancy of each of the atoms in the catalytic intermediates is above 90%, 2) the positions of the carbon atoms are at the center of the electron density, 3) the refined structure with the defined catalytic intermediate does not show apparently different temperature factors with the surrounding amino acid residues, 4) the ligand presents sounded bond-lengths and interactions among the intermediate and the surroundings. These criteria enabled us to rule out the overlapping structures of the intermediates species.

3. SUBSTRATE-INDUCED LOOP MOVEMENT IS ESSENCIAL FOR RAPID OXYGEN INCORPORATION IN 3-HYDROXYGANTHRANILIAT 3,4-DIOXYGENASE

3.1 Abstract

3-hydroxyanthranilate dioxygenase (HAO) exists in the tryptophan degradation pathway in eukaryotic species, a pathway which is responsible for energy production and NAD^+ biosynthesis. It also independently exists in the 2-nitrobenzoic acid degradation pathway in prokaryotic species for energy supplementation. Crystal structures of HAO have been determined from multiple sources. The substrate-bound structure shows a closed conformation in contrast to the open conformation. We determined six more structures of HAO and the HAO variant, in substrate-free and substrate/inhibitor-bound forms. These structures provide a clear depiction of ligand-induced loop movement in three specific loop regions adjacent to the catalytic center. A significant increase in hydrophobicity at the iron center is observed as the consequence of the concerted loop movements due to binding of the organic substrate. Due to the inherent hydrophobic character of O_2, such an increased Fe-center hydrophobicity is proposed to be essential for rapid O_2 binding and activation. Asn27 and Ile142 are identified as two key residues to orchestrate the structural reorganization in response to the organic substrate's binding. A single mutation at Ile142 to alanine abolished the loop-movement. Taken together, these structural studies provide a model to explain how the proficient non-heme Fe dioxygenases enrich O_2 from bulk solvent to fulfill a high catalytic rate.

3.2 Introduction

The ring-cleaving dioxygenase enzymes are abundant and versatile in nature (*44*). These enzymes are proficient, with catalytic rate constants faster enough to escape spectroscopic characterization of their catalytic intermediates. The activation of O_2 in these enzymes is typically accomplished by a mononuclear non-heme metal center to activate O_2 (*45*). A fundamental question remain to be answered is that how these enzymes are succeeded in a rapid O_2 binding which is necessary for the

observed catalytic rates while local O_2 concentration in aqueous solution is at low levels (200 – 300 μM at 1 atom pressure and room temperature).

Here, we chose a ring-cleaving dioxygenase as a model system for the study of this problem. 3-Hydroxyanthranilate dioxygenase (HAO) is a non-heme iron-dependent extradiol dioxygenase belonging to the cupin superfamily (*11, 16, 17*). This enzyme cleaves the phenol ring adjacent to the substitution groups. It activates and inserts dioxygen across the 3,4-bond of its substrate 3-hydroxyanthranilate, ultimately producing quinolinic acid via the intermediary product α-amino-β-carboxymuconate-ε-semialdehyde (ACMS) (see Figure 2.1, Chapter 2). HAO is present in the kynurenine pathway of eukaryotic organisms where it is essential for NAD^+ biosynthesis and tryptophan degradation. It is also found in the 2-nitrobenzoic acid (2-NBA) pathway of certain prokaryotes where it is responsible for ring-cleavage for energy production.

HAO from *Cupriavidus metallidurans* has been shown to operate at a catalytic turnover rate of 25 s^{-1} (*11, 27*). We were curious how this enzyme enhances oxygen absorption at the catalytic center to achieve this catalytic rate. Previous structural studies on HAO have allowed atomic level understanding of the overall protein structure and the active site architecture (*11, 16-18*). A substrate-bound structure, albeit at a low-resolution of 3.2 Å, is available to compare to the substrate-free structure (*11*). In order to improve the quality of these structures, we have recently determined both the ligand-free structure (1.70 Å resolution) and substrate-bound structure (2.70 Å resolution) refined them to better resolutions (see Chapter 2).

3.3 Result and Discussion

3.3.1 Induced open-to-close scenario is observed in HAO upon substrate-binding

Single crystals of wild-type HAO were obtained in an anaerobic chamber. They were washed by the 3-HAA-containing cryoprotectant under strict O_2-free anaerobic conditions. This procedure generates substrate-bound HAO structures with 3-HAA bidentately chelated to the catalytic Fe ion as described previously. The superimposition of substrate-free and substrate-bound structures of wild-type HAO

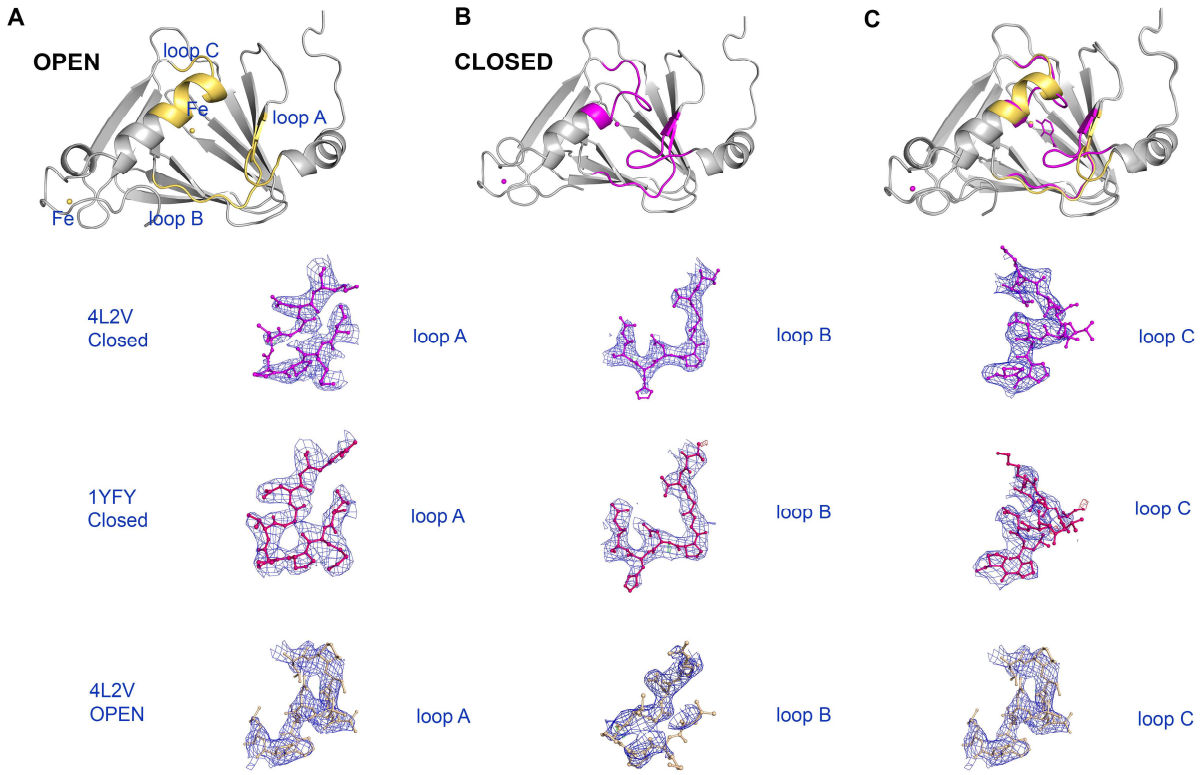

Figure 3.1. A substrate-induced loop movement around the catalytic Fe center is observed in three loop regions in HAO upon 3-HAA binding. (A) Substrate-free structure, (B) substrate-bound structure, and (C) alignment substrate-free (yellow), substrate-bond (magenta). The well-aligned components are shown in grey while the deviations are highlighted in colors. The metal iron is represented by a sphere while substrate 3-HAA is shown in sticks. The electron density map was shown on the three loop regions involved in the movement. The three loops of were fitted into the open conformation (wheat). The $2F_o$-F_c map is contoured at 1 σ; the F_o-F_c map is contoured at 3 σ (green) and -3 σ (red), respectively. The three specific loops identified are as follows: Loop A, Leu20Leu21Lys22Pro23Pro24Val25Gly26Asn27Arg28; Loop B,

shows that the enzyme exhibits two distinct conformations (Figure 3.1), which are termed open and

closed states hereafter. The substrate-bound structure is in the closed state that exhibits significant structural changes relative to the ligand-free open state on three specific loop regions surrounding the catalytic Fe center (Figure 3.1). These loop regions are as follows:

Residues 21 – 28 (loop A): Leu20Leu21Lys22Pro23Pro24Val25Gly26Asn27Arg28)

Residues 41 – 47 (loop B): Val40Val41Gly42Gly43Pro45His46Arg47)

Residues 139 – 148 (loop C): Leu139Lys140Ser141I142Val143Thr144Asp145Leu146Pro147Pro148.

Most of these residues are highly conserved across the protein sequences of HAO from various origins (Figure 3.2). These three loops shift towards to the active site iron upon 3-HAA binding. Among these three loop regions, loop A undergoes the largest movement with a shift towards the active site of ca. 8.6 Å in average for the carbon atoms when compared to the corresponding loop in the substrate-free form. When the three loops are gathered to the Fe ion, the Fe center becomes significantly more packed, resulted in an apparently a distinct active site conformation with respect to the more open conformation observed in the enzyme alone structure. Loops A and C appear to function as double-doors to the active site cavity.

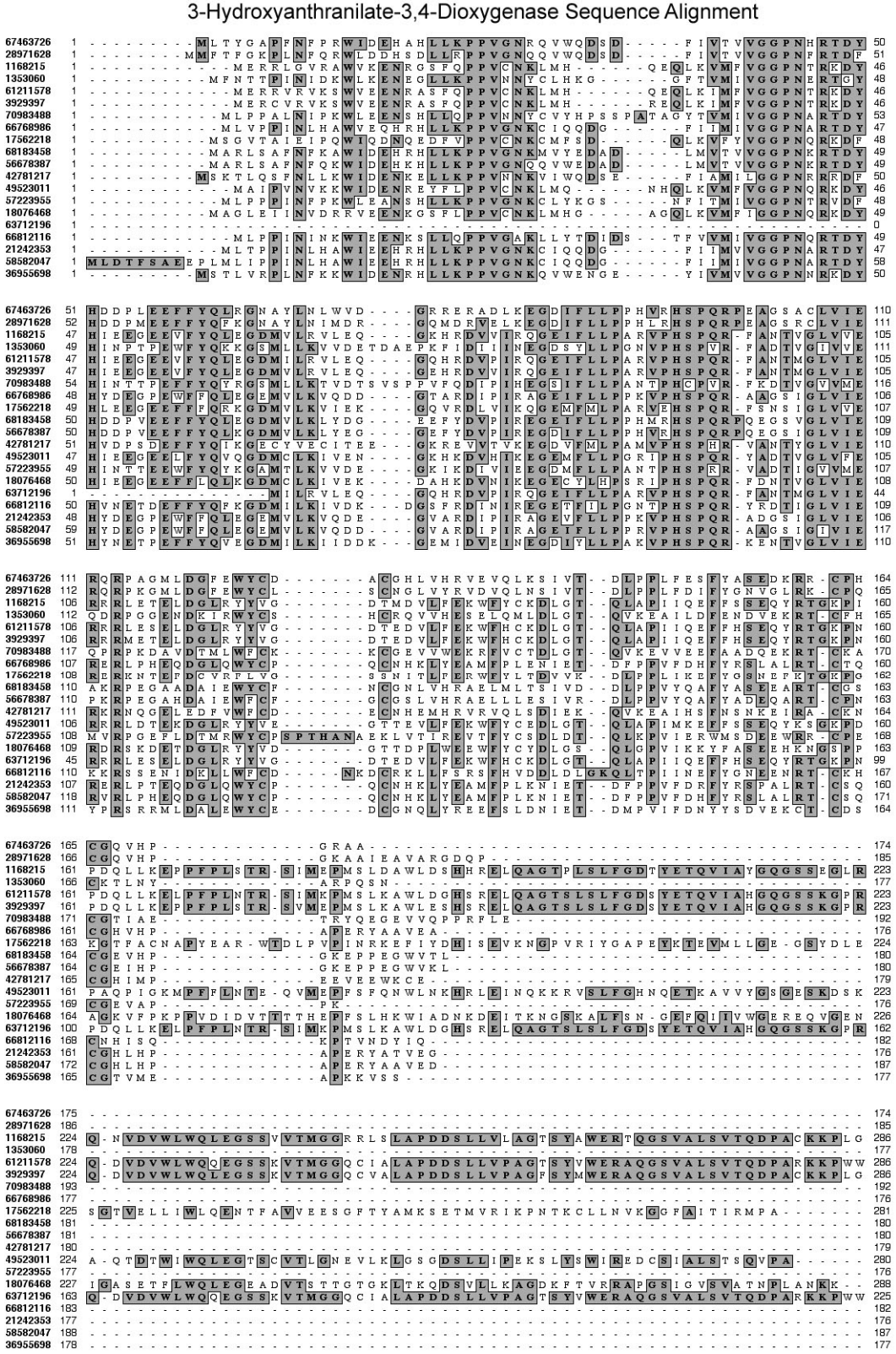

Figure 3.2 Multiple HAO sequence alignment against the protein sequence of HAO from *Cupriavidus metallidurans* (top).

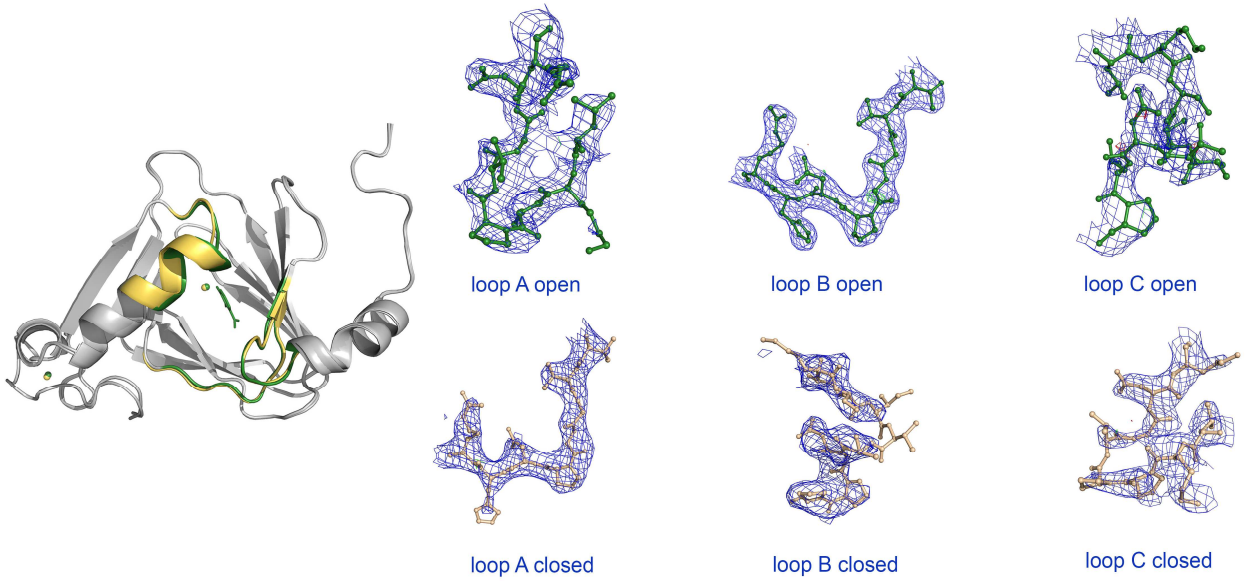

Figure 3.3 Monodentately bound 3-HAA in HAO is not able to induce the loop movement. Left, the superimposition of the substrate-free structure and 3-HAA monodentately bound HAO structure is shown. The well-aligned components are shown in grey while the deviations are highlighted in colors (substrate-free, yellow; substrate-bound, forest). The metal ion is represented by a sphere while substrate 3-HAA is shown in sticks. Right, the electron density map was shown on the three loop regions involved in the movement fitted into the open conformation (forest, top) but not the closed conformation (wheat, bottom), respectively. The $2F_o$-F_c map is contoured at 1 σ; the F_o-F_c map is contoured at 3 σ (green) and -3 σ (red), respectively.

The electron density of the residues found in the loop regions are shown in (Figure 3.3). Attempts to fit the loop residues to the open conformation led to unsatisfactory results. The electron densities do not align well on the loop residues in the open position. At a short incubation time window, we obtained the crystal structure of 3-HAA monodentately bound HAO (PDB entry 4L2P, see Chapter 2 for details). The electron density of the active site clearly shows the 3-HAA monodentately bound to the iron with the OH group at 1.7 Å while the NH_2 lies at 3.1 Å away. Surprisingly, we did not observe the loop movement as seen in the bidentate binding structure. The residues from loop A, B and C aligned well with the electron density at open conformation. If the three loops are forced to fit into the closed conformation, a lack of density at some of the residues, including xx, is clearly seen. The monodentate structure is an intermediate step prior to the final bidentate chelation. The result indicates that only the bidentate chelation of substrate is able to evoke the loop movement and close the active site.

3.3.2 The chemical nature of the Fe center in the closed state

A salient feature is that all three loops are composed of mostly hydrophobic residues. Each also contains one or two proline residues. Loop A and loop C also possess two consecutive proline residues (*i.e*., Pro23Pro24 and Pro147Pro148, respectively). Proline is a cyclic hydrophobic residue and the proline-proline dimeric fragment endows the loops with ring structure. Loop B is a highly hydrophobic fragment composed of only one proline residue (Pro45). The local hydrophobicity of the Fe center will be substantially increased due to movement of the three loops with respect to the ligand-free structure, which will facilitates the migration of molecular oxygen to the Fe center at the active site and thus maximize its catalytic efficiency.

3.3.3 Structural requirement to induce loop movement

We further sought for the driving force responsible for initiating the loop movement. After careful comparison of the structures of substrate-free, substrate monodentately bound and substrate bidentately chelated HAO, we found that the bidentate chelation of 3-HAA brings Asn27 closer to the active site through hydrogen bonding interactions with the carboxylate group of 3-HAA (Figure 3.4). Consequently, Ile142 was triggered to move closer to the iron center through ionic interactions. The original distance between Ile142 and Asn27 is 7.8 Å and it is 8.4 Å between Ile142 and Asn27 in the open state. The movement of Asn27 shortens the distance between Ile142 and Asn27 to 3.8 Å; allowing a salt bridge to form in between. This salt bridge strengthens the interactions between Asn27 and Ile142 and further induces the movement of loop C (Figure 3.4C). Furthermore, the movement of Asn27 initiates movement in loop A: Pro24, one residue on loop A, which derives hydrogen bonding interactions with Asn45 on loop B and evokes the movement of loop B. Monodentately bound 3-HAA is not able to induce the loop movement due to the long distance (6.6 Å) between the carboxyl tail of 3-HAA and the nitrogen group of Asn27. Without the proper positioning of Asn27, none of the movement in loops A, B or C can

occur. The self-adjustment of 3-HAA to a bidentate chelation mode shortens the counterpart distance by 2 Å, which results in the Asn migration to the active site. Therefore, the driving force for the loop movement is the interaction between substrate carboxyl group and Asn27 and the interaction between Asn27 and Ile142.

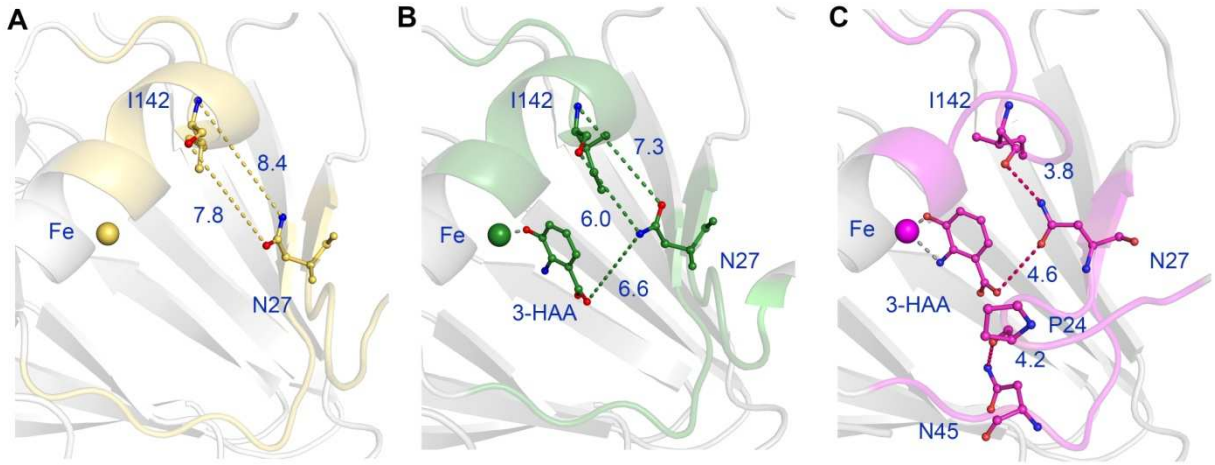

Figure 3.4 The relative positions of Asn27 and Ile142 and their interactions in the (A) substrate-free HAO, (B) 3-HAA monodentate bound HAO, and (C) 3-HAA bidentate bound HAO. The three loop regions involved in loop-movement are highlighted in color. Ile142, Asn27, Pro24, Asn45 and 3-HAA are shown in ball-and-stick mode. The distances between two-atom pairs are measured in units of Å and shown in dashed lines.

The salt bridge interaction between Ile142 and Asn27 is present in all of the HAO structures with a closed state active site, including two structures bound with the suicide inhibitor 4-Cl-3-HAA and O_2 or NO which were determined previously (*11*). Both of the structures show a closed conformation with three loops moving towards the active site iron. As expected, the interaction between the carboxyl tail of 4-Cl-3-HAA and Asn27 brings the late party into the active site. These observations further validate our conclusion that the loop movement is triggered by the 3-HAA-induced movement of Asn27 and Ile142.

3.3.4 Single mutation at Ile142 breaks down the loop movement phenomenon

The salt bridge formed between Ile142 and Asn27 upon substrate binding functions as a “clamp” and brings loops A and C towards the active site. The I142A variant has been previously constructed and

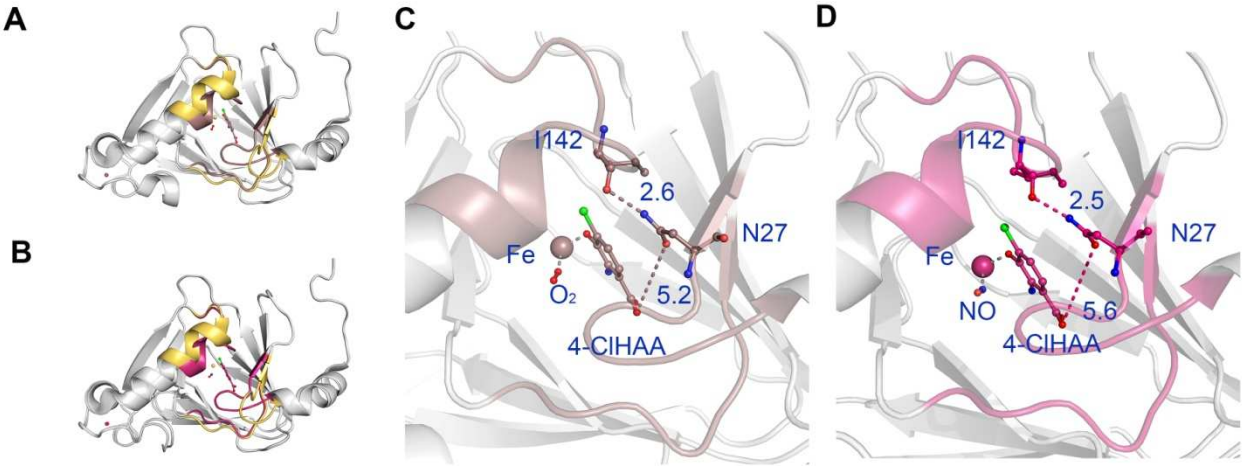

Figure 3.5 4-Cl-3-HAA bound HAO structures also turn on the closed conformation (A) superimposition of 4-Cl-3-HAA and O_2 bound HAO ternary complex and ligand-free HAO (B) superimposition of 4-Cl-3-HAA and NO bound HAO ternary complex and ligand-free HAO. The well-aligned components are shown in grey while the deviations are highlighted in colors (ligand-free, yellow; 4-Cl-3-HAA plus O_2 bound, raspberry; 4-Cl-3-HAA plus NO bound, hot pink). (C) 3-HAA bidentately bound HAO. The three loop regions involved in loop-movement are highlighted in color. Ile142, Asn27, O_2, NO and 4-Cl-3-HAA are shown in ball-and-stick mode. The distances between two-atom pairs are measured in units of Å and shown in dashed lines.

shown to be nearly catalytically inactive. Clearly, Ile142 participates in the catalytic reaction although its precise role in catalysis has not been explained. We hypothesize that it affects substrate (O_2) binding and reduces HAO catalytic efficiency. Due to the very low catalytic activity and the relative low sensitivity of the oxygen electrode, the K_m for O_2 cannot be determined. To test whether the loop movement phenomenon would still be observed with the removal of one salt bridge partner, we crystallized this variant in substrate-free and the crystal structures of I142A in complex with 3-HAA, 2-aminophenol (2-AP) and 3-aminosalicylic acid (3-ASA) and several product-bound catalytic intermediates *in crystallo*. The crystal structure of the I142A variant was determined at 1.70 Å (Figure 3.6). The comparison of the structure of I142A with the wild-type HAO structure revealed slight deviations on the residues 141 – 147, but no obvious deviations over the whole structures including the metal ligands as well as the second sphere residues as indicated by the root-mean-square deviation (RMSD) value of 0.141 from 1195 out of 1195 atoms. Thus, the observed reduction in the catalytic activity (k_{cat}) in the

mutant with substitution at Ile142 is not due to a global structural change but rather the structural alteration of loop C.

3.3.5 Structure of the I142A-3-HAA complex

To test the role of Ile142 in substrate binding, the X-ray crystal structure of the I142A-3-HAA complex was determined at 2.70 Å resolution (PDB pending). The electron density map reveals that 3-HAA binds to the active site of I142A HAO in a bidentate chelation pattern which is similarly observed in

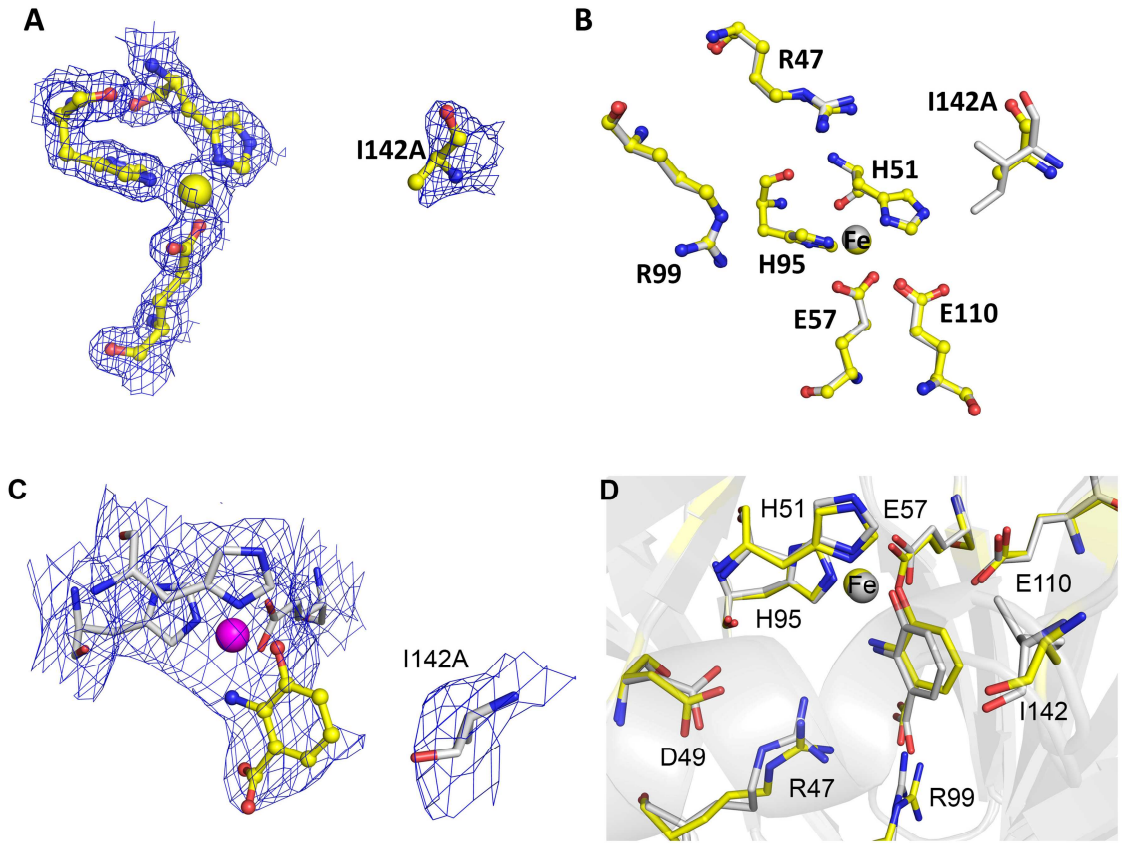

Figure 3.6 Structure details on I142A HAO. (A) Crystal structure of HAO I142A variant (PDB entry pending); (B) Comparison of the active site environments of the I142A variant and the one in wild type HAO (PDB entry 1YFY). The $2F_o$-F_c s electron density map is contoured at 1.0 σ. Atom color code: grey, carbon (wild type HAO); yellow, carbon (I142A-HAO); blue, nitrogen; red, oxygen; yellow, iron (I142A); grey, iron (wild type HAO). (C) Crystal structure of I142A HAO variant in complex with native substrate 3-HAA (PDB entry pending); (D) Comparison of the active site environments of I142A variant in complex with 3-HAA and the one in wild type HAO in complex with 3-HAA (PDB entry pending). The $2F_o$-F_c electron density map is contoured at 1.0 σ. Atom color code: grey, carbon (wild type HAO); yellow, carbon (I142A-HAO); blue, nitrogen; red, oxygen; yellow, iron (I142A HAO); grey, iron (wild type HAO).

wild-type HAO, Figure 3.3A. The superimposition of these two structures reveals several differences. Although 3-HAA binds to the active sites in I142A and wild-type HAO both in a bidentate chelation mode, substrate rotation is observed; an eight-degree dihedral angle formed by the phenol rings from the substrates in the mutant and wild-type enzymes is revealed. At the same time, the metal-coordination ligands and several second-coordination sphere residues including Asp49, Arg47 and Arg99 show deviations in orientations when compare to the counterparts in the substrate-bound wild-type structure. It is noteworthy that significant changes are observed in the previously defined mobile loop regions; 3-HAA bidentately chelates the catalytic iron in I142A and does not induce the loop movement. The loop regions can be well-aligned with the substrate-free structure (Figure 3.6). The salt bridge between Ile142 and Asn27 is not observed from these mutant structures. The interaction between Ile142 and Asn27 is presumably the key link to bring the loops together towards the catalytic iron. The alteration in the I142A variant renders this hydrogen-bonding interaction impossible, thus we do not observe the aforementioned loop movement even with the occurrence of proper substrate binding.

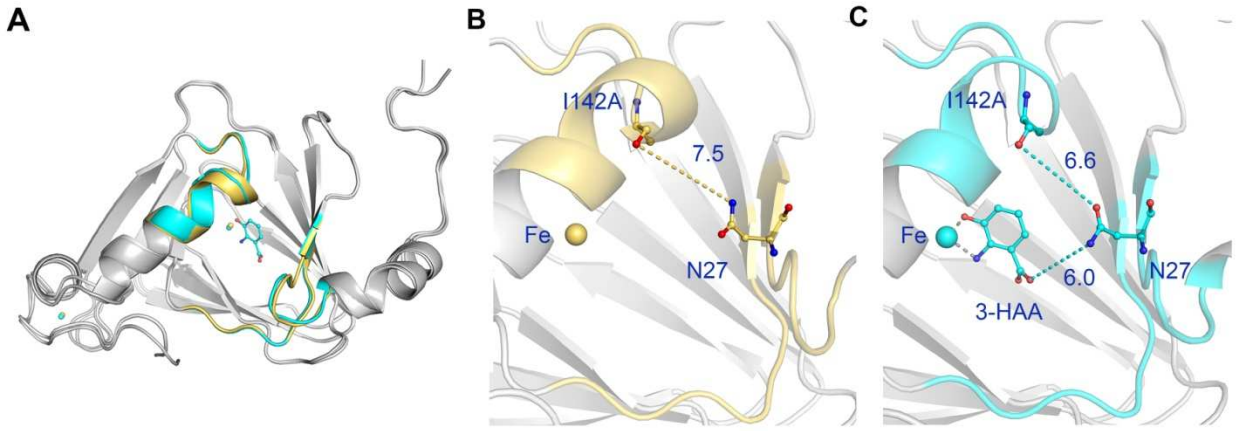

Figure 3.7 Single mutation of I142A disables the loop movement in HAO. (A) Superimposition of structures of I142A HAO and 3-HAA bidentately bound I142A HAO (B) zoom-in view of the three loop regions of I142A HAO (C) zoom-in view of the three loop regions of 3-HAA bidentately bound I142A HAO. The three loop regions involved in loop-movement are highlighted in color. Ile142, Asn27 and

3.4 Concluding Remarks

When the primary function of those Fe-dependent dioxygenase enzymes is to oxidize hydrophilic organic compounds by activating the non-polar, symmetric, hydrophobic molecular oxygen, a difficult decision has to be made: should the second ligand sphere of the Fe center be more hydrophilic or hydrophobic? In this study, we show that nature has offered an intelligent solution to solve the riddle. The Fe center is set to be more suitable for the binding of the organic substrate, and after that, a well-prepared protein dynamics follows to re-tune the active site to a much more hydrophobic environment for attracting O_2 to bind. To do this, the enzyme has to set an ordered substrate binding as found in nearly all of the Fe-dependent oxygenases. Without the organic substrate-aided tuning, the active site would not be ideal for binding of O_2. An additional benefit is that the Fe(II) ion would not tend to be oxidized by O_2 when the primary organic substrate is absent, *i.e*., preventing enzyme autooxidation.

While nature has more than one strategy to solve the low oxygen concentration problem in solution for a rapid oxygen consumption reaction at the enzyme active site, the unique feature of protein dynamics induced by substrate binding reported here may be the first structurally defined example for facilitating O_2 binding to the catalytic Fe along with the primary organic substrate in each catalytic cycle. With a rapid turnover rate, the O_2 level could drop significantly after several seconds and minutes of reaction, and the O_2 diffusion to the solution may not be faster enough and thus cause a seemingly hypoxia condition. If this occurs, the increased hydrophobicity would become more important to attract O_2 binding. Given the vast number of metal-dependent oxygen utilization enzymes, the protein dynamic-hydrophobicity strategy may be one of natural popular strategies to direct molecular oxygen towards organic substrate-bound metal centers.

4. THE RUBREDOXIN FE IS A SPARE TIRE TO THE CATALYTIC NON-HEME FE IN BACTERIAL 3-HYDROXYANTHRANILATE-3,4-DIXOYGENASE

4.1 Abstract

3-hydroxyanthranilate-3, 4-dioxygenase (HAO) catalyzes the aromaticity-breaking oxidative cleavage of 3-hydroxyanthranilate by use of a catalytic $Fe(His)_2Glu$ center, a reaction which is found critical in the kynurenine pathway of eukaryotes and the 2-nitrobenzoic acid (2-NBA) pathway of some prokaryotes. The 2-NBA pathway was recently discovered and thought to have evolved in response to human activity, and the bacteria in which it is found are able to use it as their sole source of carbon, nitrogen and energy. An interesting property of HAO from the bacterial 2-NBA pathway is a highly conserved $Fe(Cys)_4$ center which is not found in majority of the eukaryotic analogues. Here we show through EPR, Mössbauer, and fluorescent spectroscopic characterization, as well as X-ray crystallography that the buried catalytic center binds iron before the surface $(Cys)_4$ site. We also found with DALI structural search that the $Fe(Cys)_4$-containing domain in HAO resembles those of some iron-chaperon proteins. Following this finding, a doubling of enzymatic activity was observed from holo-HAO after addition of a stoichiometric quantity of apo-HAO incubation with apo-HAO, which suggests that iron bound to the $(Cys)_4$ site can be transferred to the $(His)_2Glu$ site. The results showed here uncover a new function of $Fe(Cys)_4$ center to perform as iron chaperon domain.

4.2 Introduction

The massive scale of the industrial synthesis of chemicals has generated a number of environmental challenges in recent decades. One major issue is the limited re-incorporation of synthetic organic molecules into natural biological cycles. Notably, nitroaromatic compounds are released into the biosphere almost exclusively from anthropogenic sources: agricultural and rubber chemicals, herbicides, leather, paper, and sulfur dyes (*46*). Unfortunately, they are relatively resistant to biological degradation

and recycling (*47*). 2-Nitrobenzoic acid (2-NBA) is prominent among these compounds, and it is also one of the most common precursors of numerous toxic compounds in the environment (*48*). Due to the amount of 2-NBA released into the environment in the past few decades a number of microorganisms have evolved the ability to utilize it as their sole source of carbon, nitrogen, and energy (*31*). Previous studies have shown that the bacterial degradation of 2-NBA begins with its conversion to 3-hydroxyanthranilic acid (3-HAA) (*49*). From 3-HAA, the 2-NBA pathway shares the same catabolic strategy and enzymes with the kynurenine pathway for L-tryptophan catabolism in eukaryotes (*50*).

3-Hydroxyanthranilate-3,4-dioxygenase (HAO, also known as HAD or HAAO) is the first of a series of enzymes shared by both the 2-NBA and kynurenine pathways (*31, 33, 51*). This enzyme catalyzes the critical aromaticity-breaking step of the pathways by activating dioxygen to oxidatively cleave the phenyl ring of 3-HAA, producing α-amino-β-carboxymuconate-ε-semialdehyde (ACMS) (Scheme 1) (*15*). ACMS is an unstable compound which spontaneously dehydrates and autocyclizes to produce quinolinic acid (QUIN) with a half-life time ($t_{1/2}$) of 46 min at pH 7.4 (*52*). The eukaryotic and prokaryotic HAO proteins are likely to have arisen from a common ancestral gene. Not only is the same chemical reaction catalyzed, but these proteins also share a significant degree of sequence identity (*53*).

HAO is a non-heme, iron-dependent, extradiol dioxygenase (*54*). The first crystal structure (*11*), which was determined from *Cupriavidus metallidurans* reveals that this enzyme is a homodimer belonging to the functionally diverse cupin superfamily (*3, 4*), and that the catalytic Fe is anchored by a 2-His-1-carboxylate facial triad ligand set (*55*). The crystal structures of HAO from eukaryotic origins are now available from *Saccharomyces cerevisiae* (*16*), bovine kidney, and human (*18*). An unexpected phenomenon is that prokaryotic and *Saccharomyces cerevisiae* HAO structures contain two separate iron binding domains. The first is the $(His)_2Glu$ catalytic site which is the same as the catalytic site in eukaryotes, and the other is a rubredoxin-like site coordinated by four cysteine residues on the protein

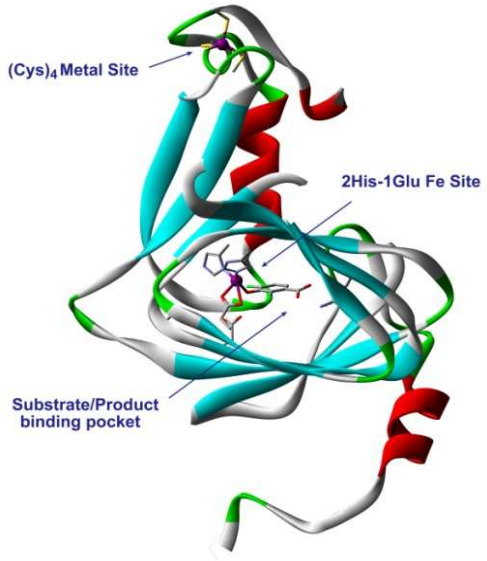

Figure 4.1 Crystal structure of HAO from *C. metallidurans* (from 1YFU.PDB). The two metal centers are represented as magenta spheres while the metal ligands are shown as sticks.

surface at the C-terminus which is not found in eukaryotes. The two iron centers are separated by 24 Å as depicted in Figure 4.1.

The rubredoxin-like iron center found in prokaryotic and *Saccharomyces cerevisiae* HAO is not involved in catalysis. Rather, it was shown in a previous study to be capable of absorbing leaking oxidative equivalents and thus preventing destructive protein damage should an uncoupling of dioxygen activation and substrate oxidation occur at the active site (*54*). This finding raises an immediate question of why the vast majority of eukaryotic HAOs do not employ a similar iron center for the same purpose. Here we propose that the $Fe(Cys)_4$ center in prokaryotic HAOs functions as an endogenous iron chaperon; it is able to store an additional iron ion which is used to replenish the catalytic center and maintain catalytic sustainability in case of iron loss from the active site caused by competition from other metalloproteins or chelation by metabolic intermediates. This role would be of paramount importance for bacteria which use 2-NBA as their sole energy and carbon source.

4.3 Materials and Methods

4.3.1 Chemicals. ^{57}Fe (95% enrichment) was obtained from Science Engineering and Education Co. (Edina, MN). 3-HAA, ammonium iron(II) sulfate (99.997%), ascorbate, EDTA, copper sulfate pentahydrate and glycerol were purchased from Sigma-Aldrich in their highest grades and used without further purification.

4.3.2 Protein preparation for the HAO catalytic activity assays.

HAO from *Cupriavidus metallidurans* was purified according to the published method (*11*). The metal-free apo form of HAO was prepared by overnight EDTA (10 mM) treatment, followed by dialysis against fresh buffer (10 mM Tris-HCl pH 7.6). The fully loaded HAO (holo-HAO) was obtained by adding 10 equiv of Fe^{2+} to the apo form of HAO and the excessive free iron ions were removed by either dialysis or desalting purification prior to use. The resulted HAO was reduced by ascorbic acid prior to enzyme activity assays.

4.3.3 Catalytic activity measurement of adding apo-HAO to holo-HAO.

Holo-HAO was premixed with apo-HAO at different ratios ranging from 0 to 2 equivalents. The catalytic activity of each sample was measured by monitoring the product formation at 360 nm. For each sample, the residual activity from apo-HAO was deducted from the observed activity to determine the effective activity for comparison. For each individual trace of a specific apo-HAO concentration, the absorbance at the starting point was subtracted over the whole time course to correct for background.

4.3.4 Reconstitution of apo-HAO for Mössbauer measurements.

Under anaerobic conditions in a glove box, we recharged the apo-HAO with $^{57}Fe^{2+}$, and/or Cu^{2+}, one equivalent at a time. This procedure generated a series of samples containing ^{57}Fe/^{57}Fe, ^{57}Fe/Cu, and Cu/^{57}Fe. The ^{57}Fe/^{57}Fe -HAO was prepared by reconstitution of apo-HAO with 2.1 equiv of Fe^{2+} ion under anaerobic conditions, followed by desalting separation using G25 column and O_2-free argon-

saturated buffer to remove unbound Fe ions. The ^{57}Fe/Cu-HAO was prepared by reconstitution of apo-HAO with 1.1 equiv of $^{57}Fe^{2+}$ ion under anaerobic conditions and followed by addition of 1 equiv of Cu^{2+}. The Cu^{57}Fe-HAO was prepared by reconstitution of apo-HAO with 1.1 equiv of Cu^{2+} ion under anaerobic conditions and followed by loading of 1 equiv of $^{57}Fe^{2+}$.

4.3.5 Mössbauer spectroscopy.

^{57}Fe-enriched HAO was obtained from apo-HAO reconstituted with $^{57}Fe^{2+}$. The final protein concentration was 0.9 mM. Mössbauer spectra were recorded on a constant acceleration instrument with an available temperature range of 1.5 to 200 K. Isomer shifts are reported relative to Fe metal at 298 K.

4.3.6 Electronic paramagnetic resonance (EPR) spectroscopy.

The Cu^{2+}-HAO EPR samples were prepared by reconstitution of apo-HAO with Cu^{2+} ion followed by desalting on a G25 column. X-band EPR spectra were obtained in perpendicular mode on a Bruker (Billerica, MA) EMX spectrometer at 100-kHz modulation frequency using a 4119HS high-sensitivity resonator. Low temperature was maintained with an ITC503S temperature controller, an ESR910 liquid helium cryostat, and a LLT650/13 liquid helium transfer tube (Oxford Instruments, Concord, MA).

4.3.7 X-ray data collection and crystallographic refinement.

HAO proteins were crystallized by optimization of conditions previously established using hanging drop vapor diffusion in VDX plates (Hampton Research). Single crystals suitable for X-ray data collection were obtained from drops assembled with 1 µL protein solution layered with 1 µL reservoir solution containing 0.1 M Tris-HCl pH 9.0, 0.2 M $MgCl_2$, 1 mM DTT and 20% PEG 8000. Crystal growth was carried out at 16 °C in a vibration-free crystal growth refrigerator (Molecular Dimensions Ltd.). The crystals were mounted in small loops of fine rayon fiber and flash-cooled directly in liquid nitrogen after being dipped into the cryoprotectant solution (0.1 M Tris-HCl, pH 9.0, 0.2 M $MgCl_2$, 22% PEG 8000 and

30% glycerol). X-ray diffraction data of Fe/Cu-HAO and Cu/Fe-HAO were collected at the SER-CAT beamline 22-ID at the Advanced Photon Source (APS), Argonne National Laboratory, Argonne, IL. All data collection was performed at 100 K. The diffraction data was indexed, integrated and scaled with (*37*). The structures were solved by molecular replacement using MOLREP program of the CCP4 suite (*56*) with the HAO structure from C. metallidurans (PDB accession number 1YFU) as search model. Electron density was fit and refined using Coot (*57*)and REFMAC5 (*58*).

4.3.8 Fluorescence spectroscopy.

The intrinsic tryptophan fluorescence of apo-HAO (40 µM) was examined at room temperature by using Cary Eclipse fluorescence spectrophotometer from Agilent Technologies. The buffer in use was 20 mM Tris-HCl at pH 7.6. The detection parameters were: excitation wavelength at 290 nm; slit width: 5 nm; emission monitoring range: 300 – 400 nm. The maxima of each of the measurements were plotted against the concentration of metal ions added and fit to equation 1:

$$\Delta F = \frac{\Delta F_{max}}{2[E]}\left((K_d + [M] + [E]) - \sqrt{(K_d + [M] + [E])^2 - 4[M][E]}\right)$$

where [M] represents the metal concentration and [E] refers to the concentration of enzyme. The fluorescence change (ΔF) is proportional to the fraction of enzyme bound with metal.

4.4 Result

4.4.1 Metal-ion reconstitution of HAO and activity assay.

Using holo-HAO loaded with two molar equivalents of Fe^{2+} per protomer as the activity benchmark, we tested the catalytic activity of HAO reconstituted with varied orders and amounts of iron and copper. Table 4.1 shows that when apo-HAO was reconstituted with one molar equivalent of Fe^{2+} per protomer, the resulting singly-loaded Fe^{2+}-HAO exhibited greater than 80% relative activity. However, when apo-HAO was reconstituted with one equivalent of Cu^{2+}, only nominal activity (*ca.* 2%) was detected. This trace activity is similar to that of the apo-HAO and is likely due either to incomplete

removal of iron during protein preparation or the presence of trace metals in the reaction solution. It appears then, that copper is unable to mediate the electron transfer between 3-HAA and O_2. Addition of copper ion, from one molar equiv up to ten equiv, to the singly loaded Fe^{2+}-HAO caused no appreciable change in its catalytic activity, suggesting that copper is unable to compete out iron from the active site. Similarly, addition of excess amount of Fe^{2+} cannot compete out Cu^{2+} from the active site. These results suggest that the enzyme active site appears to have a higher metal-binding affinity than the surface $(Cys)_4$ site, so the first metal ion presented binds to the $(His)_2Glu$ site rather than the $(Cys)_4$ site.

Table 4.1 Catalytic activity of metal-reconstituted HAO

Divalent metal ions	$2Fe^{2+}$	Apo	$1Fe^{2+}$	$1Fe^{2+}$ + $1Cu^{2+}$	$1Fe^{2+}$ + $10Cu^{2+}$	$2Cu^{2+}$	$1Cu^{2+}$ + $1Fe^{2+}$	$1Cu^{2+}$+ $2Fe^{2+}$	$1Cu^{2+}$ + $5Fe^{2+}$	$1Cu^{2+}$ + $10Fe^{2+}$
Relative activity (%)*	100	2 ± 0.3	84 ± 0.2	86 ± 4.0	84 ± 16.2	2 ± 0.7	15 ± 0.8	17 ± 0.9	19 ± 0.1	12 ± 1.2

*Activity assay was performed after removing excessive metal ions following the reconstitution reaction according to the procedure described in the Materials and Methods.

4.4.2 Spectroscopic characterization of the reconstituted HAO

Due to spin coupling between free Cu^{2+} ions in solution, the EPR signal intensity of the aqueous Cu^{2+} is quite low. Binding to protein ligands, however, increases the EPR signal intensity so that it is proportional to the amount of the chelated copper ions. Chelation also alters the EPR signal lineshape, which is sensitive to the ligand set and protein environment. Reconstitution of apo-HAO with a stoichiometric amount of Cu^{2+} gave rise to an EPR signal indicative of a type II Cu^{2+} center coordinated by a mixture of N/O ligands (Figure 4.2). Spin quantitation against a sample of Cu-EDTA recorded under the same conditions suggested *ca.* 0.8 molar equivalent of Cu^{2+} per protomer. Addition of Fe^{2+} ion to the copper-reconstituted HAO did not reduce the intensity of the EPR signal, as expected based on the data presented in Table 1. The Cu^{2+} EPR signal was nearly absent from the samples in which Cu^{2+} was added

to the singly loaded Fe^{2+} ion, also consistent with the activity assays. Moreover, this result suggests that

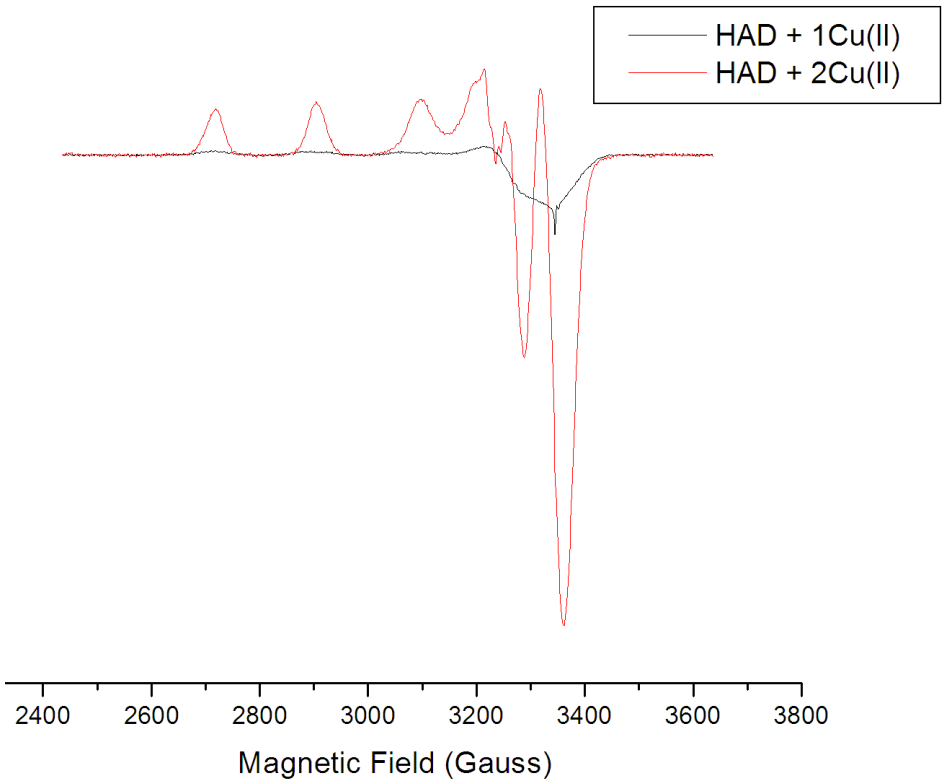

Figure 4.2 X-band EPR spectrum of Cu-reconstituted HAO measured at 20 K with 0.02 mW microwave power.

Cu^{2+} is unable to bind to the $(Cys)_4$ site.

4.4.3 Mössbauer spectroscopy

Mössbauer spectroscopy was utilized to characterize the Fe^{2+} ions of the various reconstituted proteins. Under anaerobic conditions, apo-HAO was reconstituted with $^{57}Fe^{2+}$ and/or Cu^{2+}, one equivalent at a time. This procedure generated a series of samples which contained $^{57}Fe/^{57}Fe$, $^{57}Fe/Cu$, and $Cu/^{57}Fe$ reconstituted in the specified orders, respectively. The Mössbauer spectrum of the $^{57}Fe/^{57}Fe$-reconstituted HAO sample taken at 77 K, shown in Figure 4.3A, consists of two distinct sets of quadrupole doublets with roughly equal signal intensities. Spectral simulation shows that one quadrupole doublet displays an isomer shift (δ) value of 1.37 mm/s and quadrupole splitting (ΔE_Q) value

of 2.95 mm/s. These values are consistent with N/O mixed ligation for a high-spin (S = 2) Fe^{2+} center and are comparable to the values reported for the protocatechuate 4,5-dioxygenase (*59*). This quadrupole doublet is therefore assigned to the $Fe(His)_2Glu$ center. The second quadrupole doublet shows a δ value of 0.52 and a ΔE_Q value of 0.57, which is characteristic of a ferrous rubredoxin-like $Fe(Cys)_4$ center at the S = 2 state (*60-62*). Thus, it is assigned to the $Fe(Cys)_4$ center.

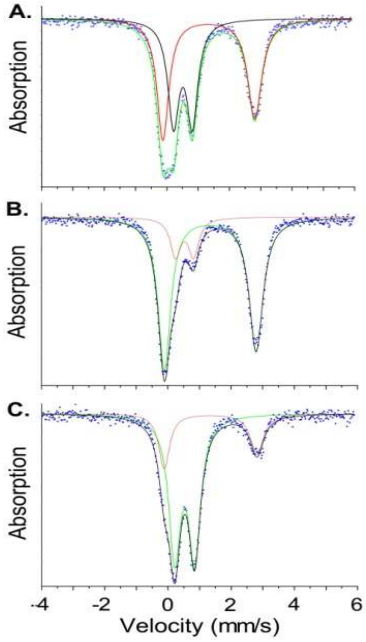

Figure 4.3 Mössbauer spectra of HAO reconstituted with (A) 2Fe (B) 1Cu + 1Fe (C) 1Fe + 1Cu (data: black; simulation of doublet 1: red; simulation of doublet 2: green.

Figure 4.3B shows the Mössbauer spectrum of Cu/Fe-reconstituted HAO. Both of the quadrupole doublets seen in the $^{57}Fe/^{57}Fe$-reconstituted HAO sample are present though not at equal intensities. Most of the ^{57}Fe signal arises from the ruberdoxin-like $Fe(Cys)_4$ center, while the catalytic $Fe(His)_2Glu$ center only accounts for 18% of the total iron. Conversely, when iron is loaded before copper (^{57}Fe/Cu-reconstituted HAO), the majority of the ^{57}Fe signal is seen from the catalytic center (75%) (Figure 4.3C). These data further support the notion that the catalytic center has priority for metal ion binding. The observation that the order of metal loading is able to significantly alter the distribution of the metals between the two metal-binding sites but that neither metal is able to completely occupy either site suggests that the metal binding affinity of the two sites are similar though differentiable.

4.4.4 Metal binding affinity measured by tryptophan intrinsic fluorescence study.

The intrinsic tryptophan fluorescence of HAO allows for the use of fluorescence spectroscopy to monitor the binding of metal ions to the enzyme. The tryptophan fluorescence signal of apo-HAO is quenched upon addition of either Fe^{2+} or Cu^{2+} (Figure 4.4). Notably, copper and iron show different quenching behavior on the fluorescence signal. Titration of Fe^{2+} to apo-HAO causes the fluorescent signal to red-shift by 23 nm from 335 nm, and the intensity to decrease to ~15% of its initial value. These effects are seen to saturate at 2 – 2.5 equivalents of Fe^{2+}. In contrast, when Cu^{2+} was used, the fluorescence signal red-shifts by 5 nm from 335 nm concomitant with a reduction in intensity to ~ 60% of its initial value. Also distinct from iron, the effects caused by copper saturates at about 1 equivalent, rather than 2. These results indicate that apo-HAO can bind two Fe^{2+} but only one Cu^{2+}. Furthermore, the K_d values of iron were determined to be 5 and 12 µM for the catalytic and rebrudoxin sites, respectively.

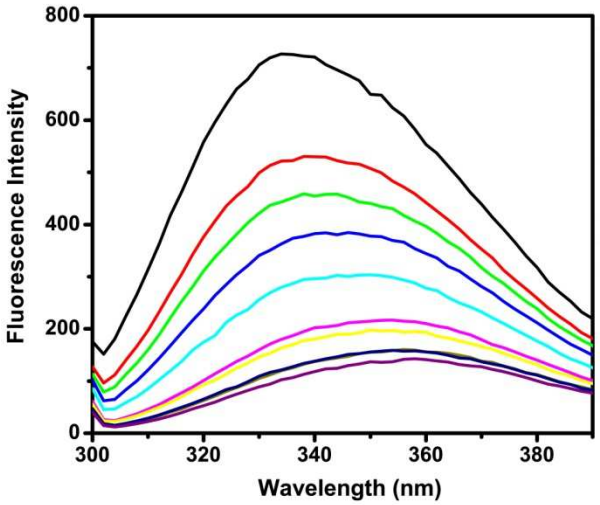

Figure 4.4 Intrinsic fluorescence spectrum of apo-HAO (black trace) quenched by titration of Fe^{2+} ion at 0.25 molar equivalent of increments

4.4.5 Crystal structures of Cu/Fe-HAO and Fe/Cu-HAO

We obtained single crystals of Cu/Fe- and Fe/Cu-reconstituted HAO proteins and determined their structures by X-ray crystallography (Figure 4.5). These crystals belong to the $P6_522$ space group.

One protomer has been observed in each asymmetric unit, however each protomer forms a dimer with a neighboring protomer in an adjacent asymmetric unit as previously observed (*11*). Size-exclusion chromatography shows that HAO is eluted as a dimer of 38 kDa, which supports that the native quaternary structure of HAO is dimeric. The Cu/Fe-HAO crystal structure was determined at 1.75 Å (Figure 4.5B), which allows for detailed comparisons of the metal centers between this structure and the previously-solved holo-HAO (*i.e.*, Fe/Fe-HAO) structure from the same species (Figure 4.5A) (*54*). The overall structures of Cu/Fe-HAO and Fe/Fe-HAO are nearly identical. The Cu/Fe-HAO clearly contains

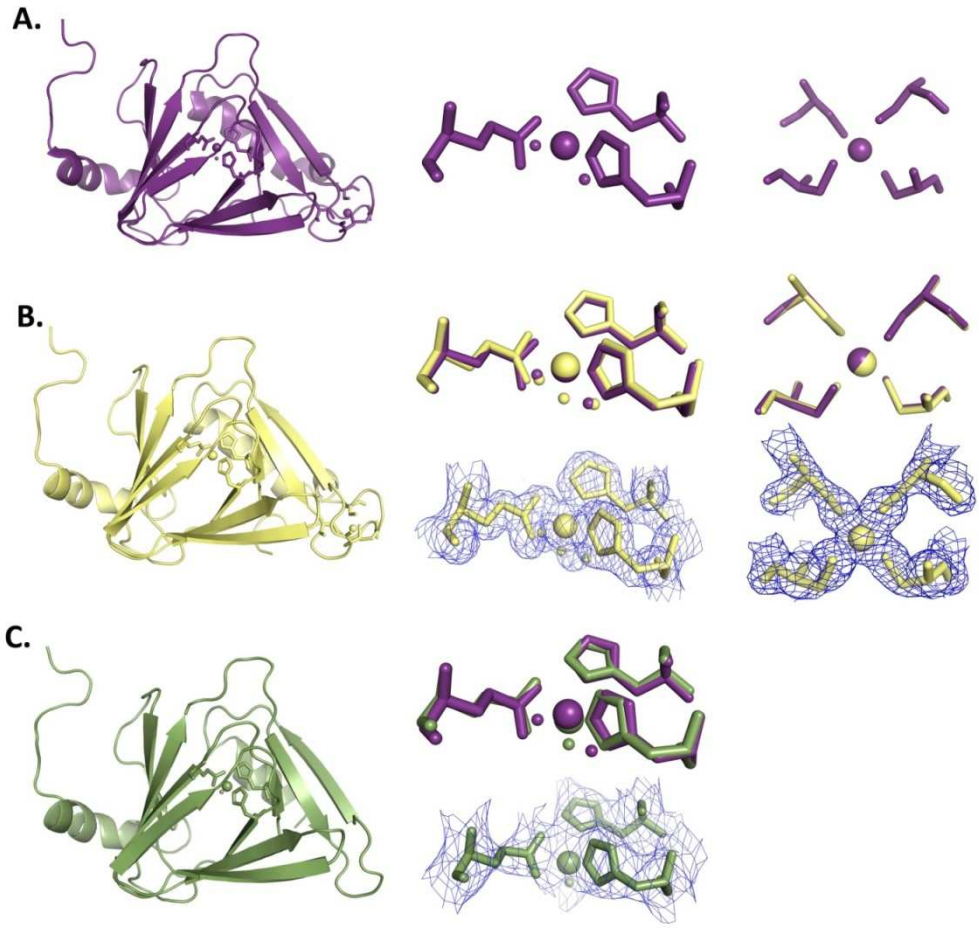

Figure 4.5 The metal sites in HAO reconstituted with different metals. (A) Ribbon diagram of holo-HAD with zoom-in view on the active site and the $Fe(Cys)_4$ site (purple, PDB entry 1YFU); (B) Ribbon diagram of Cu/Fe-HAO with zoom-in view on the active site and the $Fe(Cys)_4$ site (yellow, PDB entry 4HVO); (C) Ribbon diagram of Fe/Cu-HAO with zoom-in view on the active site (green, PDB entry 4HVQ);The metal ions are represented in larger spheres while water molecules are shown in smaller scale spheres with respective colors. $2F_o–F_c$ electron density map is countered to 1σ. This figure was produced using PyMol.

two metal centers. In the catalytic center, the metal ion is coordinated by His51 and His95 with the bond distances of 2.0 and 1.9 Å, respectively. The bidentate ligand Glu57 in the Fe/Fe-HAO structure is no longer a metal ligand in the Cu/Fe-HAO structure, although it is still close to the copper ion with $O_{\epsilon 1}$ and $O_{\epsilon 2}$ at 3.1 and 3.2 Å, respectively. This metal ion is assigned to copper based on the coordination difference to the Fe/Fe-HAO structure and is consistent with the activity assays and spectroscopic characterizations. Furthermore, three water ligands, at distances of 2.3, 2.8, and 2.9 Å to the active-site metal center, respectively, are observed in Cu/Fe-HAO rather than two at 2.8 and 2.8 Å as is seen in Fe/Fe-HAO. The other metal center shows identical structure to what was reported for the $Fe(Cys)_4$ center in the Fe/Fe-HAO structure.

The Fe/Cu-reconstituted HAO proved difficult to crystallize, and the crystals obtained were very fragile and tended to break when immersed into the cryoprotectant. The best structure obtained was only able to be refined to 2.80 Å resolution (Figure 4.5C). The metal coordination at the catalytic center closely resembles that of Fe/Fe-HAO. The bond distances are 2.0, 2.2, 2.8, and 2.4 Å for N_{δ} of His51, N_{ϵ} of His95, and the two oxygen atoms in the carboxyl moiety of Glu57, respectively. It is noteworthy that the structure of Fe/Cu-HAO lacks the surface metal center at the rubredoxin site. Moreover, comparison of this region with that of Fe/Fe-HAO reveals that the electron density of amino acids 154-174 (11.5% of

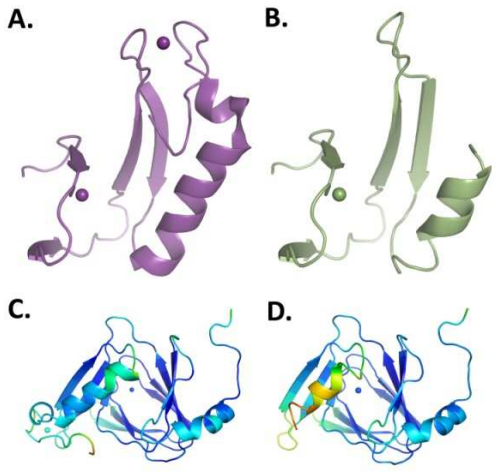

Figure 4.6 Stability of FeCu- and CuFe-HAO. (A) Structure of the 89 – 174 residues in holo-HAD; (B) Structure of the 89 – 154 residues in FeCu-HAD. The collapse containing residue 155 – 174 observed in comparsion of holo- and FeCu-HAD. The B-factor plots of CuFe-HAO and FeCu-HAO are shown in (C) and (D), respectively.

the total sequence) is missing, presumably due to increased conformational flexibility (Figure 4.6A and 4.6B). Figure 4.6C and 4.6D present the structures of Cu/Fe-HAO and Fe/Cu-HAO by their respective B-factors. The result shows a conformation flexibility at the $(Cys)_4$ site when the iron ion is absent. Notably, the disorder at the rebredoxin-like site has no observable effect on the N-terminal domain where the catalytic iron center is located. Therefore the conformation flexibility at the second Fe site should have no observable impact to catalysis. These results are consistent with the above mentioned spectroscopic conclusions that the first metal introduced to apo-HAO binds to the active site, and further reveal that the $(Cys)_4$ site is selective for iron rather than copper.

4.4.6 The $Fe(Cys)_4$ is capable of delivering its Fe ion to apo-HAO

The DALI search (30) carried out in a previous study showed that fourteen cupin proteins structurally resemble HAO (14). Although the overall structures display similarities to HAO, none of the identified proteins possess an $Fe(Cys)_4$ site. Therefore, we performed a structural search of partial prokaryotic HAO structures with special attention to the rubredoxin-like domain that contains the $Fe(Cys)_4$ center. The protein most structurally similar to the rubredoxin-like domain of HAO found from a DALI search is Kti11P (PDB entry 1YOP). Kti11P is a known iron chaperon protein with an $Fe(Cys)_4$

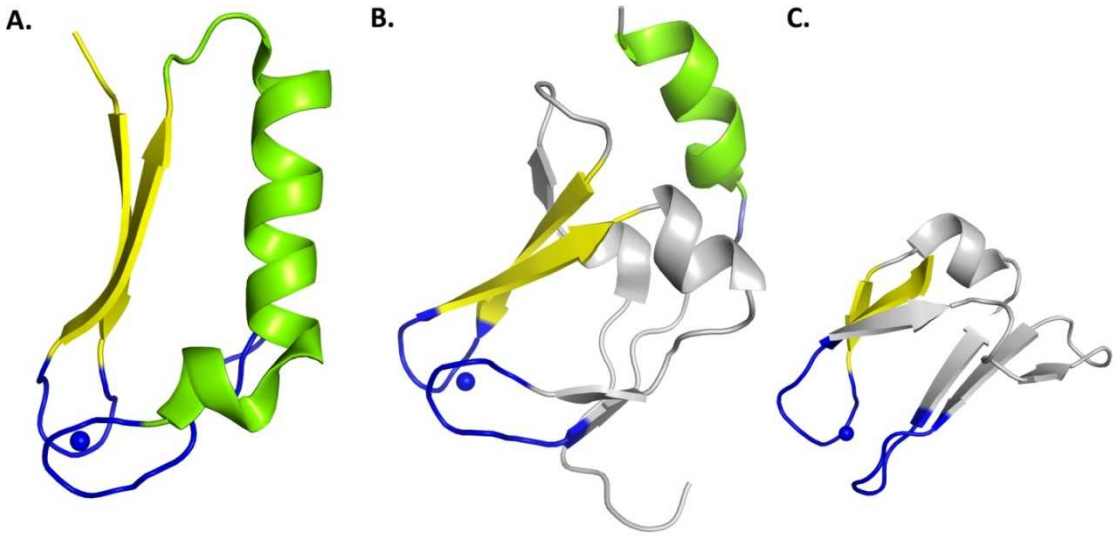

Figure 4.7 Comparison of structures of Kti11p (left) and holo-HAD (right). The spheres represent the metal ions.

center. The structures of the rubredoxin-like domain of both Kti11P and HAO contain a β-sandwich as well as an α-helix (Figure 4.7). Notably, the $Fe(Cys)_4$ is observed in prokaryotic HAO while $Zn(Cys)_4$ is shown in Kti11P. Unfortunately, zinc-reconstitution caused protein denaturation in HAO. Earlier studies suggested that Kti11P is a zinc-finger-like protein with multiple functions, including chaperoning iron and assisting the translocation of a membrane protein (31, 32). However, more recent studies revealed that Kti11P and many of the proteins possessing the zinc-finger-like structures have higher affinity to Fe ions and their primary role is to shuttle iron (33). Another example which has the aforementioned feature is Dph4, whose role as Fe-chaperon has recently been demonstrated (33). The similarity of the second metal binding site of HAO to these Fe chaperon proteins suggest that the $Fe(Cys)_4$ center of HAO may serve as an endogenous Fe-chaperon.

In order to test this hypothesis, we premixed apo-HAO and holo-HAO at different ratios with the final concentration of holo-HAO kept constant and measured the activity of the enzyme mixtures after incubation. Figure 4.8 shows that the presence of apo-HAO increased the specific activity compared to the control experiment which contained only holo-HAO. The increase in specific activity was dependent on apo-HAO concentration, and the activity reached a plateau at double the activity of holo-HAO up addition of ~4 equivalents of apo-HAO. These results suggest that the iron at the $Fe(Cys)_4$ cite of holo-

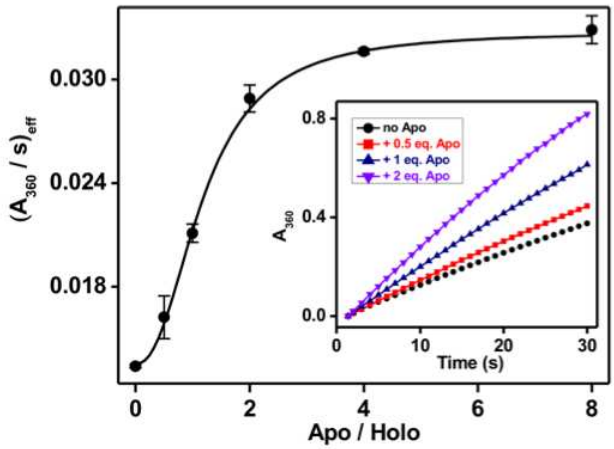

Figure 4.8 Addition of apo-HAO to holo-HAO can increase the catalytic activity. The inset shows representative kinetic traces.

HAO can be transferred to the active site of apo-HAO, increasing the population of catalytically active protein molecules. Myoglobin and tryptophan, 2-3-dioxygenase, which each contain a type-*b* heme, were used in place of holo-HAO as negative controls. Neither heme protein was able to transfer its iron ion to apo-HAO.

4.4 Discussion

Rubredoxin-like $Fe(Cys)_4$ centers are prevalent in nature. The primary role of this metal center is typically to mediate electron transfer (*63-66*), although there are isolated reports which found alternative functions such as catalysis (*67*), and oxidative stress protection (*68*). In this work, a new function for this canonical iron center as endogenous iron-chaperon is suggested.

The salient feature of HAO from *Saccharomyces cerevisiae* and prokaryotic sources is the presence of an $Fe(Cys)_4$ center not found in eukaryotic enzymes. The $Fe(His)_2Glu$ center is the catalytic center and is fully competent for activating dioxygen and mediating electron transfer from the substrate to dioxygen. The observation of a second iron site which is not involved in catalysis is then quite intriguing. Our combined kinetic assays, crystallographic studies, and EPR and Mössbauer spectroscopic characterizations show that (1) the active site has a higher binding affinity than the rubredoxin-like site for metal ions, (2) the structure and properties of the catalytic center are independent of the rubredoxin-like site, and (3) the $(Cys)_4$ center binds Fe but not copper, and the Fe ion bound there can function as a spare tire to ensure the availability of iron to the catalytic center in addition to playing a structural role in stabilizing the rubredoxin-like domain. The K_d values determined from intrinsic fluorescence further help to elucidate the feasibility of iron transfer between the two metal binding sites. A similar metal competing and conservation mechanism may exist in other proteins which play vital roles in essential metabolic pathways.

Prior to this work, it was not known why bacterial HAOs possess a second iron binding site similar to the metal centers of rubredoxin and several zinc-finger proteins which contain rubredoxin-like knuckles. Previous studies have shown that zinc ions inhibit the catalytic activity of HAO and suggests that the $(Cys)_4$ site is not designed for zinc binding in vivo (*53, 69*). The rubredoxin-type $Fe(Cys)_4$ mononuclear iron center is the simplest iron-sulfur center with tetrahedral coordination of the iron ion. Cys residues form common loop structure known as a ‘‘knuckle’’ (Cys-X-X-Cys-X-X) (36). Any mutation on the $Fe(Cys)_4$ center of HAO in previous (*54*) and current studies results in insoluble proteins. Several representative proteins like Dph4 and HscB in the J-protein family, as well as frataxin, contain the aforementioned structural features (33, 37). These proteins have previously been identified as putative iron donors in mitochontrial iron-sulfur cluster assembly. Iron is stored in the $Fe(Cys)_4$ cluster of these proteins and delivered to their partner proteins during the biosynthesis of the iron-sulfur clusters. The structural similarity of the $Fe(Cys)_4$ center of HAO to the iron donor proteins and its slightly lower affinity for iron binding compared to the active site metal center led us to propose a new role for it. The biochemical and structural results collectively point the reburedoxin-like iron center as an iron storage and chaperone role to ensure the catalytic site is loaded, *i.e*., it serves as an endogenous iron chaperon to provide iron to the active site if the active site iron ion is lost.

This spare Fe center may become important in bacteria living on nitrobenzoic acid as their sole source of carbon, nitrogen, and energy. The non-heme Fe ion at the active site is easily lost during protein purification, and this may occur in cells because many of the metabolic intermediates in the 2-NBA degradation pathway are capable of chelating metal ions. For bacteria which use 2-NBA as their sole carbon/nitrogen/energy source, HAO is a critical enzyme which must always be active. In contrast, the iron storage strategy does not necessarily exist in eukaryotic HAO, because the kynurenine pathway is not as vital for survival of the organism.

5. PIRIN IS An IRON-DEPENDENT REDOX REGULATOR OF NF-κB

5.1 Abstract

Pirin is a nuclear non-heme Fe protein of unknown function present in all human tissues. Here we describe that pirin may act as a redox sensor for the NF-κB transcription factor, a critical mediator of intracellular signaling that has been linked to cellular responses to pro-inflammatory signals and which controls the expression of a vast array of genes involved in immune and stress responses. Pirin's regulatory effect was tested with several metals and at different oxidations states, and our spectroscopic results show that only the ferric form of pirin substantially facilities binding of NF-κB proteins to target κB genes, a finding which suggests that pirin performs a redox sensing role in NF-κB regulation. The molecular mechanism of such a metal identity- and redox state-dependent regulation is revealed by our structural studies of pirin. The ferrous and ferric pirin proteins differ only by one electron, yet they have distinct conformations. The Fe center is shown to play an allosteric role on an *R*-shaped surface area that has two distinct conformations based on the identity and the formal redox state of the metal. We show that the *R*-shaped area comprises the interface for pirin-NF-κB binding which is responsible for modulation of NF-κB's DNA binding properties. The non-heme Fe protein pirin is proposed to serve as a reversible functional switch that enables NF-κB to respond to changes in the redox levels of the cell nucleus.

5.2 Introduction

The transcription factor, nuclear factor κB (NF-κB), discovered in 1986 (*70, 71*), is a ubiquitous cellular regulator widely recognized as a critical mediator of intracellular signaling for immune/inflammatory response including oxidative stress (*72-74*). NF-κB is a family of structurally related and functionally conserved dimeric proteins which consist of RelA (p65), RelB, c-Rel, p50, and p52. All members can form both homo and heterodimers with different physiological functions and gene

targets (*75-77*). NF-κB proteins bind and activate several hundred κB genes in response to activating stimuli (*78-80*). The activity of NF-κB is tightly controlled by regulatory proteins and cofactors collectively known as co-regulators (*81, 82*). Complex regulatory networks exist to ensure that NF-κB is only activated by appropriate stimuli and is then inactivated when no longer needed (*83-85*). NF-κB typically resides in the cytoplasm in an apparently inhibited state bound with an inhibitory protein known as IκBα. Previous studies have established that NF-κB activation is first achieved by phosphorylation of the inhibitory protein IκBα to liberate NF-κB to their free forms. Next, NF-κB proteins are translocated to the nucleus where, with the help of co-regulators, they will orchestrate the cascade of signaling responses to the external stimuli. At present, the precise roles played by the co-regulators in the cell nucleus are poorly understood.

Winnacker and coworkers in 1997 identified a highly conserved human protein by using nuclear factor I as a "bait protein" and named it pirin (*86*). This previously unknown protein is expressed in all human tissues. Biochemical data suggests that pirin is a nuclear protein comprised of 290 amino acids, ca. 32 kDa (*86*). Experiments using genomic Southern and Western blots have demonstrated the presence of pirin genes and their expression in dot-like sub-nuclear structures that represent loci of specific nuclear processes including DNA replication and/or RNA polymerase II transcription (*86*). Pirin has been found to form tight complexes with the inducible anti-apoptotic transcription factor NF-κB p50 homodimer and the proto-oncoprotein Bcl-3 (*87*). In a gel mobility shift assay using cell lysates, pirin was shown to enhance the DNA binding activity of the p50-Bcl-3 complex (*87*). These observations led to the initial suggestion that pirin functions as a co-regulator in the NF-κB transcription complex (*87*). However, such a proposed regulation has not been confirmed and the mechanism of which is completely unknown.

In the subsequent studies by various laboratories, pirin is found to be a non-heme iron-binding protein that belongs to an ancient redox-sensitive subclass of proteins in the cupin superfamily (*12, 88,*

89). Pirin has additionally been linked experimentally to the metastasis of melanoma cells (*90, 91*). A knockdown experiment in melanoma cells has confirmed that pirin interacts with Bcl-3 and is associated with cell migration (*91*). It has been shown that pirin expression is significantly up-regulated in the spleen and kidney of cytosolic superoxide dismutase (SOD)-deficient mice (*92*). Similarly, up-regulation of pirin expression by chronic cigarette smoking has been associated with bronchial epithelial cell apoptosis (*93*). The crystal structure of pirin at 2.1 Å resolution reveals a ferrous site that is octahedrally coordinated with three histidines, one glutamate, and two water molecules (*12*). In the present work, we describe that pirin substantially facilitates the DNA binding of NF-κB p65 to the IgκB gene when the metal center is a ferric ion. An unprecedented redox regulation mechanism is proposed from the previous studies and the results described below.

5.3 Materials and Methods

5.3.1 Protein materials

The full-length (1 - 290 amino acids) untagged form of human Pirin was cloned and expressed in *Escherichia coli* strain BL21(DE3) (Invitrogen). Cells were grown at 37°C in LB media with 50 μg/ml kanamycin until an OD600 around 0.6 - 0.8 was achieved. Protein expression was induced by 0.4 mM isopropyl-β-D-thiogalactopyranoside. Cells were further grown for 16 hours at 28°C before harvesting by centrifugation at 8000 × g for 15 min. The cells were re-suspended in the lysis buffer (15 ml per gram cell pellet), which consisted of 20 mM HEPES (pH 7.5), 150 mM NaCl, 2 mM EDTA, 0.2 mM phenylmethylsulfonyl fluoride and 10 mM β-mercaptoethanol, 5% glycerol. The cell membrane was broken by an automated cell disruptor made by Microfluidics (M-110P) to release proteins. The purification of pirin protein consisted ammonium sulfate fractionation and three major chromatographic steps including SP Sepharose, Superdex 75, and MonoS on an ÅKTA FPLC system (GE Healthcare). The metal-free apo-protein of pirn was isolated from iron-depleted minimum medium and metal reconstitution details are given in the on-line methods. The His_6-tagged truncated versions of human

p65 (19-291) was used in the previous studies (*94, 95*) by Dr. Gourisankar Ghosh of University of California San Diego and the plasmid was obtained from Dr. Jim Maher, III of Mayo Clinic College of Medicine. The metal-free protein was isolated from an iron-depleted minimal medium (*96*). The purified protein was treated with 10 equivalents of EDTA overnight and then desalted with 20 mM Tris-HCl buffer (pH 7.4) containing 50 mM NaCl and 5% glycerol.

5.3.2 Metal analysis

Metal contents of each pirin sample were determined by inductively coupled plasma optical emission spectrometry using a Spectro Genesis spectrometer (Spectro Analytical Instruments GmbH & Co. KG, Germany). Calibration curves were obtained by measuring the standards at the concentrations of each element at 0, 0.1, 0.3, 0.5, 1.0 and 10 ppm (mg/L).

5.3.3 Nuclear extract containing native NF-κB proteins

Nuclear extract of HeLa cells was prepared by using Subcellular Protein Fractionation Kit for Cultured Cells from Pierce Protein Research Products (Thermo Fisher Scientific) according to the manufacturer's protocols. Prior to injection, the extract was diluted to 0.08 μg/mL by the SPR binding buffer described above. The binding measurements were taken with the extract alone and together with added pirin (10 μM) protein.

5.3.4 DNA

The κB-site DNA used was synthetic oligonucleotide 5'-biotin-GAGTTGAG**GGGACTTTCC**CAGGC-3' (κB site is shown in bold). The single strand DNA was annealed to its complementary strand before use. A non-specific DNA sequence of 5'-CCTATATGCGGCGTATATCC-3' (a generous gift from Dr. W. David Wilson) was used as a negative control

5.3.5 Spectroscopy

SPR measurements were carried out on a Biacore T200 instrument (GE Healthcare). Biotinylated double-stranded IgκB DNA was immobilized to streptavidin-coated sensor chips using standard procedures. The protein-DNA binding was carried out at 20 °C in 20 mM Tris-HCl, (pH 7.4), containing 50 mM NaCl and 0.005% surfactant P20 at a 50 µl/min flow rate. The effect of pirin upon NF-κB binding the IgκB sequence was studied by flowing the protein over the sensor chip and comparing the levels of DNA binding in the absence and presence of the putative co-regulator protein. The final concentration of p65 was 50 nM in the SPR injection buffer while pirin concentration was varied from 0 - 25 µM. After injecting protein samples for 420 seconds, buffer was injected from 420 - 1220 s to rinse the weakly bound proteins from the chip surface in order to monitor the dissociation of the protein or protein complexes. Vitamin C was injected at 980 s in the reversibility testing experiments. The sensor chip surface was regenerated with 0.1% SDS and 3 mM EDTA between each measurement. The anaerobic SPR experiments were performed using O_2-free, argon-saturated buffer.

QCM-D measurements were performed on an E4 instrument (Q-Sense, Sweden) with biotin-functionalized sensors. Streptavidin was flowed over the biotinylated surface, followed by biotin-labeled IgκB-site DNA for immobilization. The equilibrium buffer was 20 mM Tris-HCl (pH 7.4) containing 50 mM NaCl. In each measurement, a total volume of 500 µl was continuously injected at a flow rate of 150 µl/min followed by buffer injection for an additional 300 seconds. The net change in frequency and dissipation was calculated by subtracting the values recorded at the sample injection time from those recorded at the end of each rinsing step. This eliminated the influence of nonspecific, loosely bound proteins on the DNA-immobilized surface. The surface was regenerated between each sample injection by flowing through 0.05% SDS followed by the equilibrium buffer until the baseline was restored. The concentration of p65 was maintained at 0.5 µM, while pirin concentration varied from 0, 0.5, 1.5, 2.5 and 5 µM for each run of the sample application.

Fluorescence spectroscopy was performed on a Cary Eclipse fluorescence spectrophotometer from Agilent technologies Inc., CA. Purified p65 was titrated into the fluorescence cuvette containing FAM-labeled double-stranded DNA with IgκB sequence in the presence or absence of Fe(III)-pirin, or pirin reconstituted with other metal ions in 20 mM Tris-HCl buffer (pH 7.4) and 50 mM NaCl.

The midpoint redox potential of pirin was determined by using a single-wall carbon nanotube-modified electrode in a spectroelectrochemical cell hosted in a N_2-filled, O_2-free plastic bag. Pirin (500 μM) in 50 mM Tris-HCl (pH 7.4) was used in this study. The formal potential was obtained from the recorded cyclic voltammetry curves.

X-band EPR spectra were obtained in perpendicular mode on a Bruker E200 spectrometer at 100-kHz modulation frequency using a high sensitivity resonator ER4119HS at 10 K maintained by an ESR910 liquid helium cryostat and an Oxford ITC503S temperature controller). Measurements were conducted by maintaining the frequency of the electromagnetic radiation constant while the magnetic field was swept. Pirin (160 μL/sample, 200 – 450 μM) was prepared in a quartz EPR tube with 20 mM Tris-HCl buffer (pH 7.4) containing 50 mM NaCl.

5.3.6 Crystallizations and X-ray structure determinations

Pirin was crystallized through optimization of the conditions previously established(*12*) by hanging drop vapor diffusion in VDX plates (Hampton Research). Single crystals suitable for X-ray data collection were obtained from drops assembled with 1 μL protein solution layered with 1 μL reservoir solution containing 0.1 M MOPS pH (6.5), 15% PEG 20000. Crystal growth took place in a vibration-free crystal growth refrigerator from Molecular Dimensions at 16 °C. The crystals were mounted in small loops of fine rayon fiber and flash-cooled directly in liquid nitrogen after being dipped into the cryoprotectant solution that contained 0.1 M MOPS pH (6.5), 17% PEG 20000 and 30% ethylene glycol. Initial screening was carried out using a Rigaku MicroMax 007 HF Cu-rotating anode X-ray generator, operated at 40 V and 30 mA, and utilizing a Saturn 944 CCD area detector at Emory University. X-ray

diffraction data of Fe(III)-, putative Fe(II)-bound peroxo pirin, Mn(III)-, and Co(II)-pirin were collected by the Rigaku X-ray facility. X-ray diffraction data of Mn(II)-pirin was collected at the SER-CAT beamline 22-ID at the Advanced Photon Source (APS), Argonne National Laboratory, Argonne, IL. All data collection was performed at 100 K. The diffraction data were indexed, integrated and scaled with HKL2000 (*37*). The structures were solved by molecular replacement using MOLREP program (*56*) of the CCP4 suite (*39*) with Fe(II)-pirin structure (PDB accession number 1J1L) (*12*) as search model. Electron density was fit and refined using Coot (*40*), REFMAC (*42*) and PHASER (*97*). Figures showing crystal structures were drawn with PyMOL (http://ww.pymol.org).

5.3.7 In silico docking of the supercomplex

The docking model of pirin with p65 and κB DNA was constructed by using the ZDOCK utility and server (http://zdock.umassmed.edu) (*98*). The PDB files of ferric pirin (PDB accession number 4GUL) and p65 (1RAM) (*99*) were used in model building. The top-ranked result shown in Figure 5 involves the *R*-shaped area of pirin, which has been shown in the structural study to differ in conformation when the metal oxidation state changes or metal substitution occurs.

5.3.8 Experimental validation of the docking study

The modeling results were further tested by site-directed mutagenesis experiments. The point mutants of pirin were generated by using the QuikChange II kit purchased from Qiagen (for details, see Supplementary Information). The sequences of the mutants were verified by DNA sequencing prior to expressing and purifying proteins. The procedures used for the expression, purification, metal-reconstitution and oxidation of the pirin variants were the same as described previously for the wild-type protein.

5.3.9 Accession codes

Atomic coordinates and structure factors have been deposited with the Protein Data bank under accession codes (resolution): 4GUL (1.80 Å), 4EWA (2.47 Å), 4EWE (1.56 Å), 4ERO (2.65 Å), 4EWD (2.15 Å), and 4HLT (1.70 Å).

5.4 Results

5.4.1 Human pirin facilitates the DNA binding of p65 to the κB gene in a redox-state dependent manner

We studied the effect of pirin on the binding affinity of p65 (residues 19-291) (*99*) homodimers to the immunoglobulin κB target sequence (IgκB) by testing isolated protein using surface plasmon resonance (SPR) spectroscopy. The first significant observation is that Fe(III)-pirin, generated by oxidizing Fe(II)-pirin with ferricyanide, or O_2 in a relatively slower oxidation process, and verified by EPR spectroscopy substantially enhanced p65 binding to the IgκB target site (Figure 5.1A). In the presence of 0 – 25 μM Fe(III)-pirin, the binding was a two-phase process: a fast phase in the first 60 s with $k_{on1'}$ = 1.1 $\times 10^6$ $M^{-1}s^{-1}$ and a slow association phase after 60 s with $k_{on2'}$ = 0.02 $M^{-1}s^{-1}$. The buffer rinse only resulted in the loss of a small amount of mass presumably due to washing away of non-specifically bound proteins observed in the slower binding phase. The binding is very tight, virtually no dissociation after removing non-specifically bound proteins. This is the first experimental evidence of pirin interacting with p65 and dramatically enhancing the binding affinity for p65 to the κB site. In contrast, Fe(II)-pirin does not affect p65 binding to the IgκB site. The dose response with the truncated p65 is shown in Figure 5.1B. The sequence specificity of pirin's effect on p65 has been tested by performing the same SPR experiment using a non-specific DNA sequence. Not surprisingly, the pirin-p65 complex did not interact with the non-specific DNA sequence regardless of the formal oxidation state of the iron ion in pirin.

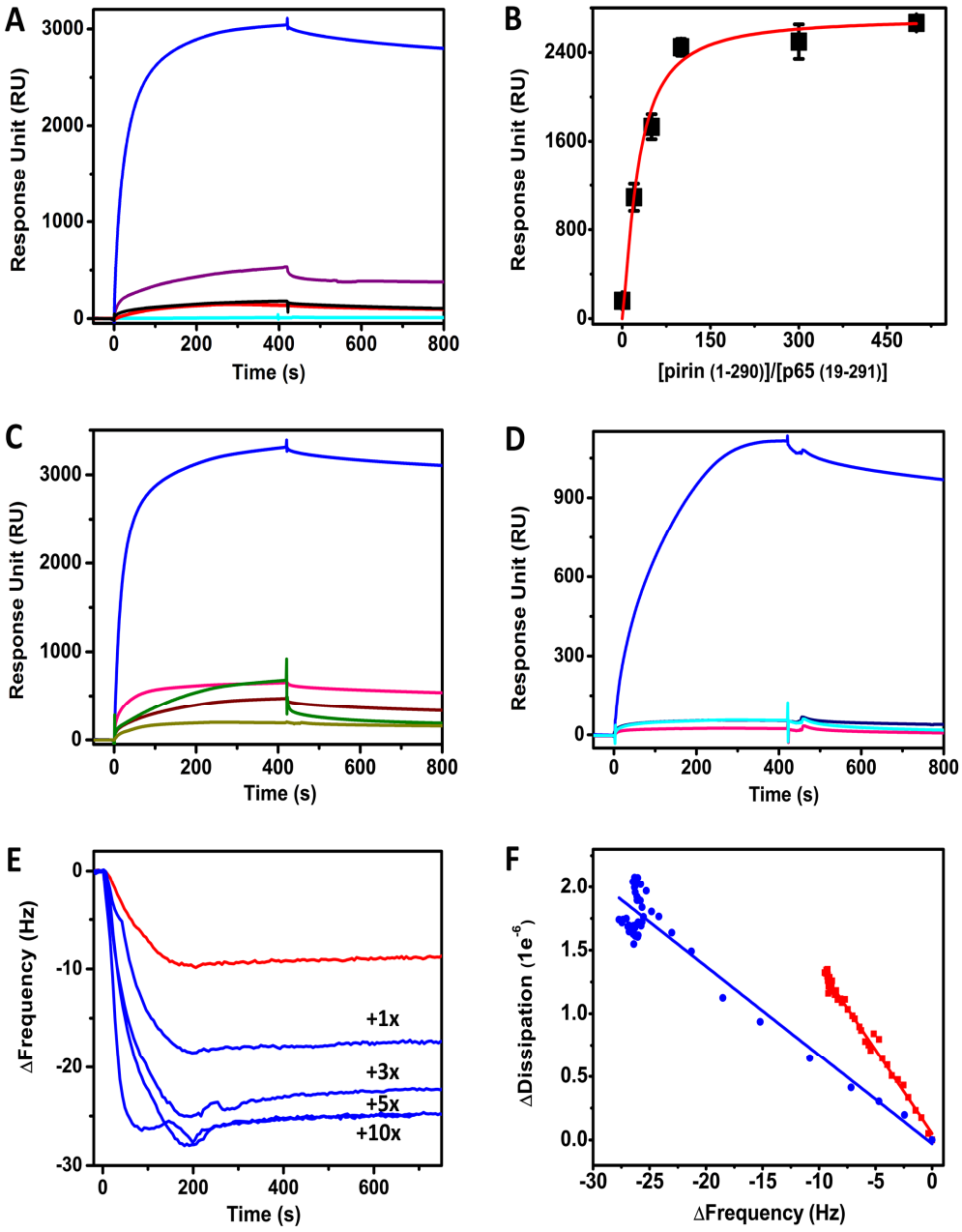

Figure 5.1 The ferric, not ferrous, form of pirin substantially facilities binding of p65 to IgκB gene in SPR spectroscopy. (**A**) Detection of apo-, Fe(II)-, and Fe(III)-pirin effect on p65 binding to the IgκB site, (**B**) the response unit as a function of the pirin (1-290):p65 (19-291) ratio, (**C**) SPR spectroscopy with Fe(III)- and metal-substituted pirin proteins, (**D**) The effect of exogenous pirin to native NF-κB of the nuclear extract of HeLa cells, (**E**) QCM-D spectroscopy of p65 alone (red trace) and along with Fe(III)-pirin in (1:1 to 1:10 ratio as indicated by 1x, 3x, 5x, and 10x), and (**F**) comparison of the ΔD/Δf slope in a QCM-D study that indicates a conformational difference of the protein-DNA complex. The SPR traces are color-coded with p65 only (red), p65 with Fe(II)-pirin (black), Fe(III)-pirin (blue), metal-striped pirin (purple), Co(II)-pirin (pink), Mn(II)-pirin (dark yellow), Mn(III)-pirin (wine), and Ni(II)-pirin (olive). Fe(III)-pirin alone (cyan) is shown in (**A**) and HeLa nuclear extract only (navy) is shown in (**D**) as controls, respectively.

To determine whether other transition metal ions can function in place of the iron cofactor, apo-pirin was prepared from Fe-depleted minimal medium and charged with divalent metal ions. Co-, Mn-, and Ni-reconstituted proteins were stable and contained about 0.6 metal ions per molecule of pirin as determined by ICP-OES analysis (Table 5.1). These metal-substituted pirin proteins had minimal effects on p65 and were unable to achieve the effect observed for NF-κB with ferric pirin (Figure 5.1C). We wondered if a metal, other than iron, with correct valence state (*i.e.*, trivalent) would make pirin active. We oxidized Mn(II)-pirin protein using potassium ferricyanide. After an overnight incubation, the protein was desalted to remove the oxidant and crystallized. As the oxidation state rises, each metal ligand increases its bond length in the Mn-substituted pirin metal center, a scenario similar to what is observed in Fe-pirin structures. The change of the oxidation state of pirin was validated by low temperature EPR spectroscopy measured before and after the oxidation reaction by the disappearance of the Mn(II) EPR signal. This is the same method we used to generate Fe(III)-pirin from Fe(II)-pirin, with the exception of a shorter incubation time (4 h) and after which the colorless Fe(II)-pirin turned into a pale yellow colored solution and a high-spin (S = 5/2) ferric EPR signal was fully developed from the EPR-silent state. As shown in Figure 5.1C, the Co(II)-, Mn(II)-, and Mn(III)-substituted pirin proteins have little or no activity towards NF-κB. A similar effect was also observed by fluorescence spectroscopy. When the 5'-FAM-labeled κB DNA was titrated by p65 in the absence of pirin, the 520 nm emission intensity increased as previously reported (*100*). In contrast, the titration using p65 and Fe(III)-pirin induced an increase in emission signal intensity that was nearly 4-fold larger than p65 alone, an effect not seen when pirin is complexed with other metals such as Co(II) and Cu(II) (Figure 5.2). The change in fluorescence intensity as a function of p65 concentration resulted in a sigmoidal curve, indicative of the binding cooperativity previously reported in studies of NF-κB and DNA interactions (*100*). All the available reducing agents affect the fluorescein in FAM and resulted in less excitation energy. Thus, the fluorescence assays with Fe(II)-pirin cannot be performed in the current stage.

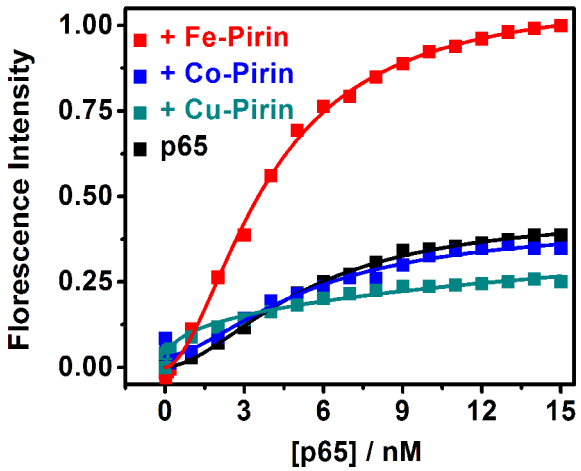

Figure 5.2. Fluorescence spectroscopic study of pirin's effect on p65's binding to the IgκB gene. The concentration of p65 is plotted as a function of the change in emission intensity originated from the 5'-FAM fluorescent label of the IgκB DNA in the fluorescence study.

Table 5.1. Metal analysis of Pirin by inductively coupled plasma optical emission spectrometry (ICP-OES). Values were obtained as average of three measurements with standard errors less than 5%. The data are present as molar ratio per pirin molecule.

Human Pirin Protein	Fe	Zn	Cu	Mn	Co	Ni
As-isolated untagged recombinant pirin	0.63	0.19	<0.01	<0.01	<0.01	<0.01
Metal-free apo-pirin	<0.10	<0.01	<0.01	<0.01	<0.01	<0.01
Fe-reconstituted, from apo-pirin	1.00	<0.01	<0.01	<0.01	<0.01	<0.01
Co-reconstituted, from apo-pirin	<0.01	<0.01	<0.01	<0.01	0.60	<0.01
Mn-reconstituted, from apo-pirin	<0.01	<0.01	<0.01	0.63	<0.01	<0.01
Ni-reconstituted, from apo-pirin	<0.01	<0.01	<0.01	<0.01	<0.01	0.61

Pirin's effect on NF-κB was further investigated with native NF-κB proteins in cell lines. Figure 5.1D shows the effect of isolated pirin on the nuclear extract from HeLa cells, which were not under redox stress, *i.e.* the NF-κB proteins were not yet induced for activation. The freshly prepared nuclear extract (at a total protein concentration of 0.08 μg/ml) was injected into the IgκB-coated SPR sensor chip simultaneously with exogenous Fe(III)-pirin. The inclusion of isolated Fe(III)-pirin protein with the nuclear extract increased binding by about 25-fold compared to the extract alone. Fe(II)-pirin and metal-substituted pirin failed to induce the same effect.

5.4.2 The protein-DNA supercomplex in the presence of pirin is compact and rigid

We also tested if NF-κB and the DNA change their structures after forming a complex. Quartz crystal microbalance with dissipation (QCM-D) was employed to monitor pirin's effect on the conformation of the p65-DNA complex (Figure 5.1E). The plot of the change in dissipation (ΔD) vs. the shift in frequency (Δf) displays a more moderate slope when pirin is present (Figure 5.1F). A less steep ΔD vs. Δf slope indicates a more compact, rigid layer formed upon the sensor (*101*). This result suggests that the conformation of the supercomplex is altered with respect to the NF-κB and DNA mixture. This observation is also consistent with previous studies showing that κB sequences are bent to various degrees upon NF-κB binding (*75, 102*). DNA bending is a common prerequisite to the formation of a fully active transcriptional complex (*103*).

5.4.3 Pirin-NF-κB-DNA supercomplex dissociates by added reducing agent

We determined the midpoint reduction potential (E_m) for the ferrous/ferric couple of pirin by cyclic voltammetry. The resulting curve shown in Figure 5.3A resembles published data on the non-heme Fe_B of nitric oxide reductase (*104*). At pH 7.4, the E_m value is +80 mV vs. an Ag/AgCl electrode.

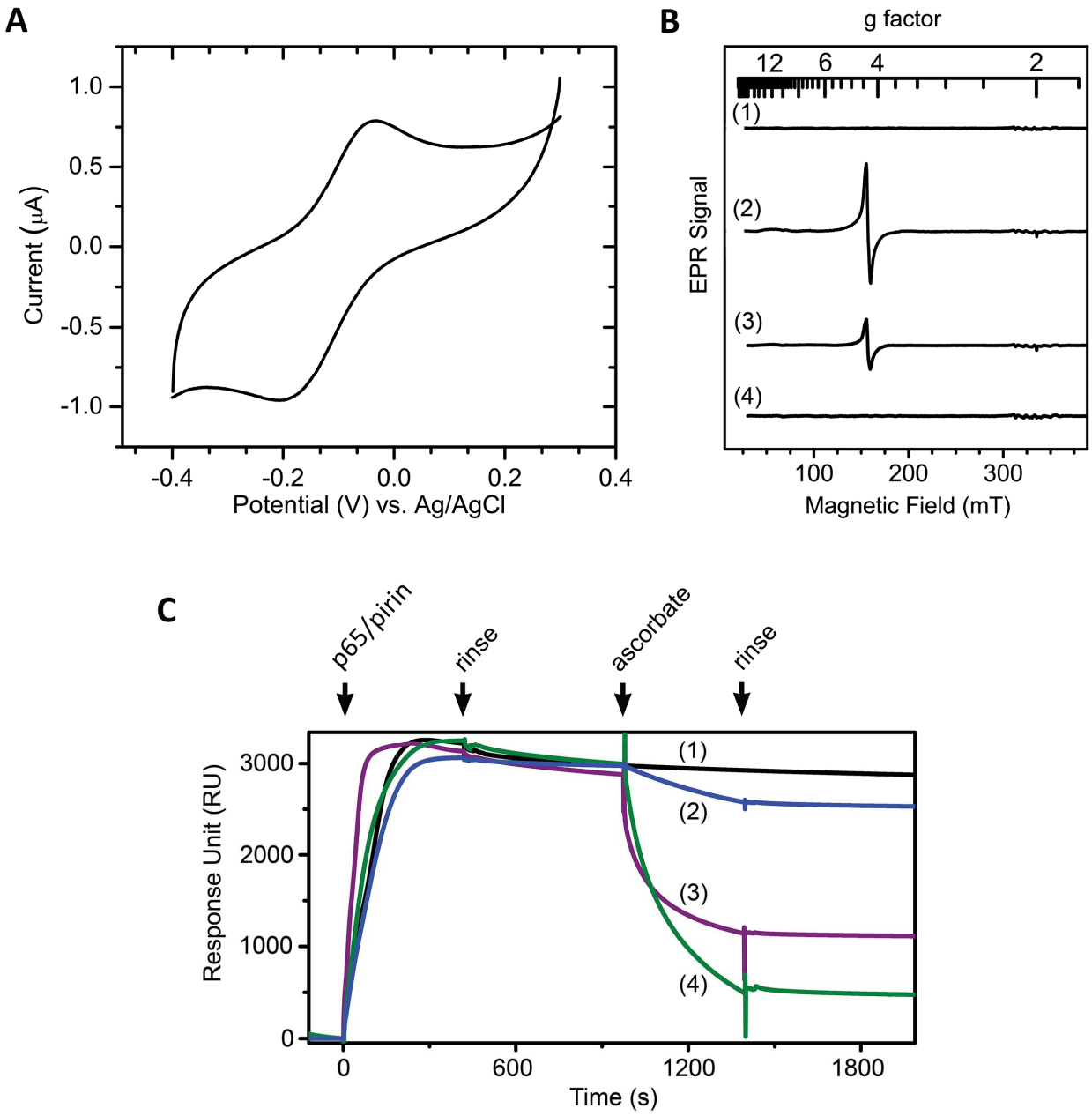

Figure 5.3 The function of pirin on p65 is reversible depending on the redox state of the iron center. (**A**) Determination of the reduction potential of pirin by film cyclic voltammetry in an anaerobic chamber. (**B**) X-band EPR spectroscopy shows reversibility of the Fe(II)/Fe(III) couple in response to L-ascorbate. Fe(II)-pirin (250 μM, trace 1) after oxidation by O_2 for 30 min (or 1 equivalent of H_2O_2 for 1 min, trace 2), addition of 1 mM L-ascorbate for 5 min (trace 3) and for 60 min (trace 4). (**C**) L-ascorbate was introduced to the system, after forming the supercomplex from initial injection of p65/Fe(III)-pirin, at concentrations of 0 (black), 0.25 (navy), 2.5 (magenta), and 25 mM (green) at 980 s.

If pirin is indeed a regulatory component in the NF-κB signaling transduction, it must be able to dissociate after the redox levels resume to normal. We designed a continuous SPR experiment to test if L-ascorbate would be able to dissociate the pirin•p65•IgκB supercomplex (Figure 5.3C). First, the supercomplex was formed and the non-specifically bound proteins were washed away by buffer. At this point, L-ascorbate was introduced to stimulate a shift in intracellular redox conditions to a less oxidative environment. Figure 5.3C shows that L-ascorbate caused the protein supercomplex to dissociate in a dose-dependent manner, and buffer wash without the L-ascorbate immediately halted the dissociation.

5.4.4 The redox state of the Fe in pirin affects the conformation of a specific R-shaped surface area as revealed by X-ray protein crystallography

To further our understanding of the structural impact of pirin metal center, especially the differences between the active Fe(III- and inactive Fe(II)-pirin and the metal-substituted pirin variants, we determined multiple X-ray crystal structures of the active form of Fe(III)-pirin at 1.80 to 2.50 Å resolutions (Table A3). All the pirin crystals, including we analyzed and previously published (*12*), belong to the $P2_12_12_1$ space group with one molecule per asymmetric unit.

An apparent structural change is observed when the active ferric form of pirin is aligned with the inactive resting state of ferrous pirin. Figure 5.4A shows that the deviations are primarily located on one face of the protein. The residues involved collectively account for ca. 20% of 290 total residues. Notable in our structural study, a specific, *R*-shaped surface loop area is identified that is substantially altered due to switching of the metal oxidation state. This area consists of residues 7–41 and 53–62 which includes the surface area surrounding the metal binding cavity at the N-terminus as well as the interface between the two cupin domains. While the root-mean-square deviation (r.m.s.d.) of shift in the protein backbone of this *R*-shaped region between the Fe(II) and Fe(III) states is modest, the widespread

coverage and especially the cumulative effect of the changes in the amino acid residues is extensive for a protein of this size. Both sheet-to-coil transition and twist of orientations are observed in the *R*-shaped region. Four charged residues (Arg14, Arg23, Glu32, and Lys34) in the *R*-shaped region show two distinct conformations depending on the oxidation state of Fe (Figure 5.5). Arg14, for example, shifts 5.1 Å by comparing the two structures (Figure 5.4B).

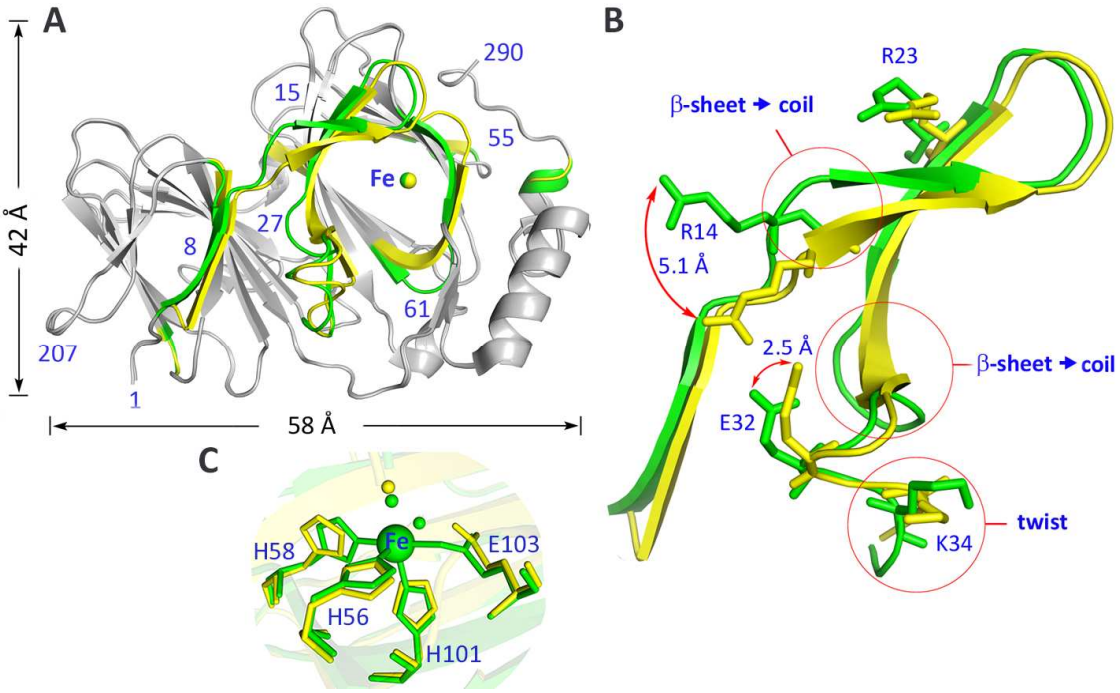

Figure 5.4 Structural comparison of ferric and ferrous pirin. (**A**) Structural alignment of ferric (active towards p65) and ferrous (inactive) pirin. Colored regions indicate areas of deviation (≥ 1 Å), while grey regions are identical. The structural differences of Fe(III)-pirin are shown in yellow, and Fe(II)-pirin in green. (**B**) the zoom-in view highlights the deviation of a special *R*-shaped area with distinct conformations, and (**C**) superimposed Fe center structure of ferric (yellow), ferrous (green) and L-ascorbate-reduced (cyan) pirin structures.

The structural data also provide clues for the cause of the extensive conformational changes. His56, His58, His101 and Glu103 are the coordination ligands at 2.1, 2.1, 2.3 and 2.3 Å distance from the Fe(II) ion respectively. While the histidine residues remain coordinated to the Fe ion at 2.1, 2.1 and 2.2 Å, the negatively charged ligand, Glu103, moves away from the Fe ion in the oxidized protein (Figure

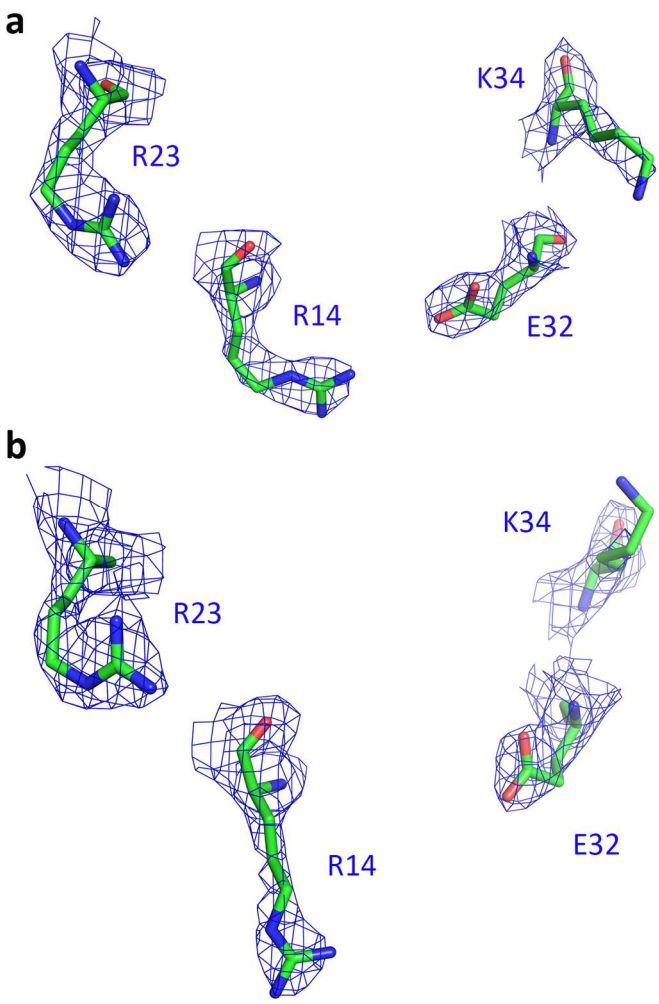

Figure 5.5. Key residues at the "active site" of pirin in the *R*-shaped surface loop including—the relative orientation and the electron densities of Arg14, Arg23, Glu32, and Lys34 in the structural data. (a) Fe(III)-pirin (4GUL) and (**b**) Fe(II)-pirin (1J1L). The 2*Fo*-*Fc* electron densities are contoured at 1.0 σ.

5.4C). The Fe-Glu103 distance lies in 2.5 - 3.2 Å in multiple ferric pirin structures determined (Figure 5.6). This is an unexpected observation. However, the positively charged Fe ion still sits in a highly negatively charged cavity. We noticed that Glu103 connects the *R*-shaped surface through a well-defined H-bond network (Figure 5.7). It is highly possible that redox state change-induced *R*-shape loop deviations are mainly triggered by the iron ion through Glu103.

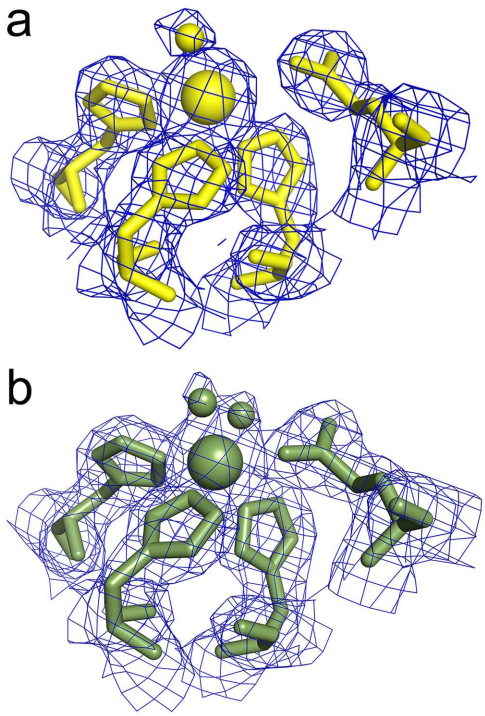

Figure 5.6 The electron density comparison of fully oxidized and reduced pirin iron centers. (**a**) Fe(III)-pirin (4EWA) and (**b**) Fe(II)-pirin (1J1L). The 2*Fo*-*Fc* electron densities are contoured at 1.0 σ. Note that the exact number and the chemical nature (i.e., water or hydroxide) of the solvent-derived ligands cannot be definitely determined by X-ray protein crystallography at these resolutions and they may be affected by X-ray resource during data collections.

5.4.5 The crystal structures of the intermediate states of Fe-Pirin show the reversibility of the R-shaped loop conformation changes dependent on the oxidation state of the metal

We have trapped the intermediate states of Pirin in response to changes in the redox environment (Figure 5.8). The crystals from Fe(II)-Pirin protein grown in an anaerobic chamber, but frozen with aerobic cryoprotectant, gave rise to an intermediate state of Pirin structure which is different from either the ferrous- or ferric-Pirin structures. A diatomic molecule (Fig. 5.9A), assigned as oxygen, occupies the Fe site opposite three His ligand residues. No diatomic molecule that can bind to Fe(II) other than O_2 is present in the crystallization or cryoprotectant medium. Attempts to fit the electron density with only a single atom or with two solvents were unsuccessful and resulted in excess residual electron density. Thus, this is a putative O_2-bound state of Pirin. The bound dioxygen is ligated

to the Fe(II) ion in a distorted side-on fashion (Fig. 5.9B), as previously seen in the non-heme Fe dioxygenases (*107, 108*). The O-O bound distance, upon crystallization refinement, converged to 1.35 Å. However, the low resolution of 2.5 Å does not definitively describe the state of the bound dioxygen species. Nevertheless, Glu103 is no longer a metal ligand (3.00 Å) as seen in the ferrous structure, but rather it is similar to what is observed in the ferric state (3.20 Å). The bound O_2 molecule is stabilized by Glu103 and Gln115, while Phe53 and Trp117 provide hydrophobic shielding. As described above, soaking Fe(III)-Pirin crystals with vitamin C resulted in the structure being nearly identical to the Fe(II)-Pirin structure, collectively demonstrating the reversibility of the specific structural confirmation in respond to the change of Pirin's redox state.

Differences in surface loops are also observed. The peroxy state of Pirin is more closely aligned

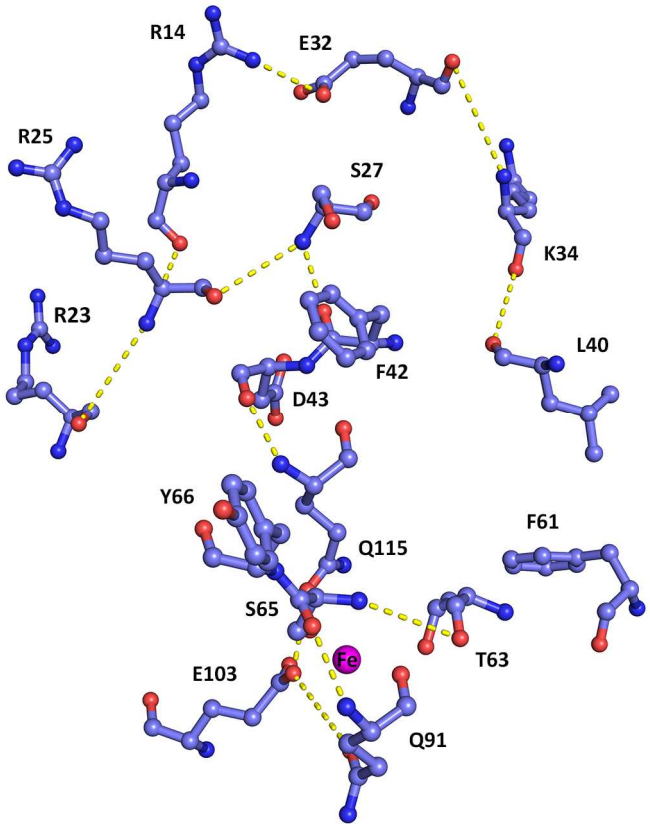

Figure 5.7 The Fe center is connected to the pirin "active site" residues (including Arg14, Arg23, Glu32, and Lys34) through a H-bond network. The metal ligand Glu103 is proposed to trigger conformation changes of the surface residues.

with the Fe(III) structure than Fe(II)'s, although it is not identical to either (Fig. 5.8). The conformal changes again are in agreement with the trend of the reversible conformational changes in the *R*-shaped region highlighted in color in Fig. 5.4A. Moreover, the structural characterization of the Fe(II)-bound peroxo species has profound implications to our understanding of how the non-heme Fe center in Pirin interacts with molecular oxygen. This observation opens an alternate avenue for Pirin to function as an O_2 sensor for NF-κB, which reversibly binds O_2, and thus not necessarily becomes oxidized to the ferric state. At present, it is not feasible to perform SPR-based assays with the crystallized intermediate state of Pirin.

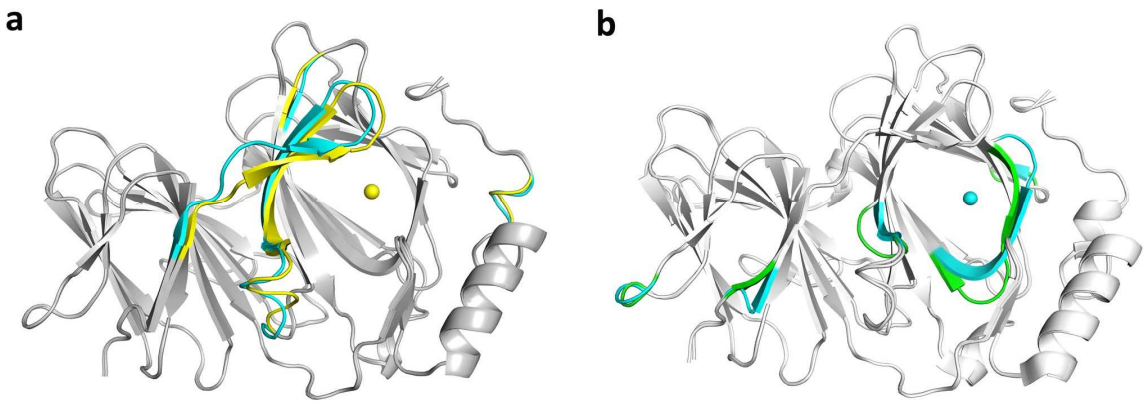

Figure 5.8 Structural alignments of (a) Fe(III)-pirin before and after L-ascorbate soaking, and (b) comparison of the *in crystallo* reduced structure with the fully Fe(II)-pirin structure. The well-aligned parts are shown in grey and differences in color with Fe(III)-pirin structure shown in yellow, L-ascorbate-reduced Fe(II)- and Fe(II)-pirin shown in cyan and green, respectively.PDB entries: Fe(II)-pirin, 1J1L; Fe(III)-pirin, 4GUL; and L-ascorbate-reduced pirin, 4FHS.

5.4.6 The metal identity affects the conformation of the R-shaped surface area

In order to understand the structural basis for the functional incapability of metal-substituted pirin proteins, we solved the X-ray crystal structures of Co- and Mn-substituted pirin. A similar *R*-shaped conformational difference is observed when comparing the active form of ferric pirin with functionally inactive pirin variants charged with Co(II) and Mn(II) (Figure 5.10). The changes in the *R*-shaped region

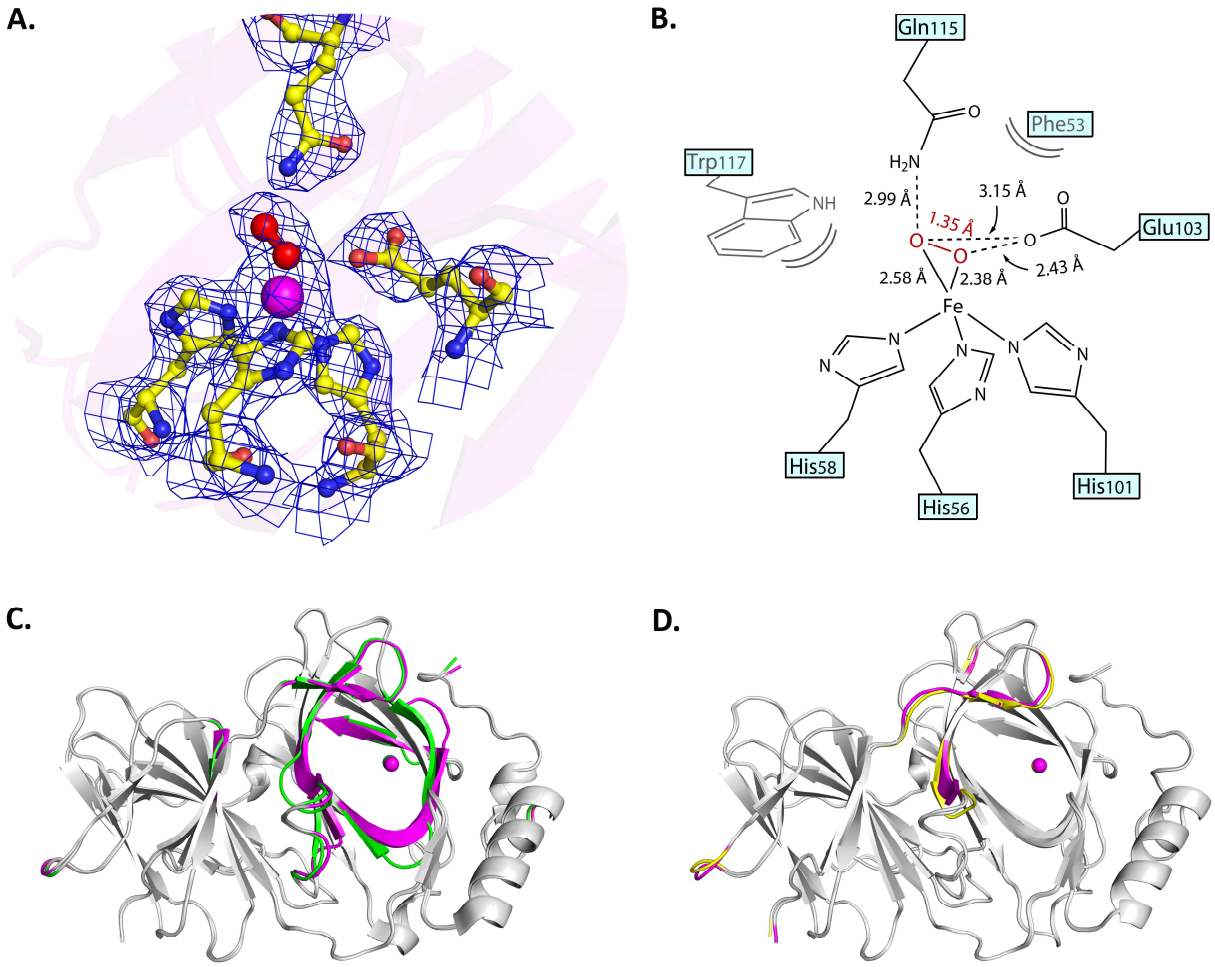

Figure 5.9 An Fe(II)-bound peroxo intermediate state of human pirin, which is structurally similar to Fe(III)-Pirin but distinct from the Fe(II) state of Pirin. (A) Electron density map of the Fe(II)-O_2 complex. The 2*Fo*-*Fc* electron densities are countered at 1.0 σ. (B) The O_2 molecule is bound to the Fe(II) at a distorted side-on fashion, which is stabilized by Glu103 and Gln115, and is shielded by Phe53 and Trp117. The Glu103 reside is no longer a metal ligand in the peroxy state of Pirin. (C) Alignment of the Fe(II)-Pirin (green) versus Fe(II)-O_2 (purple), and (D) Fe(III)-Pirin (yellow) versus Fe(II)-O_2 Pirin. Colored regions indicate areas of deviation, while grey regions are identical.

are different from one transition metal to the next, but the location and direction of the conformation changes show the same general trend. In order to understand why oxidized Mn-pirin is not active, which has an oxidation state of +3, we determined its crystal structure (Figures 5.10 and 5.11). The structure of Mn(III)-pirin (at 2.15 Å resolution) indeed differs from Fe(III)-pirin, but the conformation differences are not the same as Mn(II)-pirin (1.56 Å resolution).

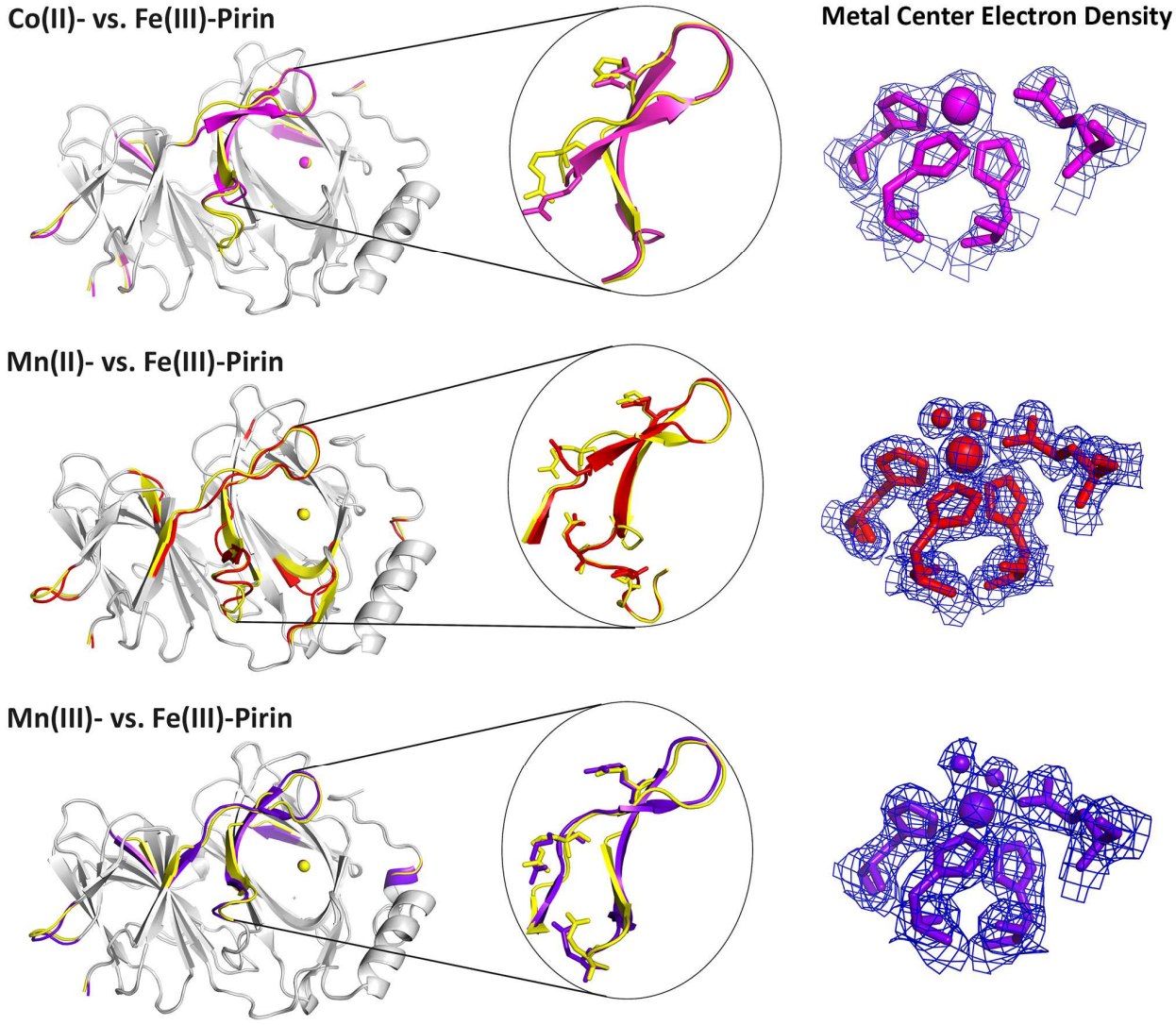

Figure 5.10 Structural alignments of Co(II)- (magenta, 4ERO), Mn(II)- (red, 4EWE), and Mn(III)- (purple, 4EWD) against Fe(III)-pirin (yellow, 4EWA). The metal center electron density maps are shown at the right column. The well-aligned parts are shown in grey and differences in color.

5.4.7 The R-shaped region on pirin interacts with the C-terminal domain of NF-κB proteins

The structural data led us to hypothesize that the *R*-shaped region is the key protein surface in pirin that directly interacts with p65. A docking model study was subsequently conducted using ZDOCK (*98*) to further investigate how pirin makes contacts with p65 (*99*). The result suggests that the *R*-shaped surface region is the pirin·p65 interface. The *R*-shaped region forms much of the central binding surface between the two proteins (Figure 5.12). The binding takes place at the C-terminal Rel homology domain. The most interesting finding from the docking study is the presence of four ion pairs interacting between pirin and p65. The *R*-shaped surface residues Arg14, Arg23, Glu32, and Lys34 of ferric pirin are electrostatically complemented by p65 residues Glu279, Glu282, Arg273 and Glu234 at distances of 3.2, 2.7, 3.0, and 3.5 Å, respectively, forming four ion pairs (Figure 5.13). Interestingly, these four residues contribute to the major changes of the *R*-shaped region as shown in Figure 5.4. In contrast, these ion pair interactions are missing when the Fe(II)-pirin structure is used for docking.

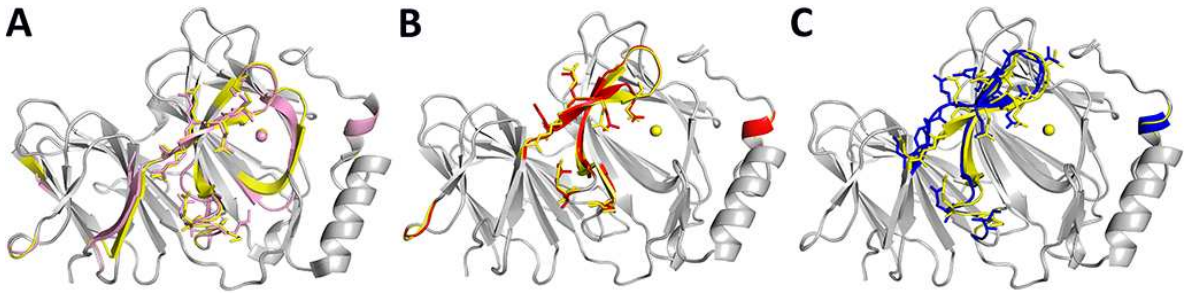

Figure 5.11 Structural differences shown in the alignment of ferric pirin (yellow) (**A**) with Co(II)-substituted pirin (pink), (**B**) with Mn(II)-pirin (red), and (**C**) with Mn(III)-pirin (blue). Colored regions indicate areas of deviation (≥ 1 Å), while grey regions indicate identical structural features.

The *R*-shaped region was tested by site-directed mutagenesis. R23E, E32V, K34V, and double mutant S13R/R14W of the *R*-shaped region mutants were generated and analyzed. These pirin variants were reconstituted with Fe(II) and oxidized prior to SPR analysis in the same manner as the wild-type protein. Figure 5.14A shows that these mutations have a significant adverse effect on the binding of pirin to p65 compared to the wild-type protein, reducing the binding efficiency to one to two-thirds of the wild-type.

While there was less DNA binding in these mutants, the resulting supercomplex was still tightly bound and showed a similar lack of dissociation as the wild-type. Q115N pirin was generated and used as a control along with wild-type pirin. Q115 is not part of the R-shaped region. It is located in the interior of the protein. Not surprisingly, Q115N essentially behaved the same as wild-type pirin. These results demonstrate that site-directed mutation of the surface loop residues dramatically changes the ability of pirin to facilitate p65 binding to the κB site and thereby supports the docking model.

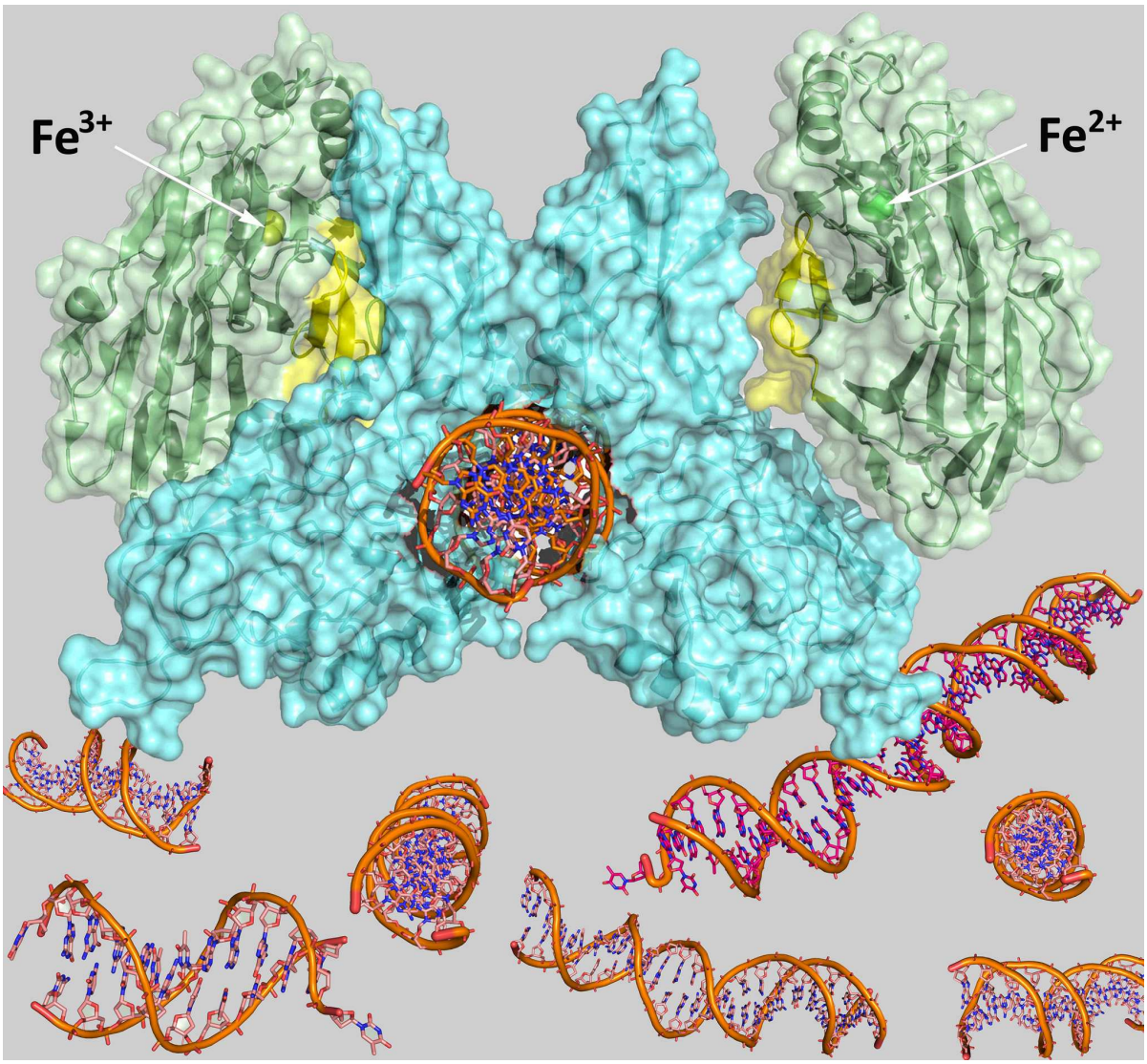

Figure 5.12 A docking model of pirin (green/yellow)-p65 (blue)-IgκB (golden/blue) supercomplex built from the corresponding crystal structures (see Materials and Methods). The *R*-shaped region is highlighted in yellow and the Fe ion is represented in the sphere (ferric in yellow and ferrous in light green).

An 1.70 Å resolution crystal structure of the E32V mutant was obtained in its oxidized form (4HLT, Table A5). The structure shows that mutation of Glu32 disrupts the electrostatic interaction between Glu32 and Arg14 (Figure 5.14B). The two residues are within 3.2 Å in the ferric form of native pirin, but Val32 and Arg14 are 9.4 Å apart in E32V. Consequently, the position of the guanidinium group of Arg23 is also shifted. Among the four charged residues, Lys34 is the only residue that is nearly not affected by mutation. This structure provides a molecular rationale for the negative impact of the

mutation. Together, these data validate the *R*-shaped region as the functionally important area of pirin for interaction with p65.

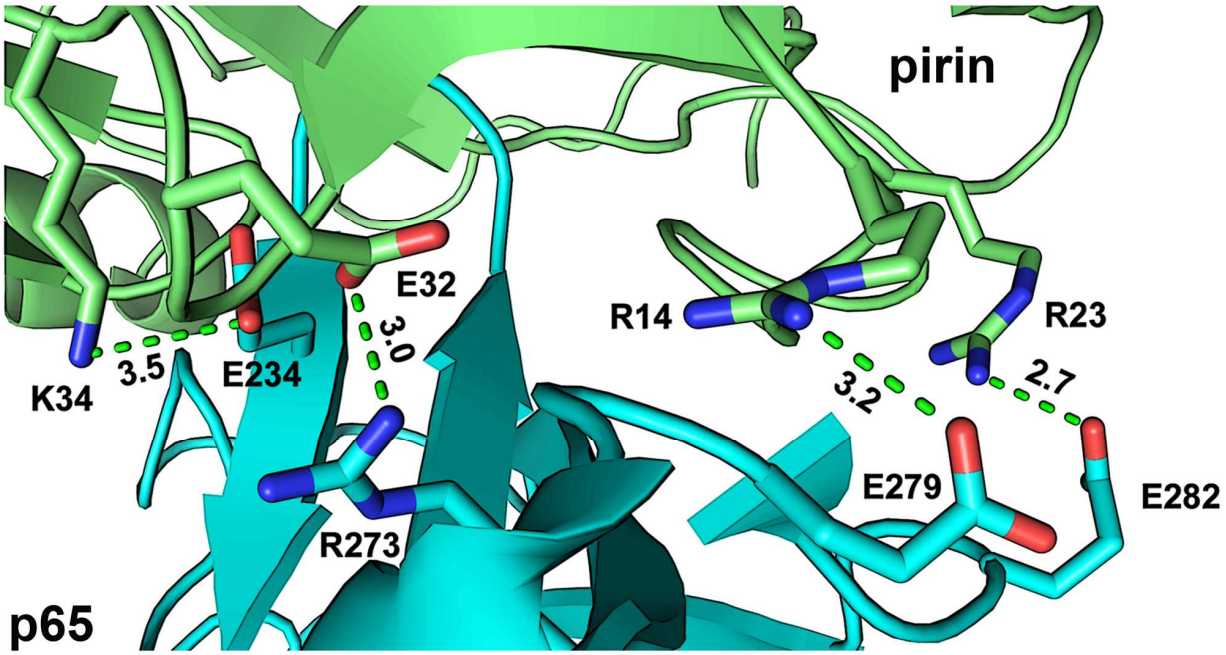

Figure 5.13 The zoomed-in view of the pirin (top, green)-p65 (bottom, cyan) interface region shows multiple complementary ion-pair interactions including K34-E234, E32-R273, R14-E279, and R23-E282 (pirin-p65).

5.5 Discussion

Based on previous work and this study, it is concluded that pirin is a redox sensor in the cell nucleus that functions as a co-regulator of NF-κB (*109*). Figure 5.15 presents an iron-dependent bioinorganic scheme for how NF-κB could respond to redox changes within the nucleus. Previous studies have established that NF-κB activation is first achieved by phosphorylation of the inhibitory IκB proteins in the cytoplasm to liberate NF-κB. Upon translocation of NF-κB to the nucleus, several layers of activation take place involving different co-regulators and mechanisms. In the nucleus, under normal reducing conditions, pirin resides in its inactive ferrous state. The results presented here show that, when the redox environment shifts to more oxidizing conditions, pirin responds by changing to its functionally active ferric form and turns on the transcription factor. This is a reversible redox process, depending on the oxidation state of the iron. The dependence of pirin on its iron cofactor is likely an additional contributing factor to the link between iron and NF-κB in the nucleus.

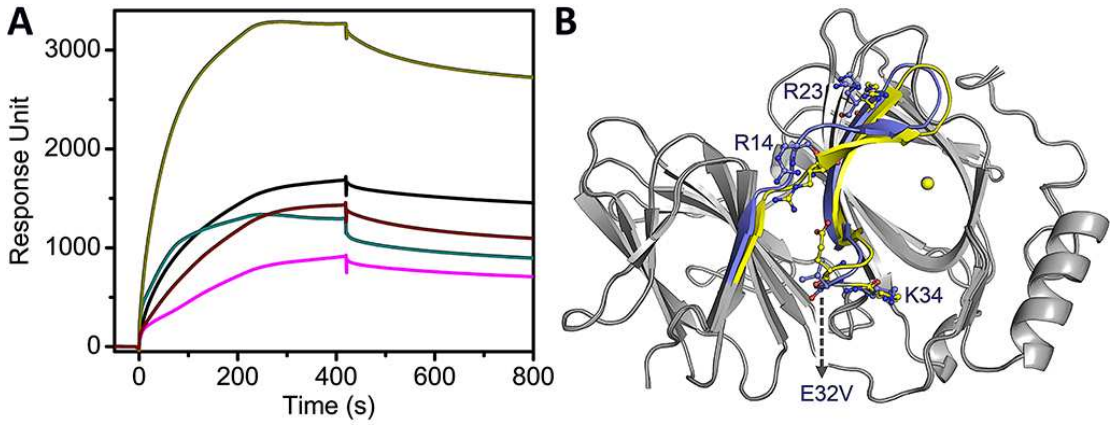

Figure 5.14 Mutation at the *R*-shaped surface impairs the ability of pirin to enhance the DNA binding ability of p65 to the IgκB site. (**A**) SPR assay using p65 and immobilized IgκB with R23E (black trace), E32V (cyan), K34V (wine), and S13R/R14W (magenta). The non-surface mutant Q115N (dark yellow) was used as a positive control, and (**B**) the crystal structure of E32V aligned with native pirin structure. Colored regions indicate areas of deviation (≥ 1 Å), while grey regions indicate identical structural features.

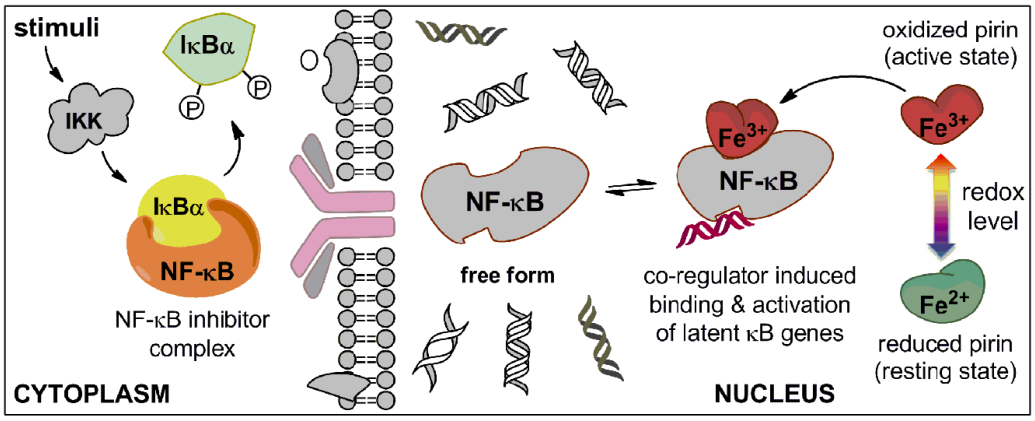

Figure 5.15 The proposed function of human pirin. This model depicts a non-heme iron- and oxidation state-dependent regulation mechanism of NF-κB in the cell nucleus.

It remains to be determined whether the proposed non-heme iron protein-based redox switch operates in vivo. However, our findings are consistent with recent biological studies showing increased expression of pirin in response to the oxidative stress (*92, 110, 111*). Interestingly, pirin-like proteins in plants and prokaryotes have also been linked to stress-induced responses and programmed cell death (*112*). Upregulation of pirin expression by chronic cigarette smoking has been associated with bronchial epithelial cell apoptosis, presumably due to increased oxidative stress that triggers Nrf2-modulated genes including pirin (*110*). The conclusion that the oxidation state and activity of pirin is regulated by cellular redox conditions is consistent with those previous findings proposing a role as a protector against oxidative stress. Thus, oxidative stress elevates both the expression of pirin and its activity. When redox levels are restored to normal reducing conditions in the cell nucleus, the transcriptional response induced by pirin may be ablated by reducing its expression and by losing its ability to form a complex with NF-κB and DNA. However, the present work does not exclude the possibility that there is another protein responsible for oxidizing pirin in the nucleus as a part of a signaling cascade.

Pirin has been proposed to be an important factor in cell differentiation (*113*). In progenitor cells, the activation of pirin is an important event that alters the transcription profile of the cell to one that primes the cell for differentiation (*113*). Reduced pirin expression is a common feature of acute

myelogenous leukemia, which results in the proliferation of immature myeloid cells. Elevation in the concentration of reactive oxygen species (ROS) has been reported to facilitate differentiation in hematopoetic progenitor cells (*114*).

Pirin utilizes a structure-based conformational switch to quickly, reversibly, and efficiently inform the transcription factor of the positive/negative shift of redox levels in the nucleus. The data presented here suggests that the Fe center in pirin is not its active site. Instead, the role of the Fe center is allosteric control. The *R*-shaped surface loop region is the site that interacts with p65. The two distinct conformational states on the *R*-shaped surface loop regions endow pirin with the ability to regulate NF-κB with full reversibility. This unique property distinguishes pirin from any other redox regulators of transcription factors, including the H_2O_2 sensor PerR found in a bacterial source (*115*). PerR and pirin are both redox sensors with a similar dependence on non-heme iron. Unlike human pirin, PerR itself is a transcription factor. The Fe ion of PerR participates in a Fenton-type reaction with H_2O_2. The result of this reaction is the formation of a hydroxyl radical that irreversibly oxidizes one of its histidine metal-binding ligands resulting in a drastically altered protein conformation that is no longer able to bind to DNA (*115, 116*). In contrast, the regulatory mechanism of redox sensing illustrated in Figure 5.15 utilizes a reversible Fe(II)/Fe(III) oxidation state coupling and a consequent reversible conformational switch. The conformational variation of the *R*-shaped loop areas of pirin can respond accordingly to the oxidation level in cell nucleus, which allows pirin to respond to redox potential shifts in both directions.

5.6 Further Experimental Details

5.6.1 Material preparations

Cloning, expression, and purification of recombinant human pirin: The full-length (1- 290 amino acids) untagged form of human pirin was cloned and expressed in *Escherichia coli* strain BL21(DE3) (Invitrogen). Cells were grown at 37°C in LB media with 50 μg/ml kanamycin until an OD_{600} around 0.6 - 0.8 was achieved. Protein expression was induced by 0.4 mM isopropyl-β-D-thiogalactopyranoside. Cells

were further grown for 16 hours at 28°C before harvesting by centrifugation at 8000 x g for 15 min. The cells were re-suspended in the lysis buffer (15 ml per gram cell pellet), which consisted of 20 mM HEPES (pH 7.5), 150 mM NaCl, 2 mM EDTA, 0.2 mM phenylmethylsulfonyl fluoride and 10 mM β-mercaptoethanol, 5% glycerol. The cell membrane was broken by an automated Cell Disruptor made by Microfluidics (M-110P) to release proteins. After centrifugation at 27000 x g for 30 min, the crude extract supernatant was subjected to ammonium sulfate fractionation. The fraction containing the target protein was re-dissolved in 20 mM MOPS (pH 6.5) buffer and desalted by a HiLoad G-25 column (2.6 x 30 cm). Pirin was purified from the desalted elute to homogeneity through three subsequent major chromatographic separation steps (Hi-Load 2.6 x 20 cm SP-Sepharose, Hi-Load 1.6 x 60 cm Superdex 75, and Mono S 4.6/100 PE columns, respectively) in the MOPS buffer on an ÅKTA Protein Purifier system.

Preparation of apo-pirin: Metal-free (apo) pirin utilized in the SPR experiment was isolated from an iron-depleted minimum medium(*96*). The purified protein was treated with 10 equivalents of EDTA overnight and then desalted with 20 mM Tris-HCl buffer (pH 7.4) containing 50 mM NaCl and 5% glycerol. The isolated protein was confirmed to be metal-free by ICP-OES spectrometry.

Metal Ion Reconstituted Pirin: Co(II), Mn(II), and Ni(II) (0.5 mM) were incubated with apo-pirin (0.05 mM) in 20 mM Tris-HCl buffer (pH 7.4) containing 50 mM NaCl. The reconstitution reaction was allowed to proceed followed by a final desalting step to remove free ions. The Co(II)-, Mn(II)-, and Zn(II)-reconstituted pirin proteins were concentrated to ~ 1 mM stock solution for further use.

The Fe(II) reconstitution reaction was initially carried out in an anaerobic chamber (COY Laboratory Products, Inc., Michigan). Apo-pirin (0.05 mM) was incubated with 1.2 equivalents of ammonium iron(II) sulfate (i.e., Mohrs salt) in a reaction vial under O_2-free conditions. The reaction vial was sealed with a rubber cap and parafilmed before being removed from the chamber. It was placed in

an ice bucket overnight with gentle stirring. The reconstituted protein was used without further desalting to minimize potential oxidation.

Preparation of Fe(III)- and Mn(III)-pirin: The oxidation of Fe(II)-pirin to Fe(III)-pirin was achieved by using an excess of potassium ferricyanide (5:1 ratio). After 4 hours of incubation, the protein was desalted to remove the oxidant. Ferric pirin shows a pale yellow color, in contrast to the colorless Fe(II) oxidation state. Likewise, oxidation of Mn(II)-pirin to Mn(III) was achieved similarly with the exception of a longer incubation time (overnight). The change of the oxidation state of pirin was confirmed by low temperature EPR spectroscopy measured before and after the oxidation reaction.

Site-directed mutagenesis of pirin: The point mutants of pirin were generated by using the QuikChange II kit (Qiagen). The forward primer sequences used for site-directed mutagenesis were as follows (mutation sites are underlined):

R23E: 5’-GAAGGGGTTGGAGCGGAGGTCCGGAGAAGCATT-3’

E32V: 5'-AGCATTGGCAGACCCGTGTTAAAAAATCTGGAT-3'

K34V: 5’-GGCAGACCCGAGTTAGTGAATCTGGATCCGTTT-3’

Q115N: 5’-CATGGCCTAAACCTGTGGGTT-3’

S13R/R14W: 5’-AGTGCTCAGGTGGGAGCAGTC-3’

The sequences of the mutants were verified by DNA sequencing prior to expressing and purifying proteins. The procedures used for the expression, purification, metal-reconstitution and oxidation of the pirin variants were the same as described previously for the wild-type protein.

Preparation of p65 and Bcl-3: The expression system of His-tagged human p65 (70 kDa, 21–325 amino acids) was kindly provided by Dr. Jim Maher (Mayo Clinic College of Medicine). The Bcl-3 expression plasmid (26 kDa, containing 119 - 359 amino acids that include the ankyrin repeat domains) was a generous gift from Dr. Ulrich Siebenlist (National Institutes of Health). All these proteins were expressed in *E. coli* strain BL21 and purified on an ÅKTA Protein Purifier system (GE Healthcare, NJ) according to

previously published procedures with minor modifications including using Cell Disruptor (Microfluidics, M-110P) for breaking cell membrane and high capacity and high resolution resins in subsequent chromatographic separation steps (*94, 117*).

DNA preparation: The κB-site DNA used in the SPR experiments was oligonucleotide 5'-biotin-GAGTTGAG**GGGACTTTCC**CAGGC-3' (The NF-κB binding site, IgκB site, are highlighted in bold). These sequence-specific oligonucleotides and their respective complementary counterparts were synthesized by Integrated DNA Technologies, Inc (Coralville, Iowa). The single strand DNA was annealed to its complementary strand before use.

5.6.2 Method description

Surface plasma resonance (SPR) measurement with isolated proteins: Biotinylated IgκB-site DNA was immobilized to streptavidin-coated sensor chips using standard procedures and sensorgrams were generated using a Biacore T200 (GE Healthcare). The protein-DNA binding was carried out at 20 °C in 20 mM Tris-HCl, (pH 7.4), containing 50 mM NaCl and 0.005% surfactant P20 at a 50 µl/min flow rate. Each sensor chip contained four channels. The first and third of which were reference channels that did not contain immobilized DNA and they were used for a blank baseline reading that was subtracted from each measurement presented in the sensorgrams (channel #2 – #1 and channel #4 – #3, respectively). The second channel was used to study protein binding to IgκB-site DNA and the last channel was an additional control by which a non-specific DNA sequence of 5'-CCTATATGCGGCGTATATCC-3' was immobilized (1000 RU, about 1 ng/mm^2 of protein or DNA (*118*)). The effect of pirin upon NF-κB binding the IgκB sequence was studied by flowing the protein over the sensor chip and comparing the levels of DNA binding in the absence and presence of the putative co-regulator protein. The final concentration of p65 and p50 was 50 nM in the SPR injection buffer while pirin's concentration was varied from 0 - 25 µM. In the p50 experiment, Bcl-3 was included at a concentration of 25 nM. After injecting protein samples for 420 seconds, buffer was injected from 420 - 1220 s to rinse the weakly bound proteins from

the chip surface in order to monitor the dissociation of the protein or protein complexes. Vitamin C was injected at 980 s in the reversibility testing experiments. The sensor chip surface was regenerated with 0.1% SDS and 3 mM EDTA between each measurement.

SPR measurements under anaerobic conditions: To perform anaerobic Biacore experiments involving the aforementioned Fe(II)-pirin, the SPR system was primed with O_2-free, argon-saturated 20 mM Tris-HCl buffer (pH 7.4), containing 50 mM NaCl and 0.005% surfactant P20 at least 4 times over half an hour. All the proteins, including Fe(II)-pirin, were pre-treated in sealed reaction vials attached to a Schlenk line by 20 – 30 gentle vacuum/argon cycles with stirring at 4 °C. The SPR experiments were conducted with the argon-saturated buffer at 20 °C.

SPR measurements with HeLa cell-free nuclear extract: Nuclear extract of HeLa cells was prepared by using the subcellular protein fractionation kit for cultured cells from Pierce Protein Research Products (part of Thermo Fisher Scientific, Rockford, IL), according to the manufacturer's protocols. Prior to injection, the extract was diluted to 0.08 µg/mL by the SPR binding buffer described above. The binding measurements were taken with the extract alone and together with added pirin (10 µM) protein.

Analysis of the SPR data: In the absence of pirin, the data of NF-κB binding to the IgκB sequence was fitted by the following one-phase exponential association equation (eq.1) for calculating the binding rate constant (K_{on}):

$$R_{(t)} = R_{max} \times (1 - \exp(-K_{on} \times t)) \qquad \text{(eq. 1)}$$

where *t* represents injection time and *R* represents response unit.

In the presence of pirin, the binding curve in the sensorgrams exhibited a two-phase association pattern. The data of NF-κB binding was fitted to the following two-phase exponential association equation (eq. 2) for calculating the binding rate constants (K_{on1} and K_{on2}, respectively):

$$R_{(t)} = R_{max1} \times (1 - \exp(-K_{on1'} \times t)) + R_{max2} \times (1 - \exp(-K_{on2'} \times t)) \qquad \text{(eq. 2)}$$

The ferric pirin-induced p65 binding to the immobilized DNA is tight, so much so that virtually no significant dissociation was observed up to 72 h of continuous buffer injection and rinsing.

Quartz crystal microbalance-dissipation (QCM-D) analyses: Biotin-functionalized sensors were purchased from Q-Sense (Sweden). Streptavidin was flowed over the biotinylated surface, followed by biotin-labeled IgκB-site DNA for immobilization. The equilibrium buffer was 20 mM Tris-HCl (pH 7.4) containing 50 mM NaCl. The QCM-D experiments were carried out with freshly prepared proteins after both frequency and dissipation baselines were stabilized. Simultaneous measurement at multiple frequency overtones of the quartz crystal was conducted but only the data obtained with overtone $n = 5$ were taken for representation. For each measurement, a total volume of 500 µl was continuously injected at a flow rate of 150 µl/min followed by buffer injection for an additional 300 seconds. The net change in frequency and dissipation was calculated by subtracting the values recorded at the sample injection time from those recorded at the end of each rinsing step. This eliminated the influence of nonspecific, loosely bound proteins on the DNA-immobilized surface. The surface was regenerated between each sample injections by flowing through 0.05% SDS, followed by the equilibrium buffer until the baseline was restored. The concentration of p65 was maintained at 0.5 µM, while pirin's concentration varied from 0, 0.5, 1.5, 2.5 and 5 µM for each run of the sample application.

Fluorescence spectroscopy: The FAM-labeled double stranded DNA containing the IgκB sequence (see DNA preparation: section) was added at a final concentration of 20 nM to a

fluorescence cuvette with 0.5 ml binding buffer of 20 mM Tris-HCl (pH 7.4) and 50 mM NaCl. Purified p65 was then titrated into the fluorescence cuvette in the presence or absence of Fe(III)-pirin, or pirin reconstituted with other metal ions. Each measurement was performed after 10 min of incubation to allow for complete protein-protein and protein-DNA interactions. The fluorescence measurements were performed on a Cary Eclipse fluorescence spectrophotometer (Varian, part of Agilent technologies Inc, CA) with an excitation wavelength of 490 nm, an emission wavelength of 520 nm, and a slit width of 10 nm.

Electrochemical study of Pirin by cyclic voltammetry: The midpoint redox potential of pirin was determined by using a single-wall carbon nanotube-modified electrode in a spectroelectrochemical cell hosted in a N_2-filled, O_2-free plastic bag. Pirin (500 µM) in 50 mM Tris-HCl (pH 7.4) was used in this study. The formal potential was obtained from the recorded cyclic voltammetry curves and reported in millivolts versus Ag/AgCl reference.

Electronic paramagnetic resonance (EPR) spectroscopy: X-band EPR spectra were obtained in perpendicular mode on a Bruker (Billerica, MA) EMX or E200 spectrometer at 100-kHz modulation frequency using a high sensitivity resonator ER4119HS. Low temperature (10 K) was maintained with an ITC503S temperature controller, an ESR910 liquid helium cryostat, and LLT650/13 liquid helium transfer tube (Oxford Instruments, Concord, MA). Measurements were conducted by maintaining the frequency of the electromagnetic radiation constant while the magnetic field was swept. Pirin (160 µL/sample, 200 – 450 µM) was prepared in quartz EPR tube with 20 mM Tris-HCl buffer (pH 7.4) containing 50 mM NaCl.

Inductively coupled plasma optical emission spectrometry (ICP-OES): Metal contents of each pirin sample were determined by using a Spectro Genesis spectrometer (Spectro Analytical Instruments GmbH & Co. KG, Germany). Calibration curves were obtained by measuring the standards at the concentrations of each element at 0, 0.1, 0.3, 0.5, 1.0 and 10 ppm (mg/L).

Crystallizations and X-ray structure determinations: Pirin was crystallized through optimization of the conditions previously established (*12*) by hanging drop vapor diffusion in VDX plates (Hampton Research). Single crystals suitable for X-ray data collection were obtained from drops assembled with 1 µL protein solution layered with 1 µL reservoir solution containing 0.1 M MOPS pH 6.5, 15% PEG 20000. Crystal growth took place in a vibration-free crystal growth refrigerator from Molecular Dimensions at 16 °C. The crystals were mounted in small loops of fine rayon fiber and flash-cooled directly in liquid nitrogen after being dipped into the cryoprotectant solution that contained 0.1 M MOPS pH 6.5, 17% PEG 20000 and 30% ethylene glycol. Initial screening was carried out using a Rigaku MicroMax 007 HF Cu-rotating anode X-ray generator, operated at 40 V and 30 mA, and utilizing a Saturn 944 CCD area detector. X-ray diffraction data were collected by either the Rigaku X-ray facility at Emory University or at the SER-CAT beamline 22-ID of the Advanced Photon Source (APS), Argonne National Laboratory, Argonne, IL. All data collection was performed at 100 K. The diffraction data were indexed, integrated and scaled with HKL2000 (*37*). The structures were solved by molecular replacement using MOLREP program (*56*) of the CCP4 suite (*39*) with Fe(II)-pirin structure (PDB accession number 1J1L) (*12*) as search model. Electron density was fit and refined using Coot (*40*), REFMAC (*42*) and PHASER (*97*). Figures showing crystal structures were drawn with PyMOL (http://ww.pymol.org).

In Silico modeling of the supercomplex: Rigid docking of pirin with p65 was conducted using the ZDOCK utility and server (http://zdock.umassmed.edu) (*98*). The PDB files of ferric pirin (PDB accession number 4EWA) and p65 (1RAM) (*99*) were used in model building. The following assumption was applied to the *in silico* model search: the interacting region is located on the C-terminal domain of the RHD of p65. This was based on the experimental observations that pirin facilitates both p50's and p65's DNA binding ability to a target gene. It is known that Bcl-3 interacts with the C-terminal domain of p50, near the dimerization interface (*119*). Pirin is not big enough to be able to interact with both the N-terminal domain and Bcl-3 at the same time. Therefore, pirin can only be located at the C-terminal domain in

close contact with Bcl-3. Especially since it has been shown that all seven ankyrin repeats of Bcl-3 are needed for the interaction between pirin and Bcl-3 (*87*), the C-terminal domain is the most likely region for pirin to bind. Since a similar DNA binding enhancement effect is seen with p65, it is reasonable to assume that the C-terminal domain is being acted upon. Out of the models generated by ZDOCK with the constraint that pirin must interact with the C-terminal domain of the RHD of p65, the top-ranked result shown in Figure 6 involves the *R*-shaped area of pirin, which has been shown in the structural study to differ in conformation when the metal oxidation state changes or metal substitution occurs. The trend of the conformation changes are all the same, *i.e.*, loops moving to one position over the other, when pirin becomes inactivated. Finally, the modeling results were further tested by site-directed mutagenesis experiments.

Table 2. X-ray crystallography data collection and refinement statistics of ligand-free, ligand bound-and Fe-bound intermediates of HAO.

Data collection	**wild-type**	**3-HAA monodentate bound**	**3-HAA bidentate bound**	**Superoxo-bound**	**Alkylperoxo-bound**	**epoxide-bound**	**all-*trans* ACMS-bound**	**2,3-*cis*-4,5-*trans* ACMS-bound**
Detector type	MAR 300 CCD	MAR 325 CCD	MAR 300 CCD	MAR300 CCD	MAR325 CCD	MAR 325 CCD	MAR325 CCD	MAR325 CCD
Source	APS, Sector 22-ID	APS, Sector 22-BM	APS, Sector 22-ID	APS, Sector 22-ID	APS, Sector 22-BM	APS, Sector 22-BM	APS, Sector 22-BM	APS, Sector 22-BM
Space group	$P6_522$	$P6_522$	$P6_522$	$P6_522$	$P6_522$	$P6_522$	$P6_522$	$P6_522$
Unit cell lengths (Å)	*a* = *b* = 58.340, *c* = 231.426	*a* = *b* = 57.961, *c* = 232.079	*a* = *b* = 58.235, *c* = 230.843	*a* = *b* = 58.567, *c* = 232.518	*a* = *b* = 58.153, *c* = 232.656	*a* = *b* = 58.279, *c* = 231.647	*a* = *b* = 58.708, *c* = 232.045	*a* = *b* = 58.299, *c* = 231.116
Unit cell angles (˚)	α = β = 90 º, γ = 120º	α = β = 90 º, γ = 120º	α = β = 90 º, γ = 120º	α = β = 90 º, γ = 120º	α = β = 90 º, γ = 120º	α = β = 90 º, γ = 120º	α = β = 90 º, γ = 120º	α = β = 90 º, γ = 120º
Wavelength (Å)	1.00	1.00	1.00	1.00	1.00	1.00	1.00	1.00
Temperature (K)	100	100	100	100	100	100	100	100
Resolution (Å)[a]	50.00 – 1.75 (1.78 – 1.75)	45.00 – 2.40 (2.44 – 2.40)	45.00 – 2.70 (2.75 – 2.70)	50.00 – 2.01 (2.04 – 2.01)	35.00 – 2.50 (2.54 – 2.50)	35.00 – 2.40 (2.44 – 2.40)	50.00 – 2.06 (2.10 – 2.06)	35.00 – 2.30 (2.34 – 2.30)
Completeness (%)[a]	96.9 (76.8)	82.2 (40.5)	81.6 (32.5)	99.2 (88.9)	77.1 (40.1)	89.3 (45.1)	97.3 (75.0)	89.0 (47.5)
R_{merge} (%)[a, b]	8.7 (47.4)	12.1 (37.4)	13.8 (61.5)	11.5 (39.6)	10.7 (44.1)	11.3 (44.7)	10.5 (35.5)	17.7 (93.3)
$I/\sigma I$[a]	67.2 (3.0)	28.1 (4.1)	25.4 (1.9)	57.7 (3.0)	15.6 (1.8)	31.2 (2.6)	31.7 (1.9)	15.4 (0.8)
Redundancy[a]	23.0 (10.0)	27.2 (12.8)	13.0 (4.7)	21.7 (8.8)	3.9 (3.4)	20.8 (9.2)	26.9 (12.7)	12.7 (2.5)

Refinement	**wild-type**	**3-HAA monodentate bound**	**3-HAA bidentate bound**	**Superoxo-bound**	**Alkylperoxo-bound**	**epoxide-bound**	**all-*trans* ACMS-bound**	**2,3-*cis*-4,5-*trans* ACMS-bound**
Resolution (Å)	1.74	2.40	2.71	2.01	2.50	2.40	2.06	2.30
No. reflections; working/test	24184 / 1239	7879 / 379	5388 / 257	15595 / 829	7522 / 356	8790 / 433	15069 / 755	9426 / 476
R_{work} (%)[c]	0.21	0.24	0.24	0.20	0.24	0.23	0.24	0.25
R_{free} (%)[d]	0.25	0.31	0.35	0.26	0.30	0.31	0.30	0.30
Ramachandran statistics[e]								
Preferred (%)	97.67	97.09	88.82	95.93	90.12	93.02	95.93	94.19
Allowed (%)	2.33	2.33	7.06	4.07	9.30	4.65	4.07	4.07
Root mean square deviation								
Bond lengths (Å)	0.007	0.02	0.11	0.007	0.04	0.009	0.008	0.01
Bond angles (°)	1.17	1.17	1.58	1.17	1.29	1.27	1.20	1.32
PDB access code	4L2N	4L2P	4L2VP	4L2Q	4L2R	4L2S	4L2T	4L2U

Table 3. X-ray crystallography data collection and refinement statistics of HAD bound with different with different small compounds.

Data collection	FeCu-HAO	CuFe-HAO
Detector type	MAR225 CCD	MAR300 CCD
Source	APS, Sector 22-BM	APS, Sector 22-ID
Space group	$P6_522$	$P6_522$
Unit cell lengths (Å)	a = b = 57.70, c = 232.01	a = b = 58.52, c = 230.25
Unit cell angles (˚)	α = β = 90 º, γ = 120º	α = β = 90 º, γ = 120º
Wavelength (Å)	1.00	1.0
Temperature (K)	100	100
Resolution (Å)[a]	45.00 – 2.80 (2.85 – 2.80)	45.00 – 1.75 (1.78 – 1.75)
Completeness (%)[a]	82.9 (22.7)	98.2 (84.3)
R_{merge} (%)[a, b]	8.8 (35.4)	11.2 (60.6)
$I/\sigma I$ [a]	30.6 (3.1)	51.6 (2.5)
Redundancy[a]	16.1 (10.5)	25.3 (13.7)
Refinement		
Resolution (Å)	2.81	1.75
No. reflections; working/test	4970/224	23111/1242
R_{work} (%)[c]	22.1	21.4
R_{free} (%)[d]	32.6	24.2
Ramachandran statistics[e]		
Preferred (%)	86.2	97.7
Allowed (%)	10.5	2.3
Root mean square deviation		
Bond lengths (Å)	0.008	0.027
Bond angles (˚)	1.170	2.274
PDB access code	4HVQ	4HVO
Estimated overall coordinate error		
Esu based on R value	0.51	0.113
Esu based on free R value	0.30	0.110

[a] Values in parentheses are for the highest resolution shell.

[b] $R_{merge} = \Sigma_i |I_{hkl,i} - \langle I_{hkl} \rangle| / \Sigma_{hkl} \Sigma_i I_{hkl,i}$, where $I_{hkl,i}$ is the observed intensity and $\langle I_{hkl} \rangle$ is the average intensity of multiple measurements.

[c] $R_{work} = \Sigma ||F_o| - |F_c|| / \Sigma |F_o|$, where $|F_o|$ is the observed structure factor amplitude, and $|F_c|$ is the calculated structure factor amplitude.

[d] R_{free} is the R factor based on 5% of the data excluded from refinement.

[e] Based on values attained from refinement validation options in COOT.

Table 4. X-ray crystallographic data collection and refinement statistics of human pirin at the active ferric oxidation state

Data Collection	Ferric Pirin (Synchron)	Ferric Pirin (in-house facility)
Detector type	MAR300 CCD	Saturn 944 CCD
Source	APS, Sector 22-ID	Cu Rotating Anode
Space group	$P2_12_12_1$	$P2_12_12_1$
Unit cell lengths (Å)	a = 42.30, b = 67.03, c = 107.06	a = 42.17, b = 66.70, c = 106.21
Unit cell angles (˚)	α = β = γ = 90º	α = β = γ = 90º
Wavelength (Å)	0.80	1.54
Temperature (K)	100	100
Resolution (Å)[a]	21.88 – 1.80 (1.85 – 1.80)	50.00 – 2.48 (2.52 – 2.48)
Completeness (%)[a]	99.5 (94.3)	89.5 (75.0)
R_{merge} (%)[a, b]	14.9 (47.5)	13.1 (52.4)
$I/\sigma I$ [a]	32.9 (3.6)	21.4 (3.8)
Redundancy[a]	9.6(3.8)	5.5 (4.7)
Resolution (Å)	1.80	2.47
No. reflections; working/test	25931/1397	9419/480
R_{work} (%)[c]	18.7	24.0
R_{free} (%)[d]	23.4	29.6
Preferred (%)	96.15	92.66
Allowed (%)	2.80	5.94
Bond lengths (Å)	0.022	0.006
Bond angles (˚)	2.258	1.091
PDB access code	4GUL	4EWA
Esu based on R value	0.029	1.752
Esu based on free R value	0.028	0.382

[a] Values in parentheses are for the highest resolution shell.

[b] $R_{merge} = \Sigma_i |I_{hkl,i} - \langle I_{hkl} \rangle| / \Sigma_{hkl} \Sigma_i I_{hkl,i}$, where $I_{hkl,i}$ is the observed intensity and $\langle I_{hkl} \rangle$ is the average intensity of multiple measurements.

[c] $R_{work} = \Sigma||F_o|-|F_c||/\Sigma|F_o|$, where $|F_o|$ is the observed structure factor amplitude, and $|F_c|$ is the calculated structure factor amplitude.

[d] R_{free} is the R factor based on 5% of the data excluded from refinement.

[e] Based on values attained from refinement validation options in COOT.

Table 5. X-ray crystallographic data collection and refinement statistics of metal-substituted pirin variants

Data Collection	Co(II)-Pirin	Mn(II)-Pirin	Mn(III)-Pirin
Detector type	Saturn 944	MAR300 CCD	Saturn 944
Source	Emory, Cu Rotating Anode	APS, Sector 22-ID	Emory, Cu Rotating Anode
Space group	$P2_12_12_1$	$P2_12_12_1$	$P2_12_12_1$
Unit cell lengths (Å)	a = 42.13, b = 66.25, c = 106.13	a = 42.16, b = 67.03, c = 107.16	a = 42.33, b = 67.07, c = 107.75
Unit cell angles (˚)	α = β = γ = 90º	α = β = γ = 90º	α = β = γ = 90º
Wavelength (Å)	1.54	0.80	1.54
Temperature (K)	100	100	100
Resolution (Å)[a]	35.00 - 2.50 (2.54 - 2.50)	50.00 - 1.56 (1.59 - 1.56)	50 - 2.07 (2.11 – 2.07)
Completeness (%)[a]	84.1 (75.0)	98.2 (97.5)	88.1 (71.2)
R_{merge} (%)[a, b]	11.6 (54.6)	7.7 (59.3)	19.3 (80.8)
$I/\sigma I$[a]	9.4 (1.6)	25.3 (2.5)	10.4 (1.9)
Redundancy[a]	3.7 (3.5)	6.9 (6.4)	9.7 (7.7)
Refinement			
Resolution (Å)	2.65	1.56	2.15
No. reflections; working/test	7038/363	41074/2179	14201/716
R_{work} (%)[c]	19.2	13.5	20.4
R_{free} (%)[d]	23.5	16.7	23.4
Ramachandran statistics[e]			
Preferred (%)	91.36	96.45	95.10
Allowed (%)	5.94	2.96	3.85
Root mean square deviation			
Bond lengths (Å)	0.014	0.026	0.019
Bond angles (˚)	0.927	2.289	1.692
PDB access code	4ERO	4EWE	4EWD
Estimated overall coordinate error			
Esu based on R value	0.082	0.017	0.079
Esu[f] based on free R value	0.176	0.014	0.049

[a] Values in parentheses are for the highest resolution shell.

[b] $R_{merge} = \Sigma_i |I_{hkl,i} - \langle I_{hkl} \rangle| / \Sigma_{hkl} \Sigma_i I_{hkl,i}$, where $I_{hkl,i}$ is the observed intensity and $\langle I_{hkl} \rangle$ is the average intensity of multiple measurements.

[c] $R_{work} = \Sigma ||F_o| - |F_c|| / \Sigma |F_o|$, where $|F_o|$ is the observed structure factor amplitude, and $|F_c|$ is the calculated structure factor amplitude.

[d] R_{free} is the R factor based on 5% of the data excluded from refinement.

[e] Based on values attained from refinement validation options in COOT.

Table 6. X-ray crystallographic data collection and refinement statistics of ferric E32V pirin variant

Data Collection	E32V-Pirin
Detector type	MAR300 CCD
Source	APS, Sector 22-ID
Space group	$P2_12_12_1$
Unit cell lengths (Å)	a = 42.41, b = 66.64, c = 107.33
Unit cell angles (˚)	α = β = γ = 90º
Wavelength (Å)	1.0
Temperature (K)	100
Resolution (Å)[a]	31.84 – 1.70 (1.73 – 1.70)
Completeness (%)[a]	97.1 (79.8)
R_{merge} (%)[a, b]	7.4 (38.4)
$I/\sigma I$ [a]	55.3 (4.0)
Redundancy[a]	12.2 (6.0)
Refinement	
Resolution (Å)	1.70
No. reflections; working/test	31298/1677
R_{work} (%)[c]	18.4
R_{free} (%)[d]	23.4
Ramachandran statistics[e]	
Preferred (%)	96.50
Allowed (%)	1.75
Root mean square deviation	
Bond lengths (Å)	0.023
Bond angles (˚)	2.353
PDB access code	4HLT
Estimated overall coordinate error	
Esu based on R value	0.110
Esu[f] based on free R value	0.116

[a] Values in parentheses are for the highest resolution shell.

[b] $R_{merge} = \Sigma_i |I_{hkl,i} - \langle I_{hkl} \rangle| / \Sigma_{hkl} \Sigma_i I_{hkl,i}$, where $I_{hkl,i}$ is the observed intensity and $\langle I_{hkl} \rangle$ is the average intensity of multiple measurements.

[c] $R_{work} = \Sigma||F_o|-|F_c|| / \Sigma|F_o|$, where $|F_o|$ is the observed structure factor amplitude, and $|F_c|$ is the calculated structure factor amplitude.

[d] R_{free} is the R factor based on 5% of the data excluded from refinement.

[e] Based on values attained from refinement validation options in COOT.

REFERENCES

1. J. M. Dunwell, Cupins: a new superfamily of functionally diverse proteins that include germins and plant storage proteins. *Biotechnol. Genet. Eng. Rev.* **15**, 1 (1998).
2. J. M. Dunwell, A. Purvis, S. Khuri, Cupins: the most functionally diverse protein superfamily? *Phytochemistry* **65**, 7 (2004).
3. S. Khuri, F. T. Bakker, J. M. Dunwell, Phylogeny, function, and evolution of the cupins, a structurally conserved, functionally diverse superfamily of proteins. *Mol. Biol. Evol.* **18**, 593 (April 1, 2001, 2001).
4. J. M. Dunwell, A. Culham, C. E. Carter, C. R. Sosa-Aguirre, P. W. Goodenough, Evolution of functional diversity in the cupin superfamily. *Trends Biochem Sci* **26**, 740 (Dec, 2001).
5. P. L. Roach, I. J. Clifton, V. Fulop, K. Harlos, G. J. Barton, J. Hajdu, I. Andersson, C. J. Schofield, J. E. Baldwin, Crystal structure of isopenicillin *N* synthase is the first from a new structural family of enzymes. *Nature* **375**, 700 (Jun 22, 1995).
6. E. J. Woo, J. M. Dunwell, P. W. Goodenough, A. C. Marvier, R. W. Pickersgill, Germin is a manganese containing homohexamer with oxalate oxidase and superoxide dismutase activities. *Nat. Struct. Biol.* **7**, 1036 (Nov, 2000).
7. B. Gopal, L. L. Madan, S. F. Betz, A. A. Kossiakoff, The crystal structure of a quercetin 2,3-dioxygenase from Bacillus subtilis suggests modulation of enzyme activity by a change in the metal ion at the active site(s). *Biochemistry* **44**, 193 (Jan 11, 2005).
8. R. A. Steiner, K. H. Kalk, B. W. Dijkstra, Anaerobic enzyme-substrate structures provide insight into the reaction mechanism of the copper-dependent quercetin 2,3-dioxygenase. *Proc. Natl. Acad. Sci. U.S.A.* **99**, 16625 (Dec 24, 2002).

9. B. M. Barney, M. R. Schaab, R. LoBrutto, W. A. Francisco, Evidence for a new metal in a known active site: purification and characterization of an iron-containing quercetin 2,3-dioxygenase from Bacillus subtilis. *Protein Expr. Purif.* **35**, 131 (May, 2004).

10. M. S. Lah, M. M. Dixon, K. A. Pattridge, W. C. Stallings, J. A. Fee, M. L. Ludwig, Structure-function in Escherichia coli iron superoxide dismutase: comparisons with the manganese enzyme from Thermus thermophilus. *Biochemistry* **34**, 1646 (Feb 7, 1995).

11. Y. Zhang, K. L. Colabroy, T. P. Begley, S. E. Ealick, Structural studies on 3-hydroxyanthranilate-3,4-dioxygenase: The catalytic mechanism of a complex oxidation involved in NAD biosynthesis. *Biochemistry* **44**, 7632 (2005).

12. H. Pang, M. Bartlam, Q. Zeng, H. Miyatake, T. Hisano, K. Miki, L.-L. Wong, G. F. Gao, Z. Rao, Crystal structure of human Pirin. *J. Biol. Chem.* **279**, 1491 (January 9, 2004).

13. E. L. Hegg, L. Que, Jr., The 2-His-1-carboxylate facial triad--an emerging structural motif in mononuclear non-heme iron(II) enzymes. *Eur. J. Biochem.* **250**, 625 (Dec 15, 1997).

14. O. Kurnasov, V. Goral, K. L. Colabroy, S. Gerdes, A. S, A. Osterman, T. Begley, NAD biosynthesis: identification of the tryptophan to quinolinate pathway in bacteria. *Chem. Biol.* **10**, 1195 (Dec., 2003).

15. K. L. Colabroy, T. P. Begley, The pyridine ring of NAD is formed by a nonenzymatic pericyclic reaction. *J . Am. Chem. Soc.* **127**, 840 (2005).

16. X. Li, M. Guo, J. Fan, W. Tang, D. Wang, H. Ge, H. Rong, M. Teng, L. Niu, Q. Liu, Q. Hao, Crystal structure of 3-hydroxyanthranilic acid 3,4-dioxygenase from Saccharomyces cerevisiae: A special subgroup of the type III extradiol dioxygenases. *Protein Science* **15**, 761 (2006).

17. I. Dilovic, F. Gliubich, G. Malpeli, G. Zanotti, D. Matkovic-Calogovic, Crystal structure of bovine 3-hydroxyanthranilate 3,4-dioxygenase. *Biopolymers* **91**, 1189 (2009).

18. E. Bitto, C. A. Bingman, G. E. Wesenberg, G. N. Phillips Jr., Crystal structure of human 3-hydroxyanthranilic acid 3,4-dioxygenase from Saccharomyces cerevisiae: A special subgroup of the type III extradiol dioxygenases. *RCSB PDB entry: 2QNK*, (2011).

19. L. D. Eltis, J. T. Bolin, Evolutionary relationships among extradiol dioxygenases. *Journal of Bacteriology* **178**, 5930 (1996).

20. E. G. Kovaleva, J. D. Lipscomb, Crystal structures of Fe^{2+} dioxygenase superoxo, alkylperoxo, and bound product intermediates. *Science* **316**, 453 (2007).

21. R. J. Deeth, T. D. H. Bugg, A density functional investigation of the extradiol cleavage mechanism in non-heme iron catechol dioxygenases. *J. Biol. Inorg. Chem.* **8**, 409 (2003/04/01, 2003).

22. P. E. M. Siegbahn, F. Haeffner, Mechanism for Catechol Ring-Cleavage by Non-Heme Iron Extradiol Dioxygenases. *J. Am. Chem. Soc.* **126**, 8919 (2004).

23. T. Borowski, V. Georgiev, P. E. M. Siegbahn, On the observation of a gem diol intermediate after O-O bond cleavage by extradiol dioxygenases. a hybrid DFT study. *J. Mol. Model.* **16**, 1673 (2010).

24. G. J. Christian, S. Ye, F. Neese, Oxygen activation in extradiol catecholate dioxygenases - a density functional study. *Chem. Sci.* **3**, 1600 (2012).

25. M. M. Mbughuni, M. Chakrabarti, J. A. Hayden, E. L. Bominaar, M. P. Hendrich, E. Munck, J. D. Lipscomb, Trapping and spectroscopic characterization of an Fe(III)-superoxo intermediate from a nonheme mononuclear iron-containing enzyme. *Proc. Natl. Acad. Sci. U.S.A.* **107**, 16788 (Sep 28, 2010).

26. E. G. Kovaleva, J. D. Lipscomb, Intermediate in the O-O bond cleavage reaction of an extradiol dioxygenase. *Biochemistry* **47**, 11168 (2008).

27. K. L. Colabroy, H. Zhai, T. Li, Y. Ge, Y. Zhang, A. Liu, S. E. Ealick, F. W. McLafferty, T. P. Begley, The mechanism of inactivation of 3-hydroxyanthranilate-3,4-dioxygenase by 4-chloro-3-hydroxyanthranilate. *Biochemistry* **44**, 7623 (2005).

28. D. T. Sawyer, R. J. P. Williams, *Oxygen Chemistry*. (Oxford University Press, 1991).

29. R. Schwarcz, W. O. Whetsell, Jr., R. M. Mangano, Quinolinic acid: an endogenous metabolite that produces axon-sparing lesions in rat brain. *Science* **219**, 316 (Jan 21, 1983).

30. M. F. Beal, N. W. Kowall, D. W. Ellison, M. F. Mazurek, K. J. Swartz, J. B. Martin, Replication of the neurochemical characteristics of Huntington's disease by quinolinic acid. *Nature* **321**, 168 (1986).

31. T. Muraki, M. Taki, Y. Hasegawa, H. Iwaki, P. C. K. Lau, Prokaryotic homologs of the eukaryotic 3-hydroxyanthranilate 3,4-dioxygenase and 2-amino-3-carboxymuconate-6-semialdehyde decarboxylase in the 2-nitrobenzoate degradation pathway of Pseudomonas fluorescens strain KU-7. *App. Environm. Microbiol.* **69**, 1564 (2003).

32. T. Li, A. L. Walker, H. Iwaki, Y. Hasegawa, A. Liu, Kinetic and spectroscopic characterization of ACMSD from *Pseudomonas fluorescens* reveals a pentacoordinate mononuclear metallocofactor. *J. Am. Chem. Soc.* **127**, 12282 (Sep 7, 2005).

33. Y. Nishizuka, A. Ichiyama, R. K. Gholson, O. Hayaishi, Studies on the metabolism of the benzene ring of tryptophan in mammalian tissues. I. Enzymatic formation of glutaric acid from 3-hydroxyanthranilic acid. *J. Biol. Chem.* **240**, 733 (Feb, 1965).

34. L. W. Chung, X. Li, H. Sugimoto, Y. Shiro, K. Morokuma, ONIOM study on a missing piece in our understanding of heme chemistry: bacterial tryptophan 2,3-dioxygenase with dual oxidants. *J. Am. Chem. Soc.* **132**, 11993 (Sep 1, 2010).

35. J. Basran, I. Efimov, N. Chauhan, S. J. Thackray, J. L. Krupa, G. Eaton, G. A. Griffith, C. G. Mowat, S. Handa, E. L. Raven, The mechanism of formation of N-formylkynurenine by heme dioxygenases. *J. Am. Chem. Soc.* **133**, 16251 (Oct 12, 2011).

36. A. Lewis-Ballester, D. Batabyal, T. Egawa, C. Lu, Y. Lin, M. A. Marti, L. Capece, D. A. Estrin, S.-R. Yeh, Evidence for a ferryl intermediate in a heme-based dioxygenase. *Proc. Natl. Acad. Sci. U.S.A.* **106**, 17371 (October 13, 2009, 2009).

37. Z. Otwinowski, W. Minor, Processing of X-ray diffraction data collected in oscillation mode. *Method Enzymol.* **276**, 307 (1997).

38. A. Vagin, A. Teplyakov, Molecular replacement with MOLREP. *Acta crystallographica. Section D, Biological crystallography* **66**, 22 (Jan, 2010).

39. S. Bailey, The Ccp4 Suite - Programs for Protein Crystallography. *Acta crystallographica. Section D, Biological crystallography* **50**, 760 (Sep 1, 1994).

40. P. Emsley, K. Cowtan, Coot: model-building tools for molecular graphics. *Acta crystallographica. Section D, Biological crystallography* **60**, 2126 (Dec, 2004).

41. A. J. McCoy, R. W. Grosse-Kunstleve, P. D. Adams, M. D. Winn, L. C. Storoni, R. J. Read, Phaser crystallographic software. *J. Appl. Crystallogr.* **40**, 658 (Aug 1, 2007).

42. G. N. Murshudov, A. A. Vagin, E. J. Dodson, Refinement of macromolecular structures by the maximum-likelihood method. *Acta crystallographica. Section D, Biological crystallography* **53**, 240 (May 1, 1997).

43. P. D. Adams, P. V. Afonine, G. Bunkoczi, V. B. Chen, I. W. Davis, N. Echols, J. J. Headd, L. W. Hung, G. J. Kapral, R. W. Grosse-Kunstleve, A. J. McCoy, N. W. Moriarty, R. Oeffner, R. J. Read, D. C. Richardson, J. S. Richardson, T. C. Terwilliger, P. H. Zwart, PHENIX: a comprehensive Python-based system for macromolecular structure solution. *Acta crystallographica. Section D, Biological crystallography* **66**, 213 (Feb, 2010).

44. E. G. Kovaleva, J. D. Lipscomb, Versatility of biological non-heme Fe(II) centers in oxygen activation reactions. *Nat. Chem. Biol.* **4**, 186 (Mar, 2008).

45. E. G. Kovaleva, M. B. Neibergall, S. Chakrabarty, J. D. Lipscomb, Finding intermediates in the O_2 activation pathways of non-heme iron oxygenases. *Acc. Chem Res.* **40**, 475 (2007).

46. J. C. Spain, Biodegradation of nitroaromatic compounds. *Annual review of microbiology* **49**, 523 (1995).

47. A. Esteve-Núñez, A. Caballero, J. L. Ramos, Biological Degradation of 2,4,6-Trinitrotoluene. *Microbiology and Molecular Biology Reviews* **65**, 335 (September 1, 2001, 2001).

48. T. Grummt, H. G. Wunderlich, A. Chakraborty, M. Kundi, B. Majer, F. Ferk, A. K. Nersesyan, W. Parzefall, S. Knasmuller, Genotoxicity of nitrosulfonic acids, nitrobenzoic acids, and nitrobenzylalcohols, pollutants commonly found in ground water near ammunition facilities. *Environmental and molecular mutagenesis* **47**, 95 (Mar, 2006).

49. Y. Hasegawa, T. Muraki, T. Tokuyama, H. Iwaki, M. Tatsuno, P. C. Lau, A novel degradative pathway of 2-nitrobenzoate via 3-hydroxyanthranilate in Pseudomonas fluorescens strain KU-7. *FEMS. Microbiol. Lett.* **190**, 185 (Sep 15, 2000).

50. Y. Hasegawa, T. Muraki, T. Tokuyama, H. Iwaki, M. Tatsuno, P. C. Lau, A novel degradative pathway of 2-nitrobenzoate via 3-hydroxyanthranilate in Pseudomonas fluorescens strain KU-7. *FEMS microbiology letters* **190**, 185 (Sep 15, 2000).

51. O. Wiss, The cleavage and oxidation of 3-hydroxyanthranilic acid. *Zeitschrift fuer Naturforschung* **9b**, 740 (1954).

52. T. Li, J. Ma, J. P. Hosler, V. L. Davidson, A. Liu, Detection of transient intermediates in the metal-dependent non-oxidative decarboxylation catalyzed by a-amino-b-carboxymuconate-e-semialdehyde decarboxylase. *J. Am. Chem. Soc.* **129**, 9278 (2007).

53. T. Muraki, M. Taki, Y. Hasegawa, H. Iwaki, P. C. Lau, Prokaryotic homologs of the eukaryotic 3-hydroxyanthranilate 3,4-dioxygenase and 2-amino-3-carboxymuconate-6-semialdehyde decarboxylase in the 2-nitrobenzoate degradation pathway of *Pseudomonas fluorescens* strain KU-7. *Appl. Environ. Microbiol.* **69**, 1564 (Mar, 2003).

54. Y. Zhang, K. L. Colabroy, T. P. Begley, S. E. Ealick, Structural studies on 3-hydroxyanthranilate-3,4-dioxygenase: the catalytic mechanism of a complex oxidation involved in NAD biosynthesis. *Biochemistry* **44**, 7632 (May 31, 2005).

55. E. L. Hegg, L. Que, Jr., The 2-His-1-carboxylate facial triad--an emerging structural motif in mononuclear non-heme iron(II) enzymes. *European journal of biochemistry / FEBS* **250**, 625 (Dec 15, 1997).

56. A. Vagin, A. Teplyakov, Molecular replacement with MOLREP. *Acta Crystallogr D Biol Crystallogr* **66**, 22 (Jan, 2010).

57. P. Emsley, K. Cowtan, Coot: model-building tools for molecular graphics. *Acta crystallographica. Section D, Biological crystallography* **60**, 2126 (Dec, 2004).

58. M. Andrejasic, J. Praaenikar, D. Turk, PURY: a database of geometric restraints of hetero compounds for refinement in complexes with macromolecular structures. *Acta crystallographica. Section D, Biological crystallography* **64**, 1093 (Nov, 2008).

59. D. M. Arciero, J. D. Lipscomb, B. H. Huynh, T. A. Kent, E. Munck, EPR and Mossbauer studies of protocatechuate 4,5-dioxygenase. Characterization of a new Fe2+ environment. *The Journal of biological chemistry* **258**, 14981 (Dec 25, 1983).

60. R. Silaghi-Dumitrescu, E. D. Coulter, A. Das, L. G. Ljungdahl, G. N. Jameson, B. H. Huynh, D. M. Kurtz, Jr., A flavodiiron protein and high molecular weight rubredoxin from Moorella thermoacetica with nitric oxide reductase activity. *Biochemistry* **42**, 2806 (Mar 18, 2003).

61. I. Moura, P. Tavares, J. J. Moura, N. Ravi, B. H. Huynh, M. Y. Liu, J. LeGall, Purification and characterization of desulfoferrodoxin. A novel protein from Desulfovibrio desulfuricans (ATCC 27774) and from Desulfovibrio vulgaris (strain Hildenborough) that contains a distorted rubredoxin center and a mononuclear ferrous center. *The Journal of biological chemistry* **265**, 21596 (Dec 15, 1990).

62. P. A. Lindahl, S. W. Ragsdale, E. Munck, Mossbauer study of CO dehydrogenase from Clostridium thermoaceticum. *The Journal of biological chemistry* **265**, 3880 (Mar 5, 1990).

63. W. H. Orme-Johnson, Iron-sulfur proteins. Structure and function. *Annu. Rev. Biochem.* **42**, 159 (//, 1973).

64. A. J. Thomson, Iron-sulfur proteins. *Top. Mol. Struct. Biol.* **6**, 79 (//, 1985).

65. H. Sticht, The structure of small electron-transfer proteins. *Recent Res. Dev. Biochem.* **1**, 1 (//, 1999).

66. J. Meyer, J.-M. Moulis. (John Wiley & Sons Ltd., 2001), vol. 1, pp. 505-517.

67. S. Kawasaki, M. Ono, Y. Watamura, Y. Sakai, T. Satoh, T. Arai, J. Satoh, Y. Niimura, An O_2-inducible rubrerythrin-like protein, rubperoxin, is functional as a H_2O_2 reductase in an obligatory anaerobe *Clostridium acetobutylicum*. *FEBS Lett* **581**, 2460 (5/29/, 2007).

68. E. D. Coulter, D. M. Kurtz, Jr., A role for rubredoxin in oxidative stress protection in *Desulfovibrio vulgaris*: Catalytic electron transfer to rubrerythrin and two-iron superoxide reductase. *Arch. Biochem. Biophys.* **394**, 76 (//, 2001).

69. X. Li, M. Guo, J. Fan, W. Tang, D. Wang, H. Ge, H. Rong, M. Teng, L. Niu, Q. Liu, Q. Hao, Crystal structure of 3-hydroxyanthranilic acid 3,4-dioxygenase from Saccharomyces cerevisiae: a special subgroup of the type III extradiol dioxygenases. *Protein Sci.* **15**, 761 (Apr, 2006).

70. R. Sen, D. Baltimore, Multiple nuclear factors interact with the immunoglobulin enhancer sequences. *Cell* **46**, 705 (1986).

71. R. Sen, D. Baltimore, Inducibility of k immunoglobulin enhancer-binding protein NF-kB by a posttranslational mechanism. *Cell* **47**, 921 (1986).

72. J. A. Romashkova, S. S. Makarov, NF-kB is a target of AKT in anti-apoptotic PDGF signalling. *Nature* **401**, 86 (Sep 2, 1999).

73. M. Karin, A. Lin, NF-kB at the crossroads of life and death. *Nat. Immunol.* **3**, 221 (Mar, 2002).

74. Q. Li, I. M. Verma, NF-kB regulation in the immune system. *Nat. Rev. Immunol.* **2**, 725 (2002).

75. F. E. Chen, D. B. Huang, Y. Q. Chen, G. Ghosh, Crystal structure of p50/p65 heterodimer of transcription factor NF-kB bound to DNA. *Nature* **391**, 410 (Jan 22, 1998).

76. S. Ghosh, M. J. May, E. B. Kopp, NF-kB and Rel proteins: evolutionarily conserved mediators of immune responses. *Annu. Rev. Immunol.* **16**, 225 (1998).

77. G. Ghosh, G. van Duyne, S. Ghosh, P. B. Sigler, Structure of NF-kB p50 homodimer bound to a kB site. *Nature* **373**, 303 (Jan 26, 1995).

78. H. L. Pahl, Activators and target genes of Rel/NF-kB transcription factors. *Oncogene* **18**, 6853 (Nov 22, 1999).

79. T. D. Gilmore, NF-kB target genes. *http://www.bu.edu/nf-kb/gene-resources/target-genes/*, (2008).

80. K. Gosselin, NF-kB target genes. *http://bioinfo.lifl.fr/NF-KB/*, (2004).

81. K. W. Jeong, K. Kim, A. J. Situ, T. S. Ulmer, W. An, M. R. Stallcup, Recognition of enhancer element–specific histone methylation by TIP60 in transcriptional activation. *Nat. Struct. Mol. Biol.* **18**, 1358 (2011).

82. T. D. Merson, M. P. Dixon, C. Collin, R. L. Rietze, P. F. Bartlett, T. Thomas, A. K. Voss, The transcriptional coactivator Querkopf controls adult neurogenesis. *J. Neurosci.* **26**, 11359 (Nov 1, 2006).

83. A. M. Naar, B. D. Lemon, R. Tjian, Transcriptional coactivator complexes. *Annu. Rev. Biochem.* **70**, 475 (2001).

84. A. Oeckinghaus, M. S. Hayden, S. Ghosh, Crosstalk in NF-kB signaling pathways. *Nat. Immunol.* **12**, 695 (2011).

85. F. E. Chen, G. Ghosh, Regulation of DNA binding by Rel/NF-kB transcription factors: structural views. *Oncogene* **18**, 6845 (Nov 22, 1999).

86. W. M. F. Wendler, E. Kremmer, R. Förster, E.-L. Winnacker, Identification of Pirin, a novel highly conserved nuclear protein. *J. Biol. Chem.* **272**, 8482 (March 28, 1997, 1997).

87. R. Dechend, F. Hirano, K. Lehmann, V. Heissmeyer, S. Ansieau, F. G. Wulczyn, C. Scheidereit, A. Leutz, The Bcl-3 oncoprotein acts as a bridging factor between NF-kB/Rel and nuclear co-regulators. *Oncogene* **18**, 3316 (Jun 3, 1999).

88. D. Gurmu, J. Lu, K. A. Johnson, P. Nordlund, A. Holmgren, H. Erlandsen, The crystal structure of the protein YhaK from *Escherichia coli* reveals a new subclass of redox sensitive enterobacterial bicupins. *Proteins* **74**, 18 (Jan, 2009).

89. M. Adams, Z. Jia, Structural and biochemical analysis reveal Pirins to possess quercetinase activity. *J. Biol. Chem.* **280**, 28675 (August 5, 2005, 2005).

90. S. Licciulli, C. Luise, G. Scafetta, M. Capra, G. Giardina, P. Nuciforo, S. Bosari, G. Viale, G. Mazzarol, C. Tonelli, L. Lanfrancone, M. Alcalay, Pirin inhibits cellular senescence in melanocytic cells. *Am. J. Pathol.* **178**, 2397 (2011).

91. I. Miyazaki, S. Simizu, H. Okumura, S. Takagi, H. Osada, A small-molecule inhibitor shows that pirin regulates migration of melanoma cells. *Nat. Chem. Biol.* **6**, 667 (2010).

92. K. Brzóska, T. M. Stepkowski, M. Kruszewski, Putative proto-oncogene Pir expression is significantly up-regulated in the spleen and kidney of cytosolic superoxide dismutase-deficient mice. *Redox Rep.* **16**, 129 (2011).

93. B. Gelbman, A. Heguy, T. O'Connor, J. Zabner, R. Crystal, Upregulation of pirin expression by chronic cigarette smoking is associated with bronchial epithelial cell apoptosis. *Respir Res* **8**, 10 (2007).

94. S. E. Wurster, L. J. Maher, 3rd, Selection and characterization of anti-NF-kB p65 RNA aptamers. *RNA* **14**, 1037 (June, 2008).

95. Y. Q. Chen, L. L. Sengchanthalangsy, A. Hackett, G. Ghosh, NF-kB p65 (RelA) homodimer uses distinct mechanisms to recognize DNA targets. *Structure* **8**, 419 (Apr 15, 2000).

96. B. M. Sjöberg, P. Reichard, A. Gräslund, A. Ehrenberg, The tyrosine free radical in ribonucleotide reductase from *Escherichia coli*. *J. Biol.Chem.* **253**, 6863 (October 10, 1978).

97. A. J. McCoy, R. W. Grosse-Kunstleve, P. D. Adams, M. D. Winn, L. C. Storoni, R. J. Read, Phaser crystallographic software. *J Appl Crystallogr* **40**, 658 (Aug 1, 2007).

98. R. Chen, L. Li, Z. Weng, ZDOCK: an initial-stage protein-docking algorithm. *Proteins* **52**, 80 (Jul 1, 2003).

99. Y. Q. Chen, S. Ghosh, G. Ghosh, A novel DNA recognition mode by the NF-kB p65 homodimer. *Nat. Struct. Biol.* **5**, 67 (Jan, 1998).

100. C. B. Phelps, L. L. Sengchanthalangsy, S. Malek, G. Ghosh, Mechanism of κB DNA binding by Rel/NF-κB dimers. *Journal of Biological Chemistry* **275**, 24392 (August 11, 2000, 2000).

101. W. Y. X. Peh, E. Reimhult, H. F. Teh, J. S. Thomsen, X. Su, Understanding ligand binding effects on the conformation of estrogen receptor α-DNA complexes: A combinational quartz crystal microbalance with dissipation and surface plasmon resonance study. *Biophys. J.* **92**, 4415 (June 15, 2007).

102. R. Schreck, H. Zorbas, E.-L. Winnacker, P. A. Baeuerle, The NF-kB transcription factor induces DNA bending which is modulated by its 65-kD subunit. *Nucleic Acids Res.* **18**, 6497 (November 25, 1990, 1990).

103. N. C. Horton, J. J. Perona, Crystallographic snapshots along a protein-induced DNA-bending pathway. *Proc. Natl. Acad. Sci. U. S. A.* **97**, 5729 (May 23, 2000).

104. C. M. Cordas, A. G. Duarte, J. J. Moura, I. Moura, Electrochemical behaviour of bacterial nitric oxide reductase-evidence of low redox potential non-heme Fe_B gives new perspectives on the catalytic mechanism. *Biochim Biophys Acta* **1827**, 233 (Mar, 2013).

105. C. K. Vance, A. F. Miller, a simple proposal that can explain the inactivity of metal-substituted superoxide dismutases. *J Am Chem Soc* **120**, 461 (1998/01/01, 1998).

106. G. D. Fasman, *Physical Chemical Data*. CRC Handbook of Biochemistry and Molecular Biology (CRC Press, Cleveland, Ohio, ed. 3rd ed, 1976), vol. 2.

107. A. Karlsson, J. V. Parales, R. E. Parales, D. T. Gibson, H. Eklund, S. Ramaswamy, Crystal structure of naphthalene dioxygenase: Side-on binding of dioxygen to iron. *Science* **299**, 1039 (February 14, 2003).

108. E. G. Kovaleva, J. D. Lipscomb, Crystal structures of Fe^{2+} dioxygenase superoxo, alkylperoxo, and bound product intermediates. *Science* **316**, 453 (April 20, 2007).

109. F. Liu, I. Rehmani, S. Esaki, R. Fu, L. Chen, V. de Serrano, A. Liu, Pirin is an iron-dependent redox regulator of NF-kB. *Proc. Natl. Acad. Sci. U.S.A.* **110**, 9722 (Jun 11, 2013).

110. R. H. Hubner, J. D. Schwartz, P. De Bishnu, B. Ferris, L. Omberg, J. G. Mezey, N. R. Hackett, R. G. Crystal, Coordinate control of expression of Nrf2-modulated genes in the human small airway epithelium is highly responsive to cigarette smoking. *Molecular medicine (Cambridge, Mass.)* **15**, 203 (Jul-Aug, 2009).

111. B. A. Mercer, V. Lemaitre, C. A. Powell, J. D'Armiento, The epithelial cell in lung health and emphysema pathogenesis. *Curr. Respir. Med. Rev.* **2**, 101 (May, 2006).

112. D. Orzaez, A. J. de Jong, E. J. Woltering, A tomato homologue of the human protein PIRIN is induced during programmed cell death. *Plant Mol. Biol.* **46**, 459 (Jul, 2001).

113. S. Licciulli, V. Cambiaghi, G. Scafetta, A. M. Gruszka, M. Alcalay, Pirin downregulation is a feature of AML and leads to impairment of terminal myeloid differentiation. *Leukemia* **24**, 429 (2009).

114. E. Owusu-Ansah, U. Banerjee, Reactive oxygen species prime *Drosophila* haematopoietic progenitors for differentiation. *Nature* **461**, 537 (Sep 24, 2009).

115. J.-W. Lee, J. D. Helmann, The PerR transcription factor senses H_2O_2 by metal-catalysed histidine oxidation. *Nature* **440**, 363 (2006).

116. D. A. K. Traore, A. E. Ghazouani, L. Jacquamet, F. Borel, J.-L. Ferrer, D. Lascoux, J.-L. Ravanat, M. Jaquinod, G. Blondin, C. Caux-Thang, V. Duarte, J.-M. Latour, Structural and functional characterization of 2-oxo-histidine in oxidized PerR protein. *Nat. Chem. Biol.* **5**, 53 (2009).

117. F. Michel, M. Soler-Lopez, C. Petosa, P. Cramer, U. Siebenlist, C. W. Muller, Crystal structure of the ankyrin repeat domain of Bcl-3: a unique member of the IkB protein family. *EMBO J.* **20**, 6180 (2001).

118. E. Stenberg, B. Persson, H. Roos, C. Urbaniczky, Quantitative determination of surface concentration of protein with surface plasmon resonance using radiolabeled proteins. *J. Colloid Interface Sci.* **143**, 513 (1991).

119. F. G. Wulczyn, M. Naumann, C. Scheidereit, Candidate proto-oncogene bcl-3 encodes a subunit-specific inhibitor of transcription factor NF-kappa B. *Nature* **358**, 597 (Aug 13, 1992).